Spring 2013

Integration of Mars Global Surveyor observations of the MY 25 planet-encircling dust storm on Mars: implications for atmospheric dynamics and modeling

John Noble
San Jose State University

INTEGRATION OF MARS GLOBAL SURVEYOR OBSERVATIONS OF THE MY 25 PLANET-ENCIRCLING DUST STORM ON MARS: IMPLICATIONS FOR ATMOSPHERIC DYNAMICS AND MODELING

A Thesis

Presented to

The Faculty of the Department of Meteorology and Climate Science

San José State University

In Partial Fulfillment

of the Requirements for the Degree

Master of Science

by

John Noble

May 2013

The Designated Thesis Committee Approves the Thesis Titled

INTEGRATION OF MARS GLOBAL SURVEYOR OBSERVATIONS OF THE MY 25 PLANET-ENCIRCLING DUST STORM ON MARS: IMPLICATIONS FOR ATMOSPHERIC DYNAMICS AND MODELING

by

John Noble

APPROVED FOR THE DEPARTMENT OF METEOROLOGY AND

CLIMATE SCIENCE

SAN JOSÉ STATE UNIVERSITY

May 2013

Professor Alison F. C. Bridger	Department of Meteorology and Climate Science
Dr. Robert M. Haberle	NASA Ames Research Center
R. John Wilson	NOAA Geophysical Fluid Dynamics Laboratory
Professor Eugene C. Cordero	Department of Meteorology and Climate Science

ABSTRACT

INTEGRATION OF MARS GLOBAL SURVEYOR OBSERVATIONS OF THE MY 25 PLANET-ENCIRCLING DUST STORM ON MARS: IMPLICATIONS FOR ATMOSPHERIC DYNAMICS AND MODELING

by John Noble

A survey of observations and analyses of the Mars year (MY) 25 planet-encircling dust storm (PDS) on Mars is presented. The environmental causes and dynamical mechanisms responsible for PDS initiation, expansion, decay, and interannual frequency are not fully understood. PDS seasonal occurrence suggests the presence of climatic and environmental components, yet interannual variability suggests that initiation and expansion mechanisms are not solely seasonal in character. The objectives of this research were to better understand the dynamical processes and circulation components responsible for MY 25 PDS initiation and evolution and to analyze why a PDS developed in MY 25 and not in MY 24 or 26.

Negative anomalies in temperature data with ~3-sol periodicity indicate the presence of baroclinic eddies. After comparing these eddies with dust storms observed in satellite imagery, the author hypothesized that six eastward-traveling transient baroclinic eddies triggered the MY 25 precursor storms due to the enhanced dust lifting associated with their low-level wind and stress fields. They were followed by a seventh eddy that contributed to dust storm expansion. All seven eddy cold anomalies were less than –4.5 K. It is possible that the sustained series of high-amplitude eddies in MY 25 were a factor in PDS onset and expansion.

ACKNOWLEDGMENTS

Many individuals have contributed to this thesis. First, thanks are due to those who contributed the data used in this investigation: Mike Smith (TES), Jeffrey Barnes (FFSM), James Murphy and Terry Martin (MHSA), Michael Malin and Bruce Cantor (MOC). Second, thanks are due to the NASA Ames Hyperwall development team, Chris Henze and Tim Sandstrom, for their assistance and expertise. Third, thanks are due to Jeffrey Hollingsworth and Melinda Kahre at NASA Ames for their valuable feedback and comments. Lastly, great appreciation is due to the above thesis committee members.

DEDICATION

This thesis is dedicated to my friends and family, especially Tenzin Choney, whose patience and support helped make it possible.

TABLE OF CONTENTS

LIST OF FIGURES

LIST OF TABLES

1 Introduction

1.1 Overview

Martian mineral aerosols (dust, 1-2 μm radius) have significant effects on weather and climate because they are dynamically, radiatively, and thermally coupled with the atmosphere (Haberle *et al.* 1982; Kahn *et al.* 1992; Strausberg *et al.* 2005). Martian planet-encircling dust storms (PDS) play a significant role in the Martian climate system by affecting atmospheric thermal structure and circulation. They also affect the surface through weathering and by changing thermal inertia and albedo (Martin and Zurek 1993).

The Mars Global Surveyor (MGS) orbiter observed a PDS from June - October 2001, corresponding to Mars year 25 (MY 25), areocentric longitude (L_s) 176.2–263.4°. Areocentric longitude is an angular measure of Mars' orbit relative to the Sun and is used to specify sols (Martian days) and seasons (see section 2.2 for discussion of time). MY 25 PDS was the seasonally earliest, sixth confirmed (Cantor 2007), and most thoroughly recorded PDS to date (Cantor 2007; Smith *et al.* 2002; Strausberg *et al.* 2005). MGS thermal emission spectrometer (TES) observations of temperature and opacity during the MY 25 PDS were described by Smith *et al.* (2002). Strausberg *et al.* (2005) analyzed both TES and Mars Orbiter Camera (MOC) data, along with Mars General Circulation Model (MGCM) output, to characterize storm evolution. Cantor (2007) conducted a comprehensive analysis of the PDS using MOC imagery and visible opacity data and concluded that the MY 25 PDS was initiated by 10 local storms that occurred in seven pulses over a 15-sol period in the Hellas region (Fig. 1) from L_s=176.2–184.6°.

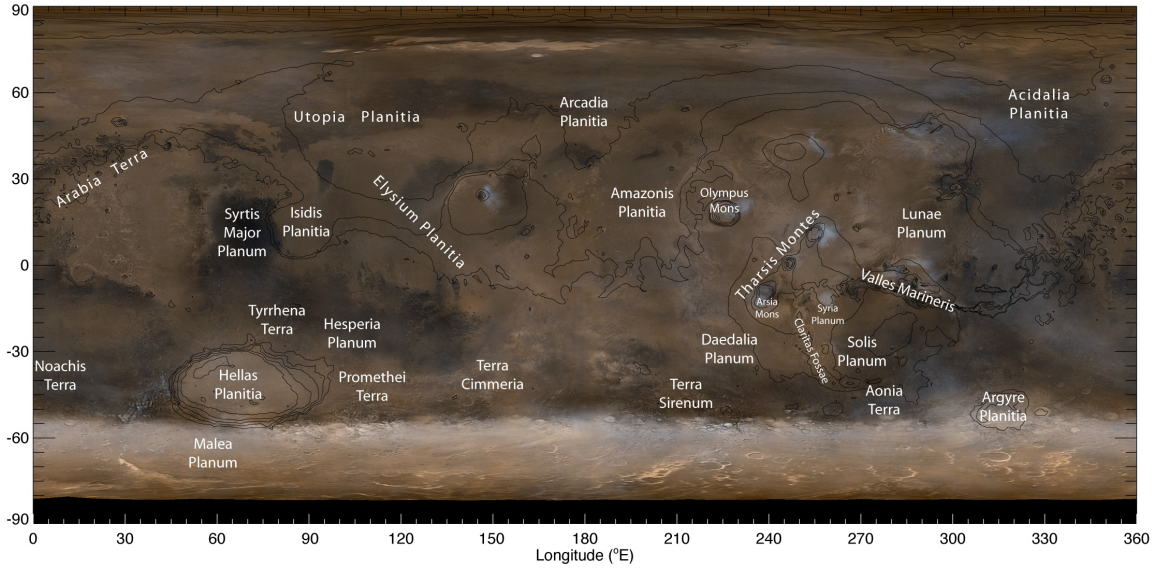

Figure 1. MOC DGM with key place names (MOC maps courtesy of B. Cantor and M. Malin, Malin Space Science Systems)

The majority of storms originated along the south polar seasonal cap edge near Hellas and moved northward and northeastward at 1.5–16.2 m s^{-1}. Derived wind speeds showed strong (~30 m s^{-1}) northward flow along the western edge of Hellas (Cantor 2007).

After L_s=184.7°, storm activity spread equatorward, southward, and eastward, which was the main direction of propagation. At L_s=188.2°, a second major dust lifting center was initiated in Claritas (12.6°S, 249°E). The mechanisms responsible for this initiation are not fully understood. Strausberg *et al.* (2005) hypothesized that lifting was activated by enhanced Hadley circulation associated with increased opacity levels. At L_s=188.8° another lifting center was initiated in Claritas Fossae (12.5° S, 249° E). By L_s=189.6°, these local storms grew to regional scale and encompassed 7.1×10^6 km^2. By L_s=191°, the storm had fully encircled the planet, and active lifting in Hellas appeared to

abate (Cantor 2007; Strausberg *et al.* 2005). Dust lifting in Claritas appears to have terminated between L_s=210–214°, and PDS decay set in. Dust opacity levels returned to typical seasonal levels by L_s=260° (Cantor 2007; Strausberg *et al.* 2005).

Following the storm, both daytime surface and atmospheric temperatures were lower compared to the year before the storm for a period of one Mars year, while nighttime surface and atmospheric temperatures remained almost unchanged (Smith 2004). Smith (2002, 2004) reported a 3 K decrease in globally-averaged surface temperature from the previous Mars year and attributed this to increased albedo from deposition of bright dust on the surface following the PDS. Bright dust increases reflection of solar radiation and decreases absorption at the surface. Cantor (2007) calculated a 3% rise in the average surface albedo following the storm and reported a similar decline in surface temperature measured from MOC sensors.

1.2 Nomenclature

The following nomenclature is used in this work. Standard Martian place names are shown in Fig. 1. The planet can be divided into two longitudinal hemispheres, eastern and western, that are hereafter referred to as the Hellas and Tharsis hemispheres respectively. Four quadrants are designated as Hellas (0–180° E, SH), Utopia (0–180° E, NH), Solis (180–360° E, SH), and Olympus (180–360° E, NH). 'High latitudes' refers to those regions north of 60° N and south of 60° S.

1.3 Problem Statement

The environmental causes and dynamical mechanisms responsible for PDS initiation, expansion, decay, and interannual frequency are not fully understood, posing fundamental unsolved problems in Martian atmospheric science (Haberle 1986; Ingersoll and Lyons 1993; Kahre *et al.* 2006; Smith *et al.* 2002). PDS seasonal occurrence suggests the presence of climatic/environmental precursors and components, yet interannual variability suggests that initiation and expansion mechanisms are not solely seasonal in character (Zurek and Martin 1993).

In recent years, much new data have been amassed. However, there are some problems with these data. For example, significant portions of the TES retrievals are missing or unreliable due to extreme opacity levels and diminished contrast. TES opacity retrieval reliability is partially a function of ground-air temperature contrast, with reliability diminishing as contrast approaches zero. Contrast limits occur at high-latitudes (>55°N, <60°S) and in extremely dusty conditions. These data gaps often occur in important times and places (Hellas and Claritas) during storm initiation and expansion and likely decrease the reliability of MGCM simulations forced with TES dust (Wilson *et al.* 2008).

1.4 Objectives and Methods

The objectives of this work were to better understand and characterize the dynamical processes responsible for PDS initiation and expansion, specifically examining the following questions: 1) Which circulation components were involved in storm onset and evolution? 2) How did the temperature and dust opacity fields evolve together? For

example, what was the relation between eddies seen in the temperature field (discussed below) and storms resolved by MOC? What was the relation between the quasi-stationary wave one structure seen in the temperature field and the dust evolution observed by TES and MOC? What was the relation between the vertical thermal structure of the atmosphere and suspended dust measured by TES? 3) Is there a dynamical connection between dust lifting in Hellas and Claritas? 4) Do MGS data show interannual variability that suggests why a PDS formed in MY 25 and not in MY 24 or 26? Although clues to these questions can be found in MGS data, they cannot be answered conclusively with observations alone; MGCM simulations are required to rigorously address them.

We employed several methods to accomplish these objectives. First, we developed software to integrate all available MGS data. Second, we analyzed MGS data to identify associations and correlations between quantities (Gawrych *et al.* 2004; Haberle *et al.* 2005; Noble *et al.* 2006). Third, we produced synthesized dust opacity maps (SDM) that provide better bases and constraints for modeling (Noble *et al.* 2007; Wilson *et al.* 2008).

MGS observations are the first comprehensive datasets that permit, through their integration, a detailed quantitative analysis of a planetary extreme weather event. The importance of this work is severalfold: 1) fundamental geophysical research is required to better understand the Martian atmosphere (*e.g.*, PDS investigation increases understanding of the radiative influence of dust); 2) global dust can be used as a tracer to reveal underlying dynamical processes and improve our understanding of regional and

global circulation components (since wind is a fundamental quantity in the primitive equations but was not measured by MGS); 3) the Martian atmosphere serves as a planetary laboratory to test and advance our understanding of geophysics and comparative planetary atmospheric science; 4) comprehensive knowledge of the Martian atmosphere is necessary to ensure the safety and success of future robotic and human missions.

1.5 Organization

This work has the following organization. Chapter 2 reviews the history of Mars scientific investigations and results, particularly those related to atmospheric dynamics, aerosols, and dust storms. Chapter 3 discusses MGS datasets and the analysis methods we employed. Data include MOC daily global maps (DGM) (Cantor 2007), TES temperature (Conrath *et al.* 2000), TES dust optical depth retrievals (Smith 2004; Smith *et al.* 2000), and Mars Horizon Sensor Assembly (MHSA) temperature retrievals (Martin 1997; Martin and Murphy 2003). Fast Fourier Synoptic Mapping (FFSM) analysis of TES thermal data (Barnes 2001, 2006) is also examined. We extended previous Fortran and Interactive Data Language (IDL) codes to bin temperature and opacity data (10° longitude × 5° latitude), generate contours, and superimpose on MOC DGMs. In addition, we superimposed the longitudinal extent of MOC visible storms on FFSM longitude-time plots to compare the evolution of storms and transient eddies. The integration of these data affords the opportunity to analyze storm development in conjunction with the evolving temperature and opacity fields.

Chapter 4 presents a sol-by-sol description of storm evolution and results from integrating MGS datasets. We propose the following storm phases: 1) precursor, L_s=176.2–184.7°: storm initiation and early growth around the Hellas region; 2) expansion, L_s=184.7–193°: eastward/northeastward expansion of storm activity from Hellas, development of new lifting centers in Daedalia and Solis Plana, and storm growth to planetary-scale; 3) mature, L_s=193–210°: peak of globally-averaged opacity and temperature (surface and 0.5 hPa); 4) decay, L_s=210–263°: opacity and temperature fields returning to seasonal levels. In this work we examine the first three storm phases.

Chapter 5 presents a comparison of MY 24–26 FFSM data and MY 24 and 25 storms visible to MOC (hereafter MOC-observed storms). Interannual comparison shows that MY 25 eddies during the precursor phase in Hellas are moderately stronger (greater amplitude) than corresponding MY 24 and 26 eddies.

Chapter 6 presents synthesized dust maps. Known limitations of TES observations result in significant spatial gaps in dust opacity data, especially at high latitudes. MGCMs are essential tools for predicting circulation; however, their ability to model the MY 25 PDS is dependent on more accurate representations of dust distribution. We produced synthesized datasets of column dust opacity and dust lifting sources in order to better constrain estimates of dust distribution and forcing. We used these improved opacity estimates as input into the NASA and Geophysical Fluid Dynamics Laboratory (GFDL) MGCMs in order to test current hypotheses concerning storm initiation and evolution. We produced model results that relate the simulated circulation, atmospheric temperature, and aerosol distribution to the available observations in an

effort to better understand the underlying dynamics of the initiation and growth of the MY 25 PDS.

Chapter 7 discusses the results and implications of this investigation. FFSM analysis of TES 3.7 hPa thermal data shows the presence of eastward-traveling waves at 60° S with a period of about three sols. We hypothesized that these waves are baroclinic eddies that contributed to the initiation of precursor storms. An examination of the spatial and temporal relationship of FFSM eddies and MOC storms suggests a strong correlation between eastward eddy propagation and eastward storm evolution.

Superimposed TES 2 pm temperature contours on MOC imagery showed that suspended dust in the Hellas sector led to the amplification of a quasi-stationary wave-one structure in the temperature field. This feature is most evident between the 0.11 and 0.83 hPa levels, with a peak-to-trough amplitude of ~30 K at 0.5 hPa. Initiation of storm activity in Claritas began on L_s=188.1°, one sol after the wave reached maximum amplitude on L_s=187.5°.

Chapter 8 summarizes the results and hypotheses that will be tested in future MGCM simulations.

2 Mars Background

2.1 Observations and Missions

2.1.1 PRE-1960s

Mars, Earth's sister planet, has captured the human imagination for eons. Due to its red color, the planet became a symbol of blood, fire, and war to many ancient cultures, including the Greeks, who named it Ares after their god of war. The root 'ares' is found in such words as areocentric and areography, and Mars' symbol, ♂, represents a shield and sword (Glasstone 1968). Mars has been the focus of ground-based telescopic observations since the 1600s. The earliest drawings of the planet were made by Fontana in 1636 and Huygens in 1659 (Flammarion 1892), the latter reproducing the dark region of Syrtis Major (Glasstone 1968). These observations enabled Huygens to conclude that Mars rotates around a north-south axis and allowed him to estimate a rotational period of ~24 hr (Glasstone 1968).

Cassini (1707) performed detailed observations of Mars and made a number of scientific contributions, including the first drawings of polar caps (Flammarion 1892) and an estimate of Mars' rotational period (~24 hr 40 min) from observations of dark spots (Anonymous 1666), remarkably close to the current value of ~24 hr 37 min. Cassini (1707) also hypothesized from stellar occultation observations that Mars had an 'extensive atmosphere,' a characterization that was debated for over a century (South 1831).

Herschel (1784) made observations that allowed him to estimate Mars' inclination angle at ~30º (*cf.* current value of ~24º), and to thus conclude that Mars has four seasons. He also posited that Mars has a "considerable but moderate atmosphere" (Glasstone 1968). Yellow-colored regions ("yellow clouds") have been observed for ~ two centuries (Gierasch and Goody 1973), first by Flaugergues in the late 1700s and early 1800s (Flammarion 1892; McKim 1996), and later by Schiaparelli (1893b, 1899), Flammarion (1892), and others. Schiaparelli (1893a) produced some of the first global maps of Mars and introduced much of the Latin nomenclature (Fig. 1) that is currently used (Glasstone 1968).

Campbell (1894) hypothesized that Mars' polar caps may consist of CO_2 based on several lines of evidence and reasoning, including observations of the south polar cap almost completely disappearing, coupled with an apparent absence of clouds, and the absence of aqueous vapor in spectroscopic observations. Campbell (1894) further hypothesized that CO_2 may be the principal constituent in the Martian atmosphere, and argued that spectroscopic evidence disproves previous theories claiming that Mars' red color was caused by an extensive atmosphere.

Pickering (1905) observed that Martian clouds are "always of a light yellow color," and reported measured cloud heights of ~15 miles (24 km). Antoniadi made many contributions to Mars planetary science, including first hypothesizing that yellow clouds were dust storms (Antoniadi 1930; James 1985; McKim 1996), noting their common occurrence near perihelion (Martin and Zurek 1993), and correlating melting polar cap data with the sun spot cycle (Antoniadi 1916).

Twentieth century spectroscopic and polarization observations produced measurements of many physical and chemical properties, including albedo, water vapor, CO_2, and atmospheric pressure (Martin and Zurek 1993). Menzel (1926) used estimates of Martian albedo and scattering to calculate an upper limit of surface air pressure of ≤ 5–6 cmHG (~66–79 hPa at 0ºC), values that are ~10 times greater than in situ Viking Lander measurements. Further calculations of surface air pressure were performed by Hess (1948) using Martian cloud height and temperature estimates, and by Dollfus (1948) using the polarization of reflected planetary light to calculate the atmospheric contribution. Both researchers independently arrived at 80 hPa estimates. Hess (1950) later calculated the vertical structure of the Martian atmosphere and produced global temperature and wind maps.

2.1.2 1960s –1990s

The era of spacecraft exploration of Mars began in 1963 when Mars 1 (USSR) flew within 195 000 km of the planet and collected data on the solar wind and magnetic fields. In 1965, Mariner-4 (US) flew by Mars at an altitude of 9850 km and conducted eight experiments including measurement of magnetic fields, radiation belts, and atmospheric pressure (Snyder and Moroz 1992). In 1971, Mariner-9 arrived during the decay phase of a dust storm and recorded thousands of images later used to infer statistical properties of the upper portion of the storm, including its height of ~60 km. The spacecraft was thus unable to obtain clear pictures of the surface for several weeks (Anderson and Leovy 1978). The Viking orbiters, however, observed the initiation, evolution, and decay of two global dust storms in 1977. Quantities derived from Viking

orbiter retrievals include temperature, opacity, and thermal inertia (Briggs *et al.* 1979). Discovery of a persistent background dust opacity was a significant finding of that mission (Kahn *et al.* 1992).

2.1.3 1990s – PRESENT

The MGS orbiter arrived at Mars in 1997 (Conrath *et al.* 2000). MGS completes 12 sun-synchronous orbits per sol, producing ground tracks separated by ~30° of longitude. It carries a number of instruments that monitored the MY 25 PDS, including TES, MOC, and MHSA. Retrievals of atmospheric thermal structure up to 0.01 hPa and aerosol (mineral and water-ice) column abundance have been obtained from the IR spectra (7 -50 μm) returned by TES (Smith 2001). The spatial and temporal resolution and coverage of TES observations greatly exceed those of previous spacecraft, and its datasets are an important advancement in the effort to understand mechanisms behind global dust storms (Smith *et al.* 2001; Smith *et al.* 2002).

Although not used in this study, the Mars Reconnaissance Orbiter (MRO) arrived at Mars in 2006. MROs carries an unprecedented array of instruments designed for obtaining atmospheric data in an ongoing mission. The Mars Color Imager (MARCI) is conducting daily, synoptic imaging used to study the evolution of weather systems, surface – atmosphere interactions, and climate evolution. MARCI also has multi-spectral capabilities to distinguish between aerosol compositions (Clancy *et al.* 2006).

2.2 Physical Characteristics

Mars is the fourth terrestrial planet from the sun and is similar to Earth in many respects, including radiative environment, length of solar day, and axial tilt. Moreover, Earth and Mars have similar geophysical systems, *i.e.,* atmospheres, cryospheres, lithospheres, and possibly hydrospheres (in previous Martian epochs). Outstanding differences include: the Martian atmospheric chemical composition of over 95% CO_2; lack of (significant) atmospheric water vapor and accompanying latent heat release; lack of liquid water and accompanying high thermal inertia; lack of strong magnetic field; and an average surface pressure of 6.1 hPa (Haberle 2003; Leovy 2001). Table 1 compares planetary and atmospheric parameters for Earth and Mars. Surface temperatures range from 150 to 275 K, and surface pressure varies seasonally by up to 20% due to CO_2 condensation at the poles during winter and sublimation during spring and summer (James *et al.* 1992; Zurek *et al.* 1992). The CO_2 cycle is driven by seasonal changes in insolation that produce similar water and dust cycles (Haberle 2003).

Table 1. Planetary and atmospheric parameters for Mars and Earth (Haberle 2003; Leovy 2001; Owen 1992; Read and Lewis 2004; Zurek *et al.* 1992)

Parameter	Mars	Earth
Mass (kg)	6.46×10^{23}	5.98×10^{24}
Semi-major axis, ($\times 10^6$ km) (AU)	227.9 1.52	149.6 1.0
Orbital eccentricity	0.093	0.017
Planetary obliquity (°)	25.19	23.93
Rotation rate, $\Omega\left(10^{-5} \cdot \mathrm{s}^{-1}\right)$	7.088	7.294
Solar day (s)	88 775	86 400
Year length (Earth days)	686.98	365.24

Equatorial radius, r_{eq} (km)	3 394	6 369
Surface gravity, $g\left(\mathrm{m\cdot s^{-2}}\right)$	3.72	9.81
Surface air pressure, p (hPa)	6.1*	1013
Constituents of lower (<120 km) atmosphere (molar ratio, %)	CO_2 (95) N_2 (2.7) ^{40}Ar (1.6) O_2 (0.13) H_2O (0.03)*	CO_2 (0.037) N_2 (77) ^{40}Ar (0.9) O_2 (21) H_2O (0–4)
Solar flux ("solar constant"), S_0 $\left(\mathrm{W\cdot m^{-2}}\right)$	589	1367
Radiative equilibrium temperature, $T_e\left(\mathrm{K}\right)$	210	256
Scale height, $H_p = \dfrac{RT_e}{g}\left(\mathrm{km}\right)$	10.8	7.5
Gas constant, $R\left(\mathrm{J\cdot kg^{-1}\cdot K^{-1}}\right)$	192	287
Specific heat at constant pressure, $c_p\left(\mathrm{J\cdot kg^{-1}\cdot K^{-1}}\right)$	831	1000
Dry adiabatic lapse rate, $\Gamma_d\left(\mathrm{K\cdot km^{-1}}\right)$	4.5	9.8
Mean lapse rate of lowest scale height, Γ (K km^{-1})	2.5	6.5
Buoyancy (Brunt–Väisälä) frequency, N (10^{-2} s^{-1})	~0.6	1.12
Bulk radiative timescale, τ_r (10^5 s)	2	40
Typical zonal wind at jet level, $U\left(\mathrm{m\cdot s^{-1}}\right)$	80	30

* Variable with season. $\bar{p} \approx 6.1$ hPa. Spatial and temporal range $\approx$ 4 – 10 hPa

Mars has an intrinsic magnetic field ~10^4 times weaker than that on Earth. Although Mars and Earth have similar rotation rates, Mars' planetary radius is 53% smaller (Table 1). The large difference in magnetic field strength is due to the weak dynamo activity in the Martian core. This results in significant losses of atmospheric constituents, especially lighter ones, due to solar wind scavenging (Luhmann *et al.* 1992).

Mars has a highly elliptical orbit (Fig. 2) with a mean radius of 2.28×10^{11} m and a mean distance from the sun of 1.5 astronomical units (AU), resulting in a mean solar constant (S_0) of 589 W m^{-2} (1380 W m^{-2} for Earth) (Read and Lewis 2004).

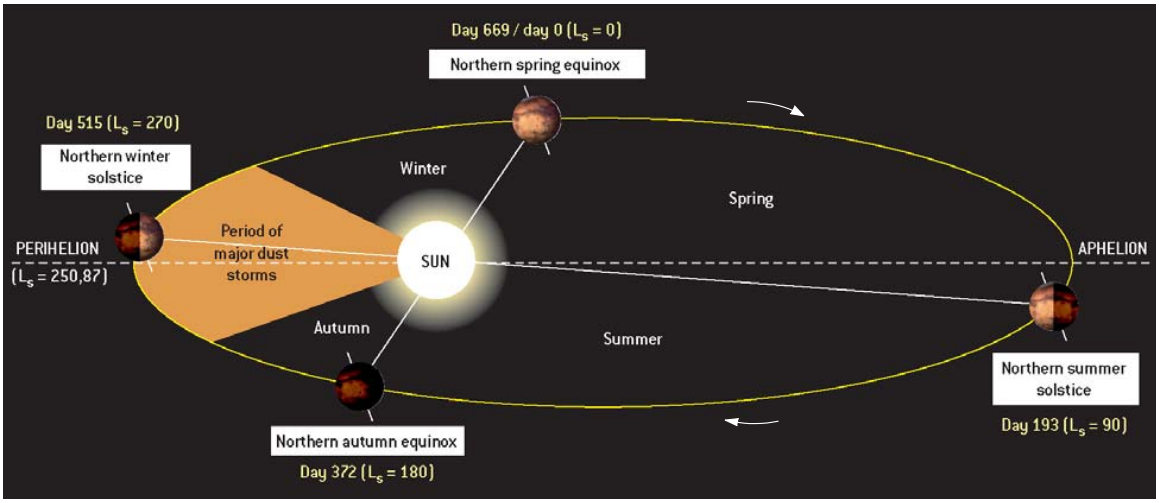

Figure 2. Martian orbit and seasons (reprinted with permission from Forget *et al.* 2008).

The insolation received at perihelion, however, is approximately 40% more that that received at aphelion due to the large degree of ellipticity. Atmospheric thermal structure and circulation are determined by daily and seasonal changes in insolation dependent on these orbital properties (Haberle 1997).

The fundamental unit of Martian time is the SI second, where the Martian day (sol) consists of 88 775 s. Each sol is divided into 24 Martian hours, equivalent to 24.63 Earth hours. Seasons are measured in degrees of areocentric longitude (L_s). NH spring equinox occurs at L_s=0°, summer solstice at L_s=90°, fall equinox at L_s=180°, and winter solstice at L_s=270°. SH seasons are reversed as on Earth, and thus SH spring equinox occurs at L_s=180°. During the spring equinox, one sol is ~0.6° of L_s. The Martian year consists of 686.98 sols, and is measured in Mars years (MY) that begin on L_s=0°. MY 1 starts at 11 April 1955, a date that was chosen because of planet-encircling dust storm observations that Mars year (Clancy *et al.* 2000; Read and Lewis 2004).

2.3 Atmospheric Properties and Circulation Components

The Martian atmosphere is composed primarily of carbon dioxide (95%), followed by nitrogen, argon, oxygen, carbon monoxide, and other trace gases (Table 1). Although CO_2 is the main constituent, greenhouse warming raises temperatures by only 5 K above the radiative equilibrium temperature of 210 K, partially due to the solar constant, but more importantly due to the narrow spectral band where the atmosphere absorbs radiation (Haberle 1997).

The atmosphere is characterized by the following layers: troposphere, mesosphere, thermosphere, and exosphere. The troposphere extends to almost 60 km and has a mean lapse rate of 6.5 K km^{-1}. This rate is less than the dry adiabatic lapse rate of 4.5 K km^{-1} due to additional heating produced from suspended aerosol particles (Haberle 2003). The mesosphere has an altitude range of 60–120 km, and lapse rates of nearly zero, due to warming and mixing produced by thermal tides (Haberle 2003; Leovy 2001).

Major components of the general circulation include the zonally symmetric mean meridional circulation, stationary and propagating planetary waves, thermal tides, jet streams, and CO_2 mass flow due to seasonal polar cap sublimation and condensation (Haberle *et al.* 1993). The Hadley circulation is characterized by equinoctial and solsticial modes (Fig. 3), with two symmetric cells at the equinoxes and a single cross-equatorial circulation from 30°S-30°N at the solstices (Haberle *et al.* 1993).

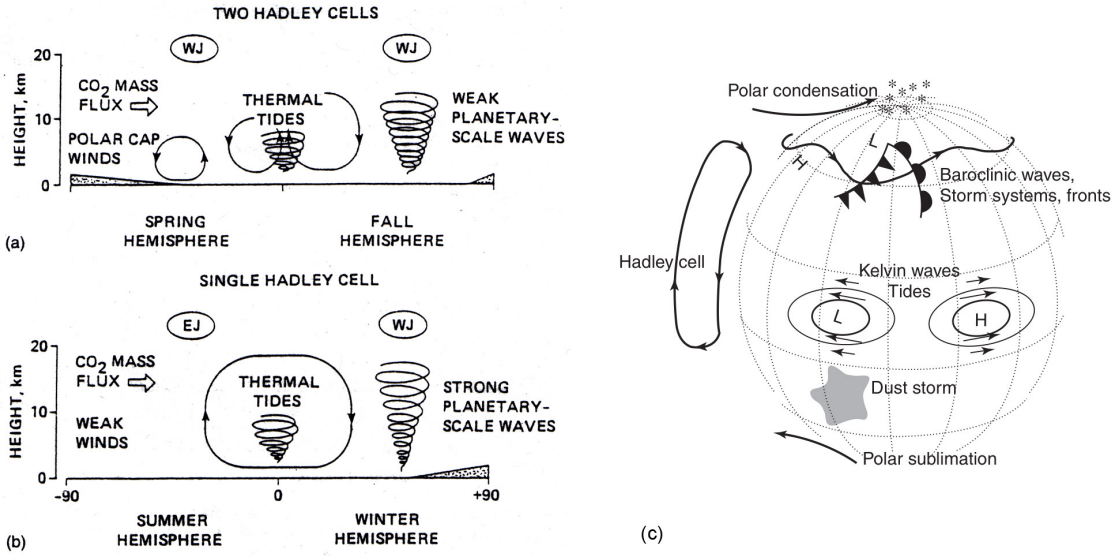

Figure 3. General circulation of the lower atmosphere at (a) equinoxes, and (b) solstices (reprinted with permission from Haberle 1997). (c) Atmospheric processes (reprinted with permission from Haberle 2003)

2.3.1 EXTRATROPICAL WEATHER SYSTEMS

Mars, like Earth, has extratropical weather systems (transient baroclinic waves) that transfer heat from low to high latitudes. Differential heating of the planet produces eastward-travelling baroclinic eddies that transfer heat via heat fluxes. Extratropical eddies are an important component of Martian general circulation and climate due to their role in the following systems: i) heat transport; ii) momentum transport; iii) water transport/cycle; iv) dust cycle; and v) PDS genesis (Barnes *et al.* 1993; Haberle 1986). Eddy-induced heat and momentum fluxes affect the general circulation by removing potential energy from the zonal-mean flow (Barnes *et al.* 1993).

Planetary waves in the NH polar vortex were inferred from Mariner 9 IRIS observations (Conrath 1981). NH transient eddies were inferred from photographs of 'front-like cloud structures' (Briggs and Leovy 1974), and observed by the Viking landers (VL) (Barnes 1981; Barnes 1980; Ryan *et al.* 1978). Viking surface observations were the first that allowed correlations between pressure, wind, and temperature. From these analyses, (Ryan and Henry 1979) deduced the presence of eastward-traveling waves with zonal wavenumbers, m, from 4 to 6, and phase speeds, c, of 5–15 m s^{-1}, while (Barnes 1981) found phase speeds of 10–20 m s^{-1}.

TES observations enabled the first global perspective on daily weather variability. Transient eddies (traveling waves) were observed by MGS in the southern (Hinson and Wilson 2002) and northern hemispheres (Hinson and Wang 2009; Wang *et al.* 2003). SH m=3 traveling waves with phase speeds of 10–20 m s^{-1} were inferred from MGS radio-occultation profiles (Hinson and Wilson 2002). Amplitudes with a maximum of 7 K were found in a storm zone from 150–300° E. Banfield *et al.* (2004) identified travelling wave signatures in the SH in MY 24 and 25.

Both NH and SH transient activity seen in FFSM analysis of TES data are characterized by the following zonal wavenumber and period modes: m=1 with 6–10 sol periods, m=2 with 3–5 sol periods, and m=3 with 2–3 sol periods (Barnes 2006). These modes are similar to those observed by Viking (Barnes 1981; Barnes 2006). Eddies in both hemispheres exhibit significant seasonal and interannual variability.

The relationship between baroclinic eddies and the dust cycle is not fully understood, though it is hypothesized that two regimes exist (Haberle 1986; Leovy *et al.*

1985). The first regime is characterized by SH dust storms at ~ L_s=200° that lift dust into the cross-equatorial Hadley circulation, causing it to strengthen and shift poleward, along with the location of the steepest meridional temperature gradient. Baroclinic wave activity is suppressed, and the location of maximum wave activity also shifts poleward (Leovy *et al.* 1985). The second regime is characterized by intense NH baroclinic wave activity that generates regional mid-latitude dust storms, but no global dust storms (Leovy *et al.* 1985).

2.3.2 STORM ZONES

Hollingsworth *et al.* (1996) first predicted storm zones in numerical simulations and identified orography as an important determining factor. SH winter–spring storm zones have subsequently been inferred from TES observations. Hinson and Wilson (2002) inferred a storm zone from ~150–330° E from zonal variations in MY 24 eddy amplitudes. Banfield *et al.* (2004) identified a persistent storm track during MY 24 and 25 from 210–300° E, located between the Tharsis ridge and Argyre basin (Fig. 1). Barnes (2003, 2006) identified SH winter storm zones from TES FFSM variance data in the ~200–300° E region. NH winter (~L_s=237–270°) storm zones have been identified in the Acidalia, Utopia, and Arcadia lowlands (~300–360°E and 120–180°E) from TES FFSM variance data (Barnes 2006).

The origin of SH storm zones is not well understood. MGCM simulations conducted by Hollingsworth (2005) suggest that SH transient barotropic/baroclinic eddies are modulated by topography. Argyre and Hellas basins perturb the mean potential

vorticity gradient, and since eddies derive their energy from this and (other gradients), orographic disruption significantly alters eddy structure and quality. These simulations also suggest that orographic modulation from the Tharsis highlands and Argyre basin contributes to the development of a western hemisphere storm zone, consistent with TES observations.

East-west longitudinal asymmetries are apparent in Compact Reconnaissance Imaging Spectrometer for Mars (CRISM) observations of SH CO_2 and H_2O distributions (Hollingsworth *et al.* 2008). Hollingsworth *et. al* (2008) conducted MGCM simulations of the water cycle and found SH east-west longitudinal asymmetries of water vapor, water ice clouds, (and other quantities). Eddy activity was greatest (weakest) in the western (eastern) hemisphere.

2.4 Atmospheric Aerosols

Suspended dust particles absorb and scatter incoming solar radiation, absorb and emit IR radiation, strengthen global meridional circulation, and change atmospheric thermal structure (Haberle *et al.* 1982). IR radiation from aerosols is also absorbed and re-emitted by CO_2, which causes warming in the surrounding air (Kahn *et al.* 1992). Microwave observations of MY 21 and 22 regional dust storms indicate abrupt 10–30 K global temperature increases to altitudes above 50 km (Clancy *et al.* 2000).

IR spectroscopy indicates that dust may be composed of magnetite (Pollack *et al.* 1979), montmorillonite and basalt (Toon *et al.* 1977), and palagonite-like minerals (Clancy *et al.* 1995). Soil analysis from Viking (Banin 1993) and Mars Pathfinder

(Wanke *et al.* 2001) sites indicated iron oxide (Fe_2O_3) proportions of ~19 and 22% (by mass), and silicon (SiO_4, SiO_2) proportions of ~40 and 42% respectively.

2.4.1 DUST LIFTING AND FEEDBACKS MECHANISMS

The two main mechanisms thought to transport dust into the atmosphere are saltation and convective vortices (dust devils). Saltation is the process by which surface winds lift large (20–100+ μm) particles that rapidly fall out due to sedimentation, but dislodge and lift smaller (~1μm) particles upon impact. These may remain suspended due to eddy wind fluctuations (Gierasch and Goody 1973; James 1985; Read and Lewis 2004). Near-surface wind stress is a quantity used by numeric modelers in determining thresholds for lifting due to saltation. Dust devils are convective vortices that have a low pressure core with strong updrafts that lift and entrain particles of all sizes from the surface. Viking lander wind speed measurements of passing dust devils were as high as 25 ms^{-1} in 6% of cases (Read and Lewis 2004). Although dust devils are thought to play an important role in maintaining background opacity (τ_d) levels, they are not thought to be a major contributor to PDS initiation.

Once dust is lifted above the surface, it is possible that a radiative–dynamical feedback occurs that supports further lifting. Increased heating due to suspended dust may increase induced vertical wind, transporting warm air upward and bringing in cooler air below, subsequently increasing surface winds and further lifting dust. Vertical velocity, w, is proportional to the solar heating rate, Q_T, as in: $w \sim Q_T / N^2$, where N is the Brunt–Väisälä or buoyancy frequency (Rafkin 2009; Read and Lewis 2004). Newman *et*

al. (2002b) found a strong positive non-linear feedback in near-surface wind stress in numerical simulations of the saltation mechanism. Heating of optically-thick dust increases turbulence and convection that subsequently entrains more particles (James 1985). Rafkin (2009) conducted numerical simulations that also produced a positive radiative-dynamic feedback mechanism under certain conditions, including steep background lapse rates and modest dust-lifting thresholds.

A feedback mechanism involving particle-laden gravity currents has been hypothesized to explain rapid dust storm growth (Parsons 2000). A gravity (or density) current occurs when a greater-density fluid flows within a lesser-density fluid. The density difference is the force that maintains these buoyancy-driven flows (Simpson 1982). Lobes and clefts are morphological features seen in the leading edges of terrestrial gravity currents (e.g. turbidity currents), and are visible in many Martian dust storms. James (1985) reported that south polar cap edge and Solis Planum dust storms observed by Viking are characterized by a well-defined lobate-structured leading edge, analogous to terrestrial haboobs that are produced by density currents of underlying cold air. Proposed Martian dust storm generation mechanisms involve cold air flows undercutting warmer air that would produce sharp, lobate edges (James 1985). Parsons (2000) hypothesized that collapse of a dust devil can lead to an initial particle-laden gravity current. Mechanisms for particle entrainment and rapid storm growth also include laterally propagating compressional shock waves (Parsons 2000) and hydraulic jumps (Timmermans *et al.* 2001).

2.4.2 DUST STORM CHARACTERISTICS

Observations indicate an association between south polar cap recession and dust storm genesis (Cantor *et al.* 2001; Fernandez 1999; Martin and Zurek 1993). South polar cap recession (data through 1969) begins at ~L_s=120° (~40° S) and continues through ~L_s=270° (~80° S) (Martin and Zurek 1993). Local storms are regularly generated along the cap edge between Argyre and Hellas during southern spring. James (1985) hypothesized that the primary dust-lifting mechanism is CO_2 sublimation-induced wind, whereas secondary mechanisms are topographically-enhanced winds, baroclinic waves, and dust devils. These circulation components are augmented by differential surface heating due to albedo differences between CO_2 ice and exposed soil, as well as pressure/temperature gradients due to polar cap recession (Briggs *et al.* 1979; Cantor 2007; Haberle *et al.* 1979; Strausberg *et al.* 2005). Models suggest that these strong gradients between the south polar cap and ice-free soil to the north produce diurnally varying baroclinic zones with strong polar cap circulations (*cf.* terrestrial sea breeze) sufficient for dust lifting (Burk 1976; Fernandez 1999; Haberle *et al.* 1979; Leovy *et al.* 1972; Siili *et al.* 1999; Toigo *et al.* 2002), along with high stresses in the southwest corner of Hellas during SH spring (Newman *et al.* 2002a; Newman *et al.* 2002b). Moreover, CO_2 sublimation-induced outflow increases wind shear and may produce turbulence capable of raising dust (James 1985). Furthermore, the topography of Hellas and Argyre basins may augment dust lifting due to higher surface pressure and corresponding lower friction velocity thresholds. In the Claritas/Solis Planum region, primary dust-lifting mechanisms are thought to be slope winds and thermal tides, while

secondary mechanisms are internal gravity waves and convection enhancement (James 1985).

Although regional dust storms occur throughout the year, they are most prevalent in the dust storm season from L_s=161–326° (Fernandez 1999; Martin and Zurek 1993). Perihelion occurs in the middle of this season (~L_s=251°) and is a factor in dust storm initiation due to maximum SH diurnal heating during this period. Regional storms generally decay within two weeks (Martin 1984).

2.4.3 PLANET-ENCIRCLING DUST STORMS

The largest atmospheric aerosol phenomenon is the global dust storm, alternately classified as a planet-encircling dust storm (Cantor 2007; Gierasch 1974; Strausberg *et al.* 2005). Cantor (2007) emphasizes that these events do not have a single locus of dust-lifting, but instead are composed of numerous lifting centers.

Although PDSs occur on an irregular basis, all well-documented storms have begun within ± 75° L_s from perihelion (L_s=251°), when insolation is greatest near the SH summer solstice (L_s=270°) and the south polar cap is receding. These storms were at: L_s=249° (1956), L_s=260° (1971-1972), L_s=300° (1973), L_s=204° (1977a), L_s=268° (1977b), and L_s=176° (2001) (Cantor 2007; Kahn *et al.* 1992; Martin and Zurek 1993). There is Earth-based microwave evidence that PDSs also occurred in 1992 and 1994 (Clancy *et al.* 1994; Clancy *et al.* 1996). Major PDS emergence regions include the Hellas and Argyre basins, Isidis Planitia, and Claritas Fossae (Cantor 2007; Ebisawa and Dollfus 1986).

Planet-encircling dust storms profoundly affect climate on all time scales: seasonal, annual, and millennial. They change the thermal structure of the atmosphere by lowering temperatures near the surface due to absorption of incoming solar radiation, and by raising temperatures aloft, as discussed above. This subsequently affects the pressure, winds, and ultimately general circulation patterns (Haberle *et al.* 1982; Zurek *et al.* 1992). Dust entrained in the Hadley circulation causes rapid diabatic warming due to low atmospheric thermal inertia. Moreover, dust-induced heating in one hemisphere intensifies the Hadley circulation, which in turn causes dynamical adiabatic heating as the returning branch sinks in the high latitudes of the opposite hemisphere (Haberle *et al.* 1993; Smith *et al.* 2001).

The environmental causes and dynamical mechanisms responsible for PDS initiation, decay, and interannual variability are not fully understood (Haberle 1986; Ingersoll and Lyons 1993; Kahre *et al.* 2006; Smith *et al.* 2002). Numerous variables (and their multiple combinations) may play a role, including: microphysical variables such as dust placement in relation to surface roughness components; surface roughness (affects critical friction velocity); dust sources and sinks; background (pre-storm) opacity levels; cap location, transient eddy amplitudes and phases; and the general circulation (Haberle *et al.* 1982; Ingersoll and Lyons 1993; Zurek and Martin 1993).

Leovy *et al.* (1973) hypothesized that constructive interference of circulation components may be responsible for PDS genesis. These components include transient baroclinic eddies, cap-edge sublimation winds, topographically-enhanced winds in the Hellas basin, and thermal tides. Weather variability may also be a critical factor.

Observed dust lifting near the VL-1 lander, for example, was thought to be due to unusually high winds produced from constructive phasing of the diurnal thermal tide and strong baroclinic waves (Arvidson *et al.* 1983).

The seasonal occurrence of PDSs suggests the presence of climatic/environmental precursors and components, yet interannual variability suggests that initiation and expansion mechanisms are not solely seasonal in character (Zurek and Martin 1993). Martin and Zurek (1993) hypothesize that cap recession interannual variability is evidence for an interrelationship between cap location and dust storm initiation.

Zurek and Martin (1993) estimate PDS frequency to be roughly one per three Mars years, with ~50% probability that a PDS will occur in any given Mars year, and an 18-55% (5σ) probability range considering all 1924–1983 observations. Year-to-year variability of general circulation patterns is thought to be small (Newman *et al.* 2004), leading Montabone *et al.* (2005) to hypothesize that PDS interannual variability may be largely determined by local meteorological conditions and feedbacks. Montabone *et al.* (2005) studied dust storm interannual variability with assimilated TES data and found large near-surface wind stresses in Hellas and Tharsis during MY 25 simulations compared to other years.

Uncertainty remains regarding PDS interannual variability. Are PDSs periodic or aperiodic, *i.e.* chaotic: governed by highly nonlinear, stochastically forced systems (Zurek and Haberle 1988)? Ingersoll and Lyons (1993) state that PDSs do not seem to be periodic, though statistics are limited. If PDSs are periodic, what environmental causes and dynamical mechanisms are responsible?

3 MGS Data and Analysis Methods

3.1 Thermal Emission Spectrometer

TES is an interferometric spectrometer that measures thermal emission in the IR spectrum from 6-50 μm (wavenumbers 1600-200 cm^{-1}) with 5 and 10 cm^{-1} nominal spectral resolutions (Christensen *et al.* 2001; Christensen *et al.* 1992). There are six detectors and each has an 8.3 mrad field of view, yielding a spatial resolution of ~3 x 9 km on the surface (Smith *et al.* 2002). Spectral data are used to retrieve the following quantities: temperature (surface and atmospheric), optical depth (dust and water ice aerosol), and water vapor column abundance (Smith *et al.* 2000). Atmospheric thermal retrievals were obtained from 3.7–0.01 hPa, approximately 5.4–70.4 km (Table 2). We refer to 9-μm (IR) dust optical depth hereafter as 'opacity' (τ_d). All opacity retrievals have been normalized to remove the effects of topography. The values of visible-to-IR opacity ratios derived from various datasets range from: 1.69 (Hunt *et al.* 1980), to 1.85 (Zurek 1982), and 2.5 (Martin 1986). We use a value of 2 when comparing visible opacity observed by Cantor (2007).

Table 2. Martian atmospheric pressure levels and height estimates. TES nadir retrievals span the surface to 0.11 hPa, while limb retrievals span 1.36–0.01 hPa.

Pressure level (hPa)	~Log pressure height (km) $z^* \equiv H \ln(p_r/p)$	TES nadir height description
0.01	70.4	

0.015	64.9	
0.025	59.4	
0.041	54.0	
0.068	48.6	
0.11	43.4	Upper
0.18	38.0	Upper
0.3	32.5	Middle
0.5	27.0	Middle
0.83	21.5	Middle
1.36	16.2	Middle
2.24	10.8	Lower
3.7	5.4	Lower
6.1	~0 (mean surface level)	

TES viewing geometries include nadir and limb (forward and aft). TES temperature retrievals occur at ~ 0200 and 1400 local time, though this varied at high latitudes. The spatial and temporal resolution and coverage of TES observations greatly exceed those of previous spacecraft (Smith *et al.* 2001; Smith *et al.* 2002).

Retrieval algorithms for atmospheric temperatures are described by (Conrath *et al.* 2000) and for dust opacity by (Smith 2004; Smith *et al.* 2000). A brief description is given below. Atmospheric temperature and aerosol optical depth retrievals are calculated sequentially (Smith *et al.* 2001). Atmospheric temperature profiles $T(p)$ are obtained from thermal emission spectra within the CO_2 absorption band (Fig. 4) centered at 15-μm (550–800 cm^{-1}) (Conrath *et al.* 2000). Atmospheric dust has absorption bands between 800–1300 cm^{-1} and 300–550 cm^{-1} (Smith *et al.* 2000).

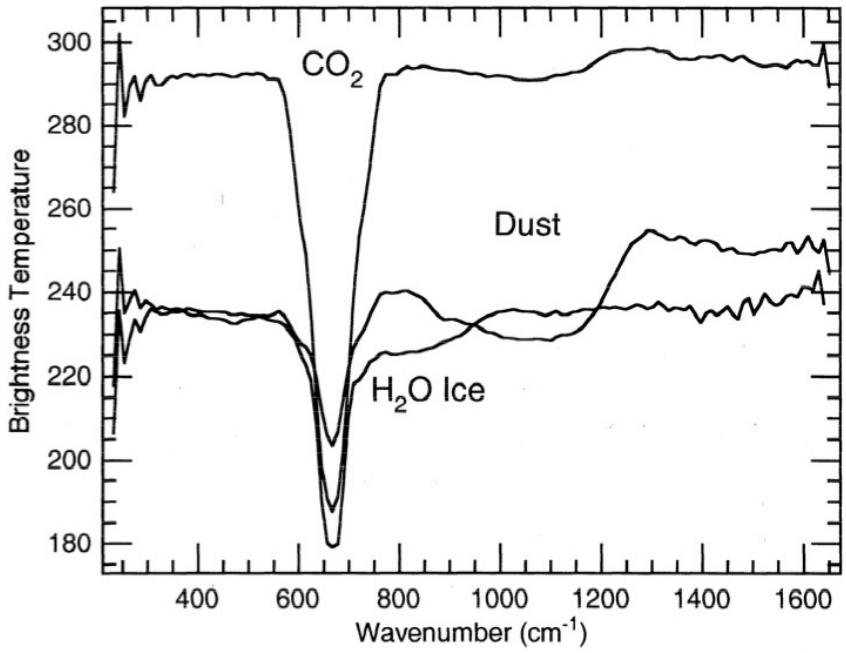

Figure 4. Daytime TES spectra (reprinted with permission from Smith *et al.,* 2000)

Radiance $I(\mu,\nu)$ measured by TES at the top of the atmosphere is formulated as

$$I(\mu,\nu) = \varepsilon(\nu)B(\nu,T_s)Tr(\mu,\nu,z_s) + \int_{z_s}^{z_t} B[\nu,T(z)]\frac{\partial Tr(\mu,\nu,z)}{\partial z}dz \qquad (1)$$

where μ is the cosine of emission angle, ν is wavenumber, $\varepsilon(\nu)$ is surface emissivity at frequency ν, $z = -\ln p$, p is atmospheric pressure, $Tr(\mu, \nu, z)$ is atmospheric transmittance from level z to the top of atmosphere, and $B(\nu, T)$ is the Plank radiance at wavenumber ν and temperature T (Conrath *et al.* 2000).

Atmospheric attenuated surface emission is represented by the first RHS term in Eq. (1), and atmospheric emission by integration of the second RHS term. Equation (1) represents a simplified radiative transfer equation that neglects scattering and surface

fluxes. Estimates for surface pressure and temperature are required to perform the retrieval (Conrath *et al.* 2000). An effective surface temperature is estimated by averaging brightness temperatures on either side of the CO_2 band. This observation is an underestimate due to non-zero atmospheric extinction.

Solving Eq. (1) for $T(z)$ is an inverse problem that requires linearization and low-pass filtering constraints (Conrath *et al.* 2000). This process yields retrievals from 3.7–0.1 hPa (~5–35 km) for each nadir spectrum, and from 1.36–0.01 hPa (~16-65 km) for each limb spectrum (Smith *et al.* 2001). Vertical resolution however is limited to ~ one scale height (~10 km) for nadir profiles and 1–2 scale heights for limb. Temperature uncertainty is ~ 2 K in the middle atmosphere, and greater in the lowest and highest scale height (Christensen *et al.* 1992; Smith 2004).

After an atmospheric temperature retrieval has been calculated, an opacity retrieval is calculated with the following radiative transfer equation:

$$I_{\text{comp}}(\nu) = \varepsilon(\nu) B\left[T_{\text{surf}}, \nu\right] e^{-\tau_0(\nu)/\mu} + \int_0^{\tau_0(\nu)} B\left[T(\tau), \nu\right] e^{-\tau/\mu} d\tau \qquad (2)$$

where I_{comp} is radiance (computed) as a function of wavenumber, $\varepsilon(\nu)$ is surface emissivity at frequency ν, $B\left[T, \nu\right]$ is the Plank function, T_{surf} is surface temperature, $\tau_0(\nu)$ is normal column-integrated aerosol optical depth, μ is the cosine of the emission angle, and $T(\tau)$ is atmospheric temperature found by integrating from the spacecraft $(\tau = 0)$ to the surface $(\tau = \tau_0)$ (Conrath *et al.* 2000; Smith 2004). The first RHS term in Eq. (2) determines atmospheric attenuation ($e^{-\tau_0(\nu)/\mu}$) of surface radiance,

$\varepsilon(\nu)B\left[T_{surf},\nu\right]$, while the second term calculates attenuation ($e^{-\tau/\mu}$) of upwelling emission from atmospheric layers.

Dust opacity is obtained from spectral measurements near 1075 cm^{-1}, the center of a broad dust absorption band (Fig. 4). Required inputs are atmospheric temperature $T(z)$, calculated above from Eq. (1), and surface temperature, estimated from a relatively transparent spectral window near 1300 cm^{-1} that yields maximum brightness temperature (Smith *et al.* 2000).

Both retrieval algorithms incorporate three simplifying assumptions: 1) well-mixed mineral aerosols; 2) fixed spectral functions/shapes; 3) negligible aerosol scattering (Conrath *et al.* 2000; Smith 2004). The third assumption implies retrieval of an effective absorption opacity rather than full extinction opacity (absorption + scattering), as seen by the lack of scattering terms in (1) and (2). The validity/reliability of this assumption is a function of actual opacity, where validity decreases with increasing opacity. In low opacity conditions ($\tau_d \leq 0.25$), predicted values underestimate actual by 10–25%, and by ~20% at high opacities (Bandfield and Smith 2003; Smith *et al.* 2000). It is thus likely that TES MY 25 PDS opacity measurements are underestimates (Elteto 2009; Wolff and Clancy 2003).

A sampling resolution of 10 cm^{-1} was used during MY 24 and 26, and 5 cm^{-1} resolution during MY 25. Although no significant differences between the two resolutions were seen in surface and 0.5 hPa temperature retrievals (Smith 2003), MY 25 near surface afternoon temperatures were significantly cooler as a result (Wilson). The majority of temperature profiles were obtained from nadir-viewing spectra, yielding ~

19,000 retrievals per pressure level per sol, while limb spectra yielded ~ 50 retrievals per pressure level per sol. Limb retrievals are available every ~10° of latitude (Smith *et al.* 2001).

TES opacity retrieval reliability is partially a function of ground-air temperature contrast, with reliability diminishing as contrast approaches zero. Contrast limits occur at high-latitudes (>55°N, <60°S), and in extremely dusty conditions. Significant portions of the TES retrievals are missing or unreliable due to high opacity levels and diminished contrast.

3.2 Fast Fourier Synoptic Mapping

FFSM is a spectral analysis method that creates synoptic maps from asynoptic data, maintaining full space-time resolution without distorting or smoothing higher frequency (~1–3 sols) weather signals (Barnes 2001, 2003, 2006). This process removes the time mean, zonal mean, and westward diurnal tide. We analyzed FFSM-filtered MY 24–26 TES temperature data produced by Barnes (2003, 2006). As a result of this analysis, we produced longitude-time plots of TES 3.7 hPa temperature anomalies at 60° S for a desired L_s range. These are presented and discussed fully in Chs. 4 and 5.

3.3 Mars Orbiter Camera

The MOC consists of three push-broom cameras: a single, high-resolution narrow-angle (NA) camera with a broadband visible filter (500–900 nm), and two lower-resolution wide-angle (WA) cameras with red (575–625 nm) or blue (400–450 nm) band passes (Malin *et al.* 1992). The push-broom method constructs images one line at a time

as opposed to capturing a single frame. Malin Space Science Systems (MSSS) provided MOC DGMs that were created by map projecting (cylindrical) and mosaicking 12–13 global swaths (WA) (both red and blue band passes) of all daytime orbits (Cantor 2007). Each DGM is 3600 x 1800 pixels, with 10 pixels degree^{-1} resolution.

3.4 Mars Horizon Sensor Assembly

MHSA is an MGS engineering instrument that measures 15-μm CO_2 band emission to monitor the limb in order to adjust spacecraft pitch and roll alignment (Martin 1997; Martin and Murphy 2003). Data collected have also been used to study atmospheric density, thermal structure (Albee 2001; Albee *et al.* 1998; Martin 1997), and dynamics, particularly eastward and westward travelling diurnal and semi-diurnal waves/thermal tides (Murphy *et al.* 2001).

Atmospheric temperatures can be simultaneously derived from measurements made in four quadrants: aft (Q1), forward (Q2), right (Q3) and left (Q4). These are made at three local times each night/day: 2 am/pm (Q1 and Q2), 12:30 am/pm (Q3/Q4), and 3:30 am/pm (Q4/Q3) respectively (Murphy 2010). MHSA uses a broad weighting function that averages a region of the atmosphere 10–40 km above the surface. Advantages of MHSA data, from a meteorological perspective, include greater longitudinal and temporal coverage, while disadvantages include limited vertical resolution and sampling (Murphy 2010). MHSA data are also valuable because they contain continuous measurements throughout a 2–sol period (L_s=189.7–191.4°) of missing TES data.

MHSA and TES mid-level (0.5 hPa) temperature data are generally consistent (based on our analysis). The main differences are weaker horizontal temperature gradients and less noise in MHSA data due to the deep weighting function used for retrievals (10-40 km). TES data tend to be warmer in low to midlatitudes, and colder in polar regions compared to MHSA.

3.5 Data Analysis Methodology

In order to investigate this wealth of data, the following plots were generated:

- longitude-height cross sections of temperature and static stability (5° latitude spatial resolution)
- MOC DGMs with superimposed contours of
    - TES nadir temperature
    - TES opacity
    - MHSA temperature
    - environmental lapse rate
- time histories of TES nadir temperature, opacity, and MHSA temperature at various spatial resolutions (30 x 5°; 10 x 10°) for both the entire time domain (L_s=169.8–264.0°) and a subset (L_s=175.1–200.4°)
- TES nadir and limb temperature profiles (every 25 x 5°) with 10 consecutive days overlaid on a single plot, 60 days total
- height-time cross sections of TES nadir temperature
- zonally averaged temperature.

Here we present selected plots to illustrate key aspects of PDS evolution. When important TES opacity data are missing, MGCM-derived opacity plots are presented. Mars Orbiter Laser Altimeter (MOLA) topography (select heights) is represented on MOC DGMs by black contours.

3.5.1 STABILITY

We calculated static stability, *S*, from TES mean layer temperatures using the following formulation (Zurek *et al.* 1992):

$$S = R\left(\frac{\kappa T}{H} + \frac{dT}{dz^*}\right), \tag{3}$$

where *R* is the Mars gas constant, $\kappa = R/c_p$, c_p is specific heat at constant pressure, $H = RT/g$ is atmospheric scale height (~10.8 km), *T* is mean layer temperature, *g* is gravitational acceleration, and dT/dz^* is the environmental lapse rate using the pressure-based (*p*) vertical coordinate, $z^* \equiv H \ln\left(p_r/p\right)$, where p_r is the reference mean surface pressure of 6.1 hPa. Rearranging (3) yields:

$$S = \left(\frac{R\kappa T}{H} + R\frac{dT}{dz^*}\right). \tag{4}$$

Substituting $H = RT/g$ yields:

$$S = \left(\kappa g + R\frac{dT}{dz^*}\right). \tag{5}$$

Substituting $\kappa = R/c_p$ yields:

$$S = R\left(\frac{g}{c_p} + \frac{dT}{dz^*}\right). \tag{6}$$

Substituting Mars' dry adiabatic lapse rate, $\Gamma_d \equiv g/c_p$, allows static stability to be formulated as $S = R\left(\Gamma_d + dT/dz^*\right)$, or simply

$$S^* = \Gamma_d + \frac{dT}{dz^*}, \tag{7}$$

since *R* is constant. For stable conditions, the environmental lapse rate is limited to: $dT/dz^* \geq -g/c_p = -4.5\ \mathrm{K \cdot km^{-1}}$. Mars orbital and atmospheric parameters are given in Table 1.

Since scale height decreases with increasing altitude and decreasing temperature (Read and Lewis 2004), a constant reference scale height, H_r, was not used. Instead, mean layer temperature was calculated from 5° x 10° (lat. x lon.) binned data, allowing $H = RT/g$ to be computed for each bin, and then zonally averaged for each layer, two times per day. The above definition for z^* allows dT/dz^* to be discretized as $\Delta T/\Delta z$, and thus S^* to be computed. Results are discussed in Ch. 4.3.

3.5.2 PHASE SPEED AND PERIODICITY

We subjectively defined globally-coherent eddies and calculated their phase speed, *c*, using: $c(x) = \Delta x/\Delta t$, where $\Delta x = (r_{eq} \cdot \cos\varphi) \cdot \Delta\lambda$, r_{eq} is planetary radius, φ is latitude, λ is longitude, and *t* is time at 180° E. We estimated MY 24–26 eddy

periodicities, *P*, in Hellas from FFSM longitude-time plots. Periodicities were also calculated by Fast Fourier Transform in IDL using:

$$F(u) = \frac{1}{N}\sum_{x=0}^{N-1} f(x) e^{-i2\pi u \frac{x}{N}}, \tag{8}$$

where $F(u)$ is the discrete Fourier transform of an N-element, one-dimensional function, $f(x)$. These results are discussed in Ch. 5.5.

3.5.3 DATA VISUALIZATION

Effectively visualizing large, multi-dimensional datasets can be challenging. To address this problem, the above plots were designed to be viewed on the NASA-Ames Hyperwall, a node in the NASA Columbia supercomputer with a 7×7 matrix of 49 monitors created to efficiently visualize and navigate through multi-dimensional datasets. In addition, custom tools for this project were developed by Columbia scientists that allowed us to easily juxtapose various dimensions by interleaving data by row or column, including: times of day; physical quantities (temperature, dust opacity, pressure); instruments (TES vs. MHSA); and observations vs. MGCM output. The combination of these software and hardware systems enabled us to visualize the storm from local to global scales, enhancing our ability to efficiently examine the evolution of the temperature and opacity fields, and to locate regions and signals of interest from large numbers of high-resolution plots.

3.6 Missing Data and Synthesized Dust Maps

TES opacity retrieval reliability is partially a function of surface-air temperature contrast, with reliability diminishing as contrast approaches zero. This known limitation results in significant data gaps, especially at high latitudes (>55° N, <60° S), and in extremely dusty conditions (Smith 2004). As a result, data from the meteorologically-significant periods of lifting onset and expansion in both Hellas and Claritas are unreliable, including the majority of retrievals south of 30–45° S in Hellas from L_s=185–191°, as well as those from Daedalia and Solis Plana from L_s=191–210° during the rapid expansion of the Claritas storm. In addition to these partial data gaps, TES opacity data is completely missing for 4 sols in Hellas (L_s=189.3–191.4°) and 3 sols in Claritas (L_s=189.7–191.5°).

We believe that an improved opacity "sequence" would increase the credibility and reliability of numerical simulations. We have thus developed a qualitative and quantitative description of storm evolution that may be used to constrain horizontal dust distribution, and model storm initiation and expansion (Noble *et al.* 2007; Wilson *et al.* 2008). We produced two synthesized dust maps: column opacity and structured opacity. Column opacity maps estimate atmospheric column opacity at each grid point from a range of 15 possible levels (τ_d = 0.2, 0.4, 0.6, …, 3.0). Structured opacity maps delineate latitude-longitude boundaries where cloud top morphology is visibly structured. These regions are suggestive of convective activity and possibly of active lifting (Strausberg *et al.* 2005), and are designed to be used as proxies for dust lifting locations in MGCM simulations. Both maps were produced for L_s=184.1, 185.8, 186.4, 187.5, 189.2, 191.6,

193.3, 195.1, 200.4, and 205.2°, while structured opacity maps were additionally generated for L_s=184.6, 186.9, and 185.2°. See Ch. 6 for a detailed description of SDM development and results.

4 MY 25 PDS Observations

4.1 Overview

Cantor (2007) inferred a sequence of storm activity from an analysis of MOC opacity data and DGMs, and classified storm evolution into three phases: 1) precursor, L_s=176.2–184.6°, sols 1–15; 2) expansion, L_s=184.7–200.3°, sols 16–42; 3) decay, L_s=200.4–263.4°, sols 43–140. Here we propose the following PDS phases: 1) precursor, L_s=176.2–184.7°; 2) expansion, L_s=184.7–193°; 3) mature, L_s=193–210°; 4) decay, L_s=210–263°. Figure 5 shows the evolution of TES globally-averaged temperatures and opacity.

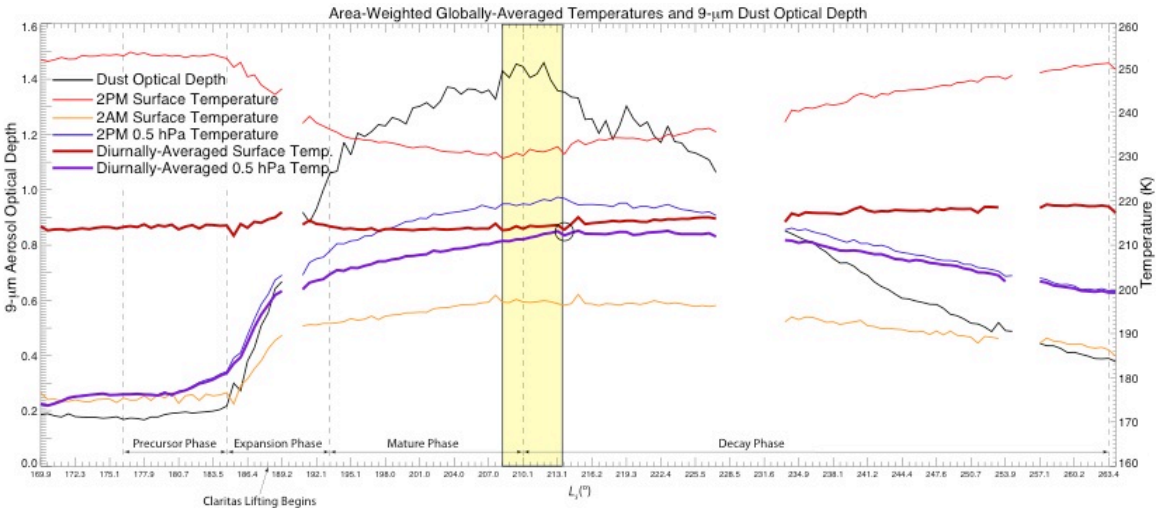

Figure 5. Area-weighted, globally-averaged TES temperatures and 9-μm dust optical depth from L_s=169-263°. Shaded area represents time when quantities reach maxima or minima.

This classification has the expansion phase ending at L_s=193°, when total lifting area peaked (Cantor 2007), and introduces a mature phase that ends at L_s=210°, the time of peak globally-averaged opacity and temperature (surface and 0.5 hPa). The shaded area in Fig. 5 shows the extrema of opacity at L_s=212°, 2 pm 0.5 hPa temperature at L_s=213°, and 2 pm surface temperature at L_s=208°.

Steep opacity and temperature changes are apparent in the first half of the expansion phase (Fig. 5), where rising opacity levels cause 0.5 hPa 2 pm temperatures to increase due to IR emission from dust at that height. A downward trend in surface temperature was observed during the expansion and mature phases due to absorption of solar radiation aloft and subsequent blocking at the surface. Diurnally-averaged surface and 0.5 hPa temperatures are nearly isothermal (~213 K, circled) at L_s=213° (Fig. 5).

4.2 Precursor Phase L_s=176.2–184.6°

Pre-storm background dust optical depth values of τ_d = 0.1–0.3 were typical of the season. Two storms were observed at L_s=176.2° (sol 1): a local storm that originated in central Hellas (42.5°S, 61.6°E) and a second in Malea Planum (58.2°S, 76.9°E) at the polar cap edge (note CO_2 ice obscuration) (Fig. 6a).

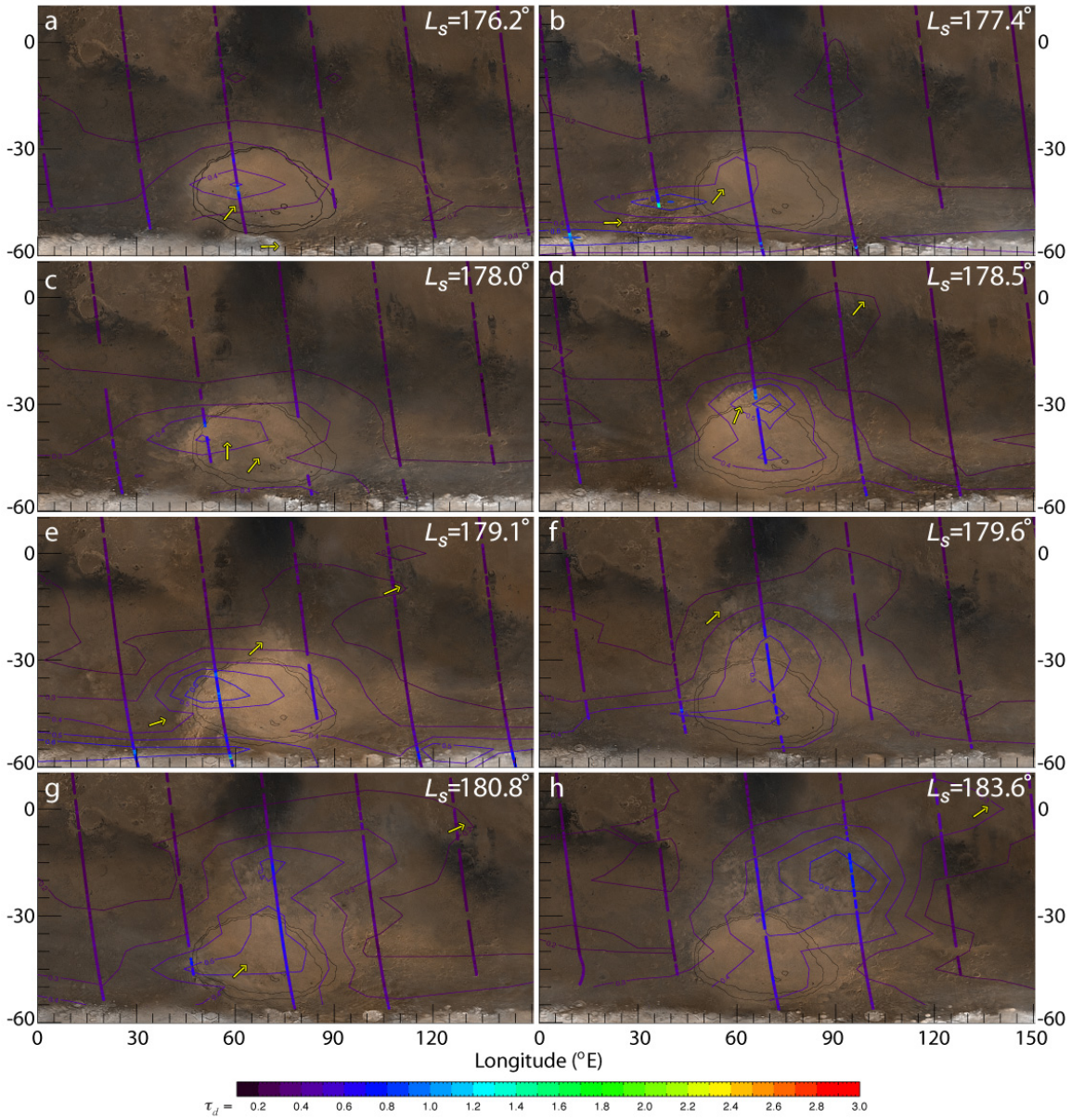

Figure 6. TES (a, c, d, f, g, h) and MGCM-derived (b, e) opacity on MOC DGMs, L_s=176.2–183.6°. Arrows indicate dust storms and dust transport.

These storms are associated with a transient eddy (E1) propagating through Hellas (Fig. 7).

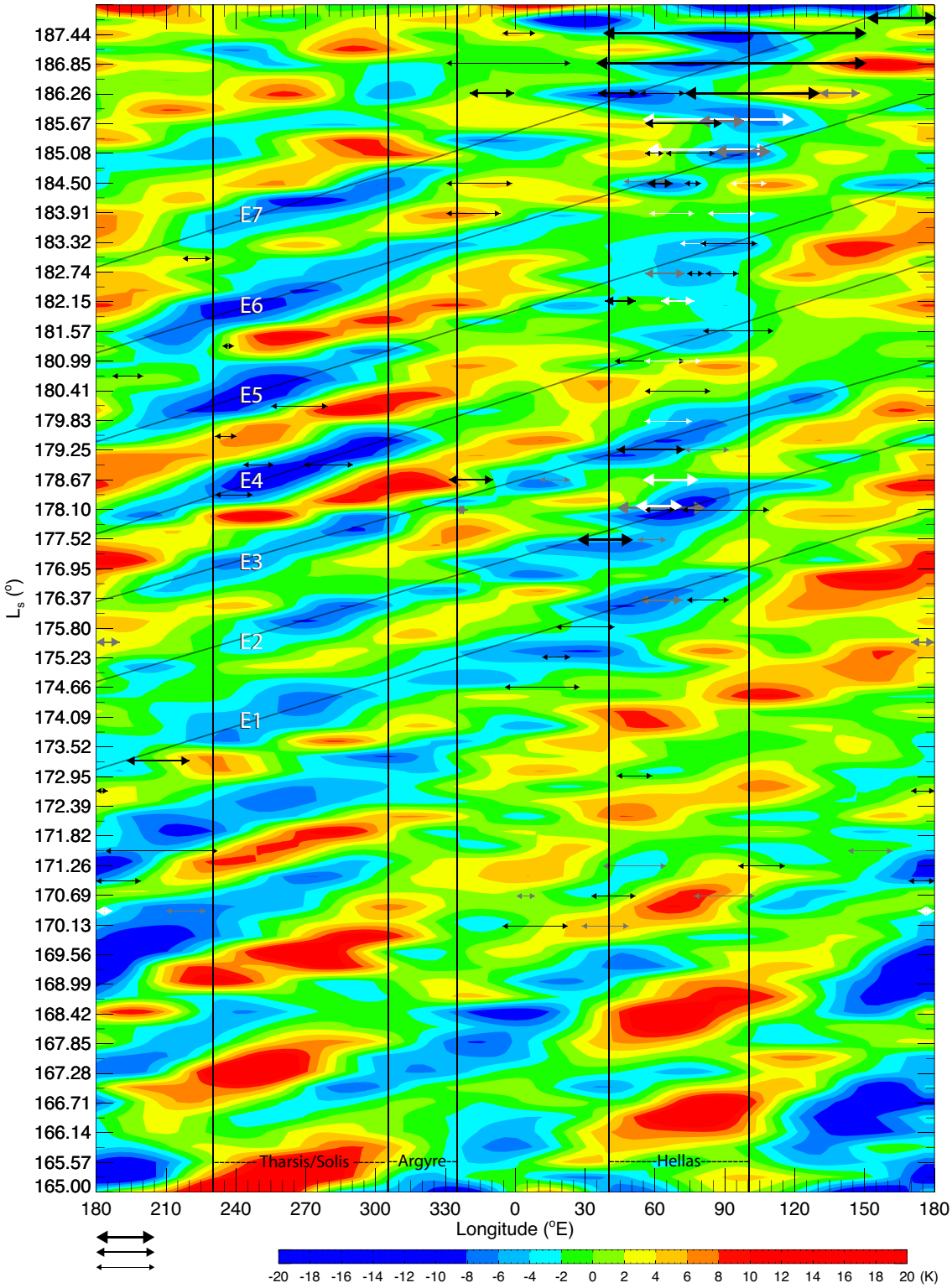
187.44
186.85
186.26
185.67
185.08
184.50
183.91
183.32
182.74
182.15
181.57
180.99
180.41
179.83
179.25
178.67
178.10
177.52
176.95
176.37
175.80
175.23
174.66
174.09
173.52
172.95
172.39
171.82
171.26
170.69
170.13
169.56
168.99
168.42
167.85
167.28
166.71
166.14
165.57
165.00
L_s (°)
E7
E6
E5
E4
E3
E2
E1
Tharsis/Solis
Argyre
Hellas
180
210
240
270
300
330
0
30
60
90
120
150
180
Longitude (°E)
-20 -18 -16 -14 -12 -10 -8 -6 -4 -2 0 2 4 6 8 10 12 14 16 18 20 (K)

Figure 7. Longitude-time plot of TES FFSM eddies (E1–E7) and MOC-observed dust storms, 3.7 hPa, 60° S, MY25, L_s =165.1–187.74°. Arrows delimit the longitudinal extent of dust storms based on our and Cantor's (2007) analyses of MOC images. Three arrow sizes represent a subjective magnitude scale of apparent convective activity/structure, while colors represent storm central latitudes: black (< 45° S), grey (35–45° S), and white (25–35° S). FFSM data have 5° longitudinal resolution, while storm arrows have 1°.

The first storm is located (roughly) near the zero line between cold and warm anomalies (Figs. 6a and 8a).

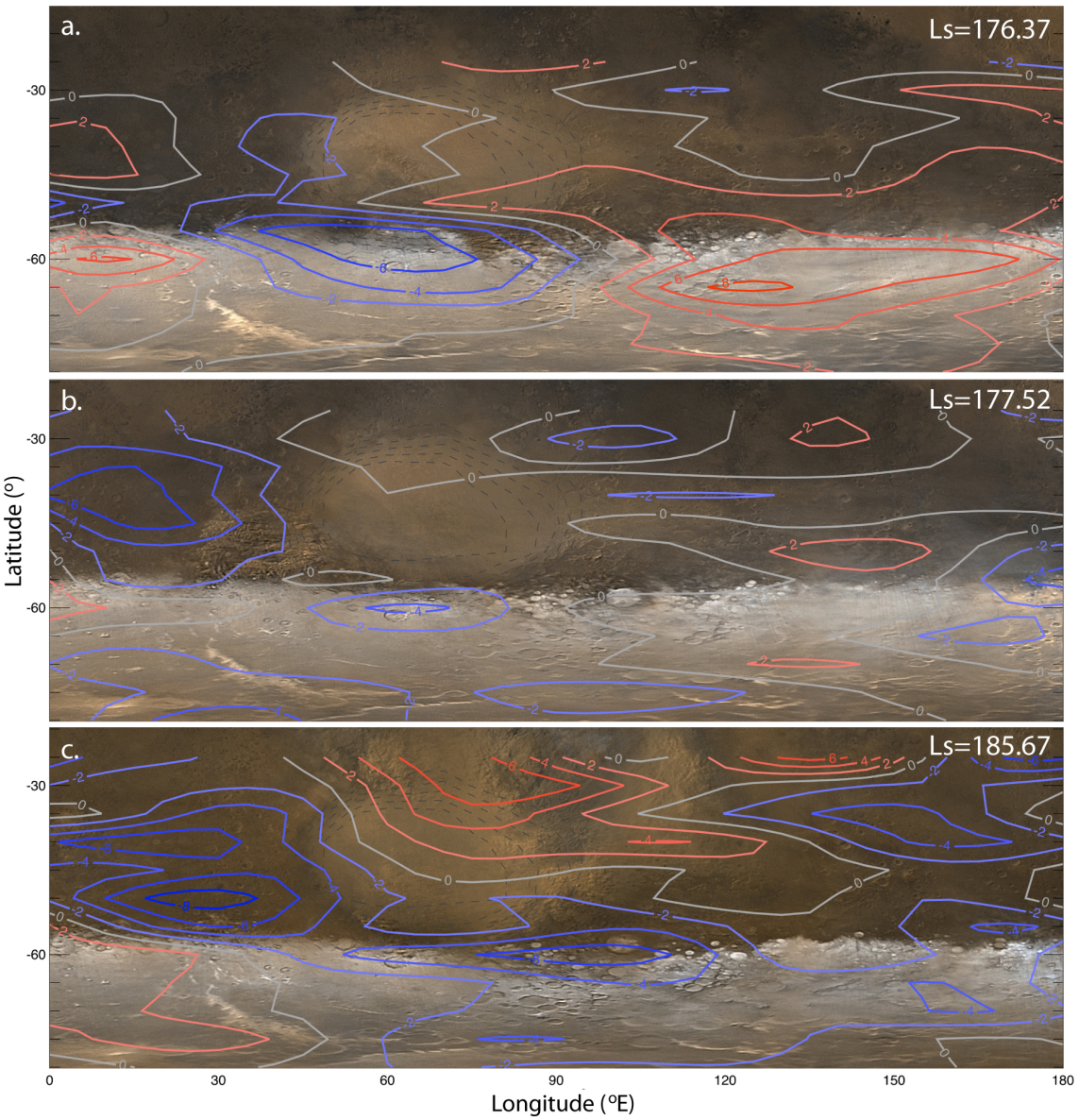

Figure 8. TES FFSM eddies on MOC DGMs, 3.7 hPa, Hellas quadrant

To better understand the role of eddies in the precursor phase, we superimposed FFSM eddy temperature contours on MOC DGMs (N.B. FFSM eddies are synoptic estimates, while MOC DGMs are asynoptic). By L_s=176.7° (sol 2) eddy activity had diminished east of Hellas at ~100° E and the local storms had subsided.

The second eddy (E2) propagated into Hellas on L_s=177.4° (sol 3) (Fig. 7). Two local storms are associated with this eddy, one in western Hellas and a second near the seasonal cap edge southwest of Hellas (50.6°S, 40°E) (Fig. 6b). Both are located on the leading edge of strong cold anomalies (Fig. 8b). These storms joined on L_s=178.0° (sol 4) and grew in intensity as they propagated northward and eastward as shown in Fig. 6c. By L_s=178.5° (sol 5), eddy intensity diminished east of Hellas at 120° E (Fig. 7), while storm activity expanded into northern Hellas. Opacity retrievals of τ_d = 0.7–0.8 were observed from 30°S to 45°S, and a τ_d = 0.2 opacity branch expanded northeast into Tyrrhena and Isidis to ~0° N, 105° E (Fig. 6d).

The third eddy (E3) propagated into Hellas (Fig. 7) on L_s=179.1° (sol 6). The previous sol's storm expanded northeastward into the subtropics, while new local storms appeared in Malea Planum and western Hellas (41.9° S, 51.2° E). Dust clouds extended to 21° S, and τ_d=0.2 contours spread northeastward to ~110° E (Fig. 6e). Equatorward storm expansion extended to 10° S on L_s=179.6° (sol 7) as shown in Fig. 6f. Eddy 3 propagated as far as 130° E before diminishing on L_s=180.1°. Eddies 1–3 are (somewhat) globally coherent, originating near ~ 200° E and propagating through Argyre into Hellas. The TES 2 pm zonal mean temperature field at L_s=180.1° is shown in Fig. 9a. This thermal structure is representative of pre-storm values (*c.f.* Fig. 9b)

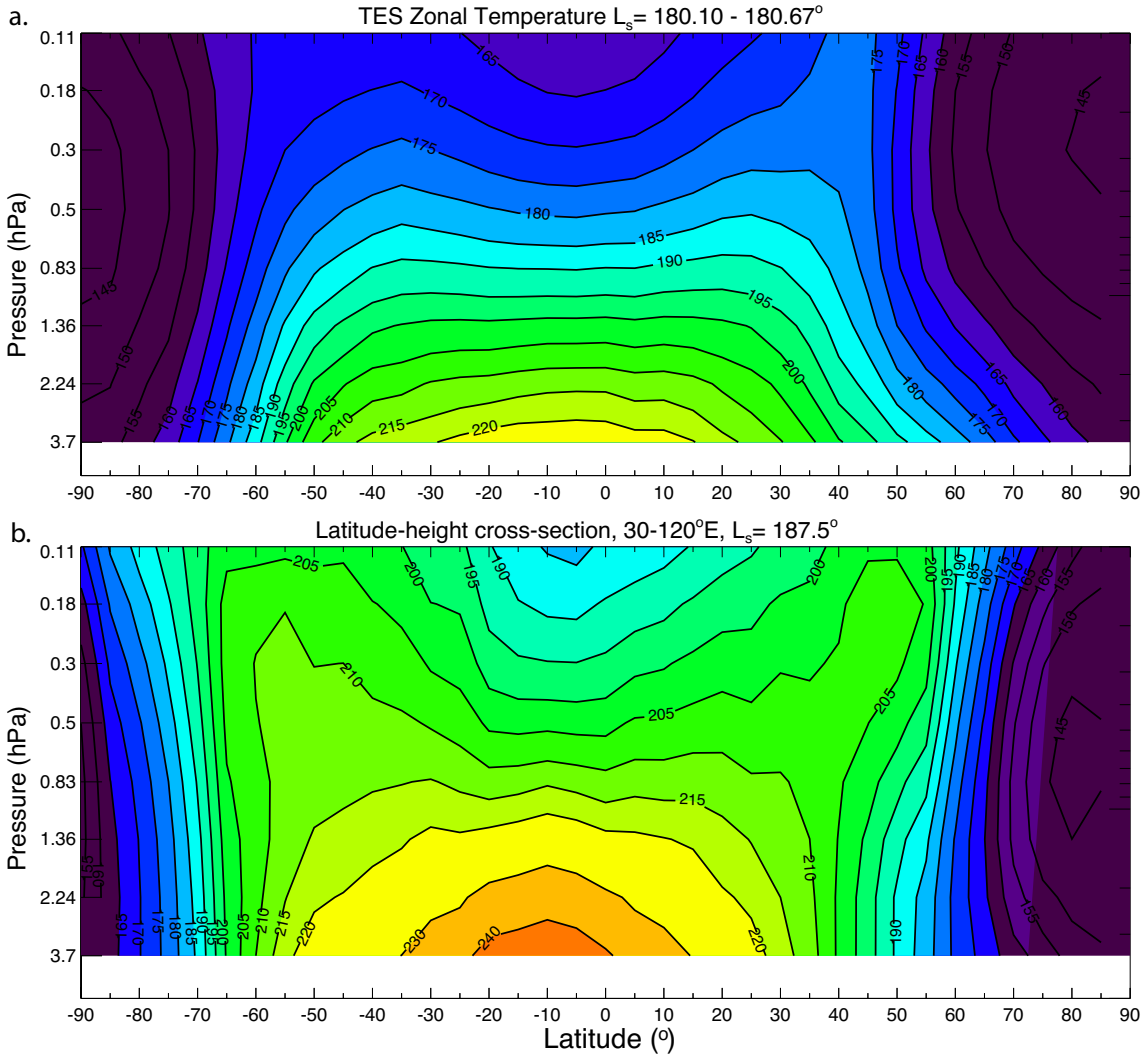

Figure 9. (a) TES 2 pm zonal temperature, L_s=180.1°; (b) TES 2 pm latitude-height cross section, 30-120° E, L_s=187.5°

The fourth eddy (E4) propagated into Hellas on L_s=180.8°, sol 9 (Fig. 7). The previous sol's storms expanded into the southern subtropics to 12° S, while new storm activity developed in central Hellas at 45.6°S, 68.7°E (Fig. 6g). On L_s=181.3° (sol 10) subtropical storms expanded eastward into Tyrrhena while new cap-edge storm activity

appeared southeast of Hellas in Malea (57.2°S, 90.6°E). Eastward dust transport along the equator (hereafter equatorial branch) extended to ~135 °E, as seen in Fig. 6g τ_d = 0.2 contours.

The fifth eddy (E5) propagated into Hellas on L_s=181.9°, sol 11 (Fig. 7). A cap-edge storm appeared southwest of Hellas (54.3°S, 47.4°E). Cantor (2007) inferred from MOC imagery that this storm propagated northeastward towards Tyrrhena over the next two sols. A weak amplitude (5–10 K), quasi-stationary wave one feature with an eastern hemisphere ridge centered at 50–60° E in the north, and western hemisphere trough appeared in the 0.5–0.11 hPa TES nadir (not shown) and MHSA temperature fields (Fig. 10).

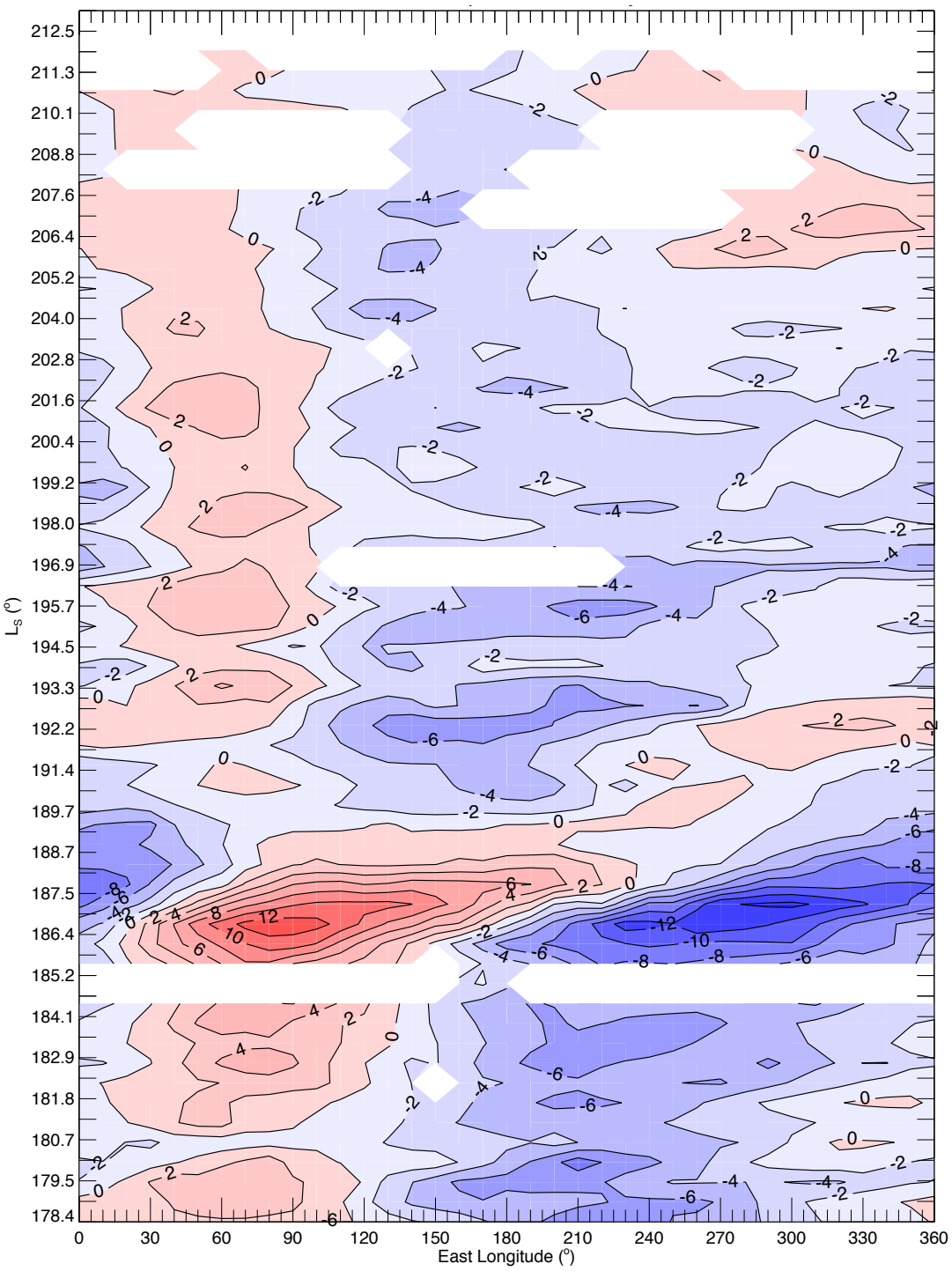

Figure 10. MHSA temperature anomaly (instantaneous observations minus zonal averages) averaged for 55–60° S

Along the equator, τ_d = 0.2 (0.3) levels extended eastward to ~160° E (120 °E), and to ~235° E (140 °E) the following sol, L_s=182.4°. By L_s=183.6°, tropical opacities of τ_d = 0.2 extended to ~265° E (not shown), while τ_d = 0.3 extended to 140 °E (Fig. 6h).

On sol 15, L_s=184.2°, the sixth eddy (E6) propagated into Hellas (Fig. 7). Five local storms developed, two along the cap edge, and the remaining along the southeast, southwest, and northwest rims of Hellas (Fig. 11a) (Cantor 2007).

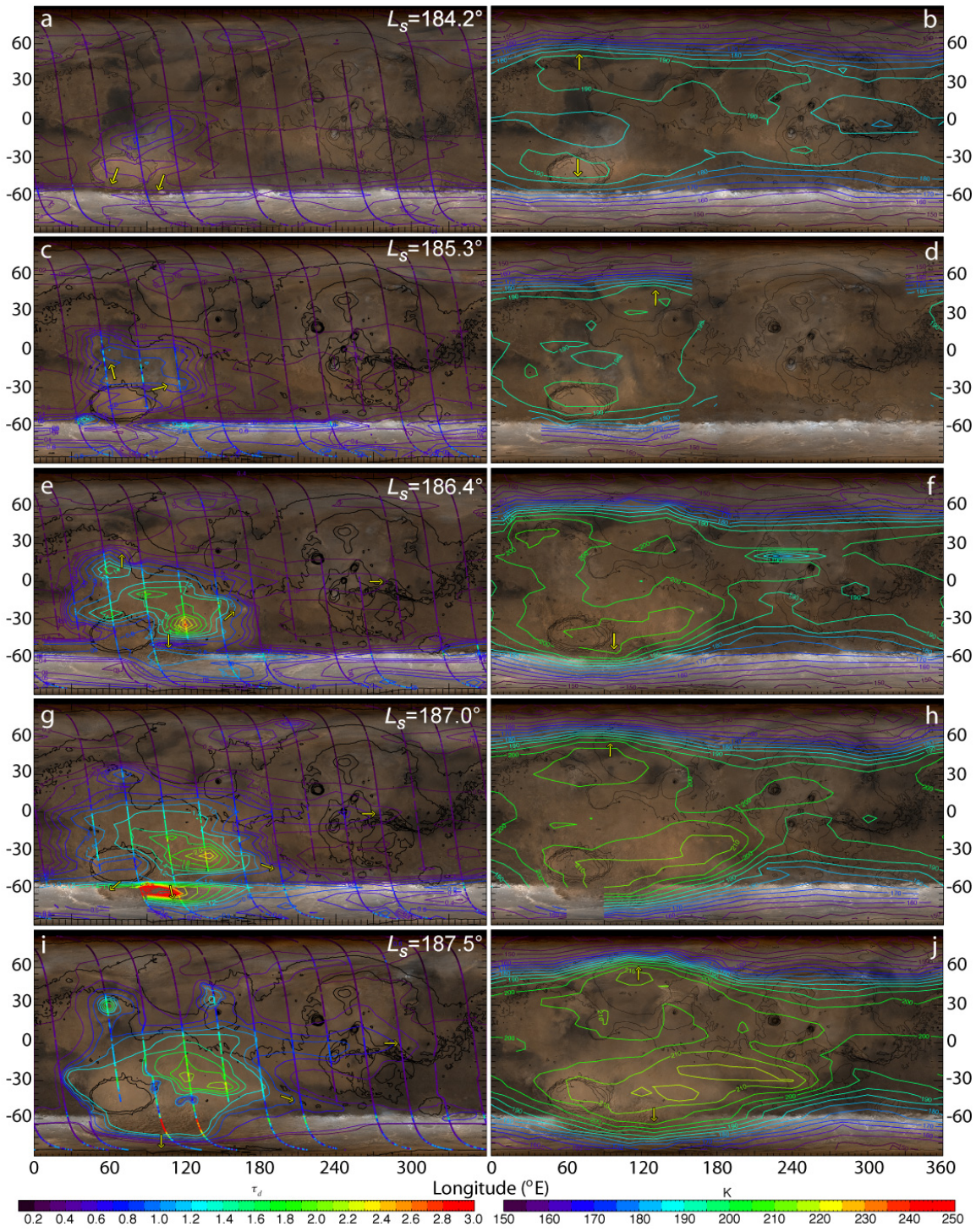
a
L_s=184.2°
b
c
L_s=185.3°
d
e
L_s=186.4°
f
g
L_s=187.0°
h
i
L_s=187.5°
j
60
30
0
-30
-60
0
60
120
180
240
300
360
Longitude (°E)
τ_d
0.2 0.4 0.6 0.8 1.0 1.2 1.4 1.6 1.8 2.0 2.2 2.4 2.6 2.8 3.0
K
150 160 170 180 190 200 210 220 230 240 250

Figure 11. MGCM-derived opacity (a,c,e,g,i), 0.5 hPa temperature (b,d,f,h,j), SDM (i) L_s=184.2-187.5°. Arrows indicate dust storms and transport on opacity plots, and wave on warm peaks on temperature plots.

A 20°-latitude wide τ_d=0.2 (0.3) opacity branch moved eastward along the equator to ~280° E (150° E). Wave one amplification is visible in TES 0.5 hPa (Fig. 11b) and MHSA (Fig. 10) temperature fields. SH temperature contours are fairly zonally symmetric at 3.7 hPa, while significant wave amplification begins at 0.83 hPa and increases through 0.1 hPa (not shown).

4.3 Expansion Phase L_s=184.7–193°

The expansion phase began on L_s=184.7° as storm activity spread northward from Hellas into Tyrrhena, and eastward into Hesperia and Promethia to 110°E (Cantor 2007). On L_s=185.3° storm activity spread further to the north, northeast, and east into Tyrrhena, Hesperia, and Promethia respectively (Fig. 11c), with steep opacity increases measured from 10° N–30° S, and diffuse dust spreading beyond lifting centers (Cantor 2007). Along the equator, τ_d = 0.3 levels extended to ~160° E, and the wave one's NH peak propagated further eastward to ~125° E (Fig. 11d).

On sol 18, L_s=185.9°, the storm spread northeastward over the equator into Isidis and Elysium (10°N, 122°E), eastward into Cimmeria (147.6°E), and southward over the polar cap as far as 66°S (Cantor 2007). Dust cloud heights of 21.5–29.0 km over Isidis

were estimated by Cantor (2007) based on shadow length measurements. Opacity levels of $\tau_d = 0.3$ extended to ~205° E along the equator.

By L_s=186.4° dust storm activity had expanded southward over the polar cap (to 73° S, 96° E), northward to Syrtis Major, and eastward towards Elysium. The equatorial opacity branch ($\tau_d = 0.3$) reached ~290° E (Fig. 11e). The quasi-stationary wave's SH peak amplified and shifted eastward to ~100° E (Fig. 11f). Vertical temperature profiles (Fig. 12) show ~44 K warming from L_s=182.4–186.9° in the 0.5–0.18 hPa layer and strengthened inversions from L_s=186.4°–186.9° in the 3.7–0.3 hPa layer.

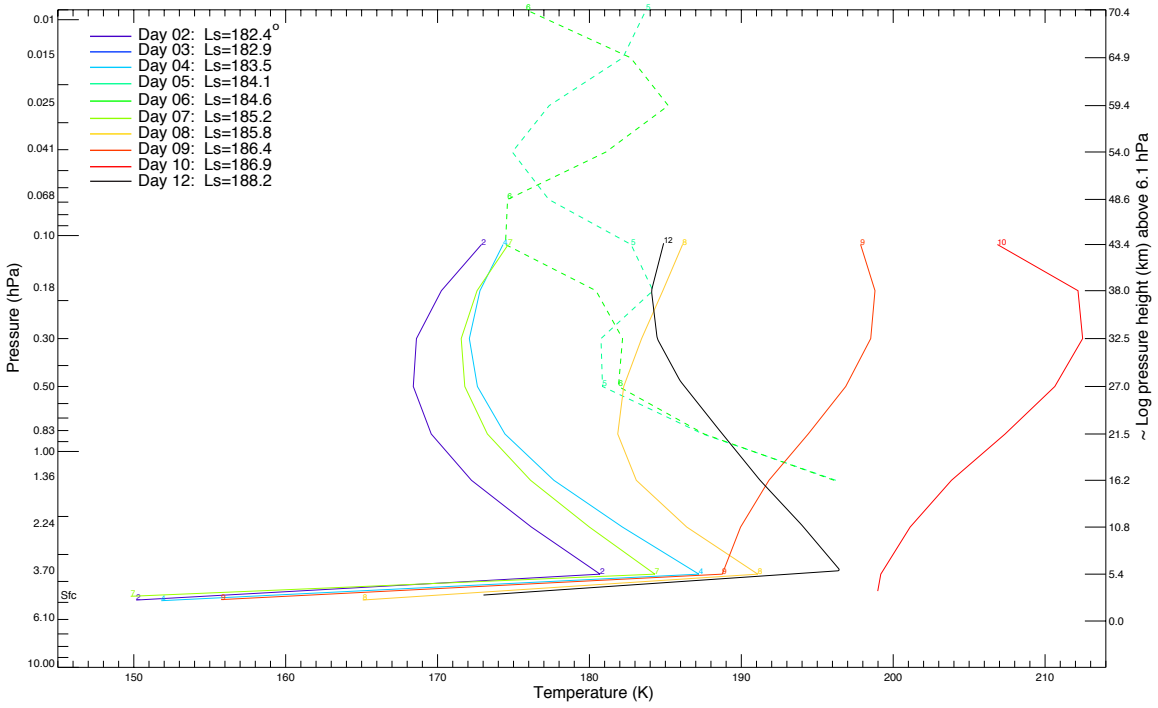

Figure 12. Evolution of TES temperature profiles, 60–85° E, 65° S, L_s=182.4–188.2°; solid: nadir; dashed: limb.

By L_s=187.0°, the continued northeastward storm expansion had caused opacity levels to increase to τ_d =1.2–1.3 across a large area from Hellas in the southwest to Elysium in the northeast. Thick dust clouds with visible signs of convective and advective "lobate" structure obscured the south polar cap from 50–120° E and to 75° S (Cantor 2007). A thinner veil of dust partially obscured the cap from 120–185° E (Fig. 11g). The quasi-stationary wave's NH peak amplified and shifted eastward to ~90° E (Fig. 11h). The equatorial branch moved farther eastward, with τ_d = 0.4 levels measured at ~280° E, and τ_d = 0.6 at 200° E. The expanding dust cloud also arrived in the Tharsis hemisphere at 30–40° S (hereafter extratropical branch), with τ_d = 0.6 levels extending to ~200° E (Fig. 11g). A dipole-like structure with a 235 K warm cell at 250° E, 5° S and a 205 K cold cell at 250° E, 30° S was observed at the 2.24 hPa level (not shown).

By L_s=187.5°, MOC DGMs showed thick clouds of dust extending from 55–140° E and to 80.7° S (Figs. 11i and 13) (Cantor 2007).

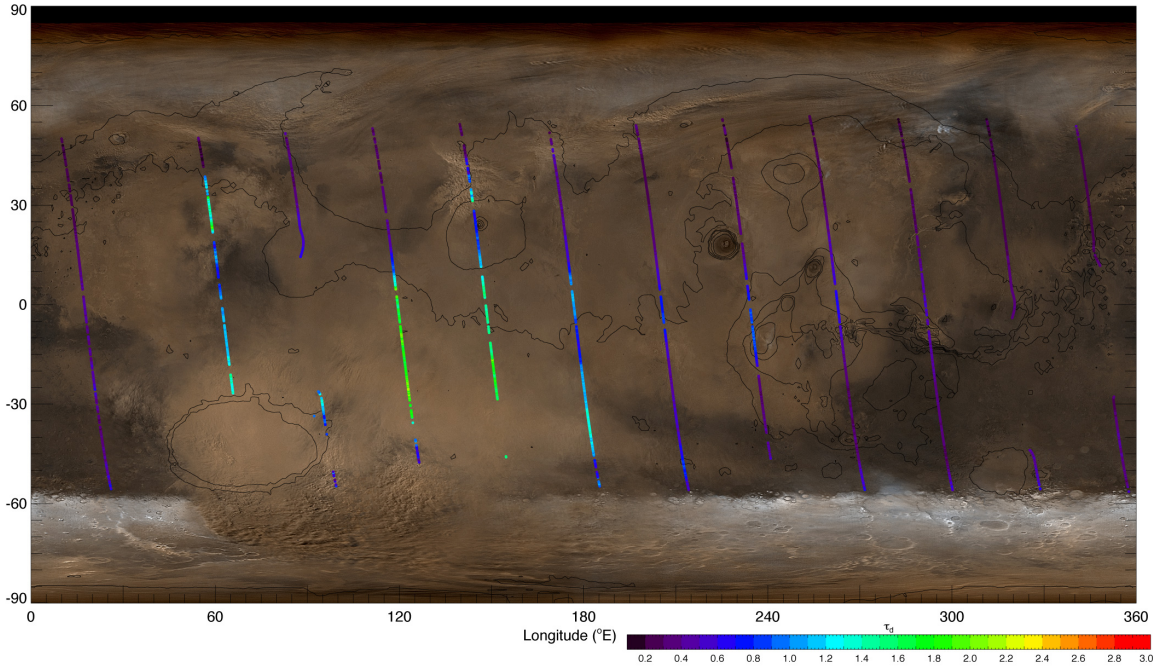

Figure 13**.** TES opacity retrievals on MOC DGM, L_s=187.5°

As dust loading over the southern cap neared its peak, observations indicate that the quasi-stationary wave reached a maximum amplitude of 35–40 K at 0.5 hPa at 60° S. The SH warm peak propagated to ~130° E. Notably symmetrical growth of the wave occurred in the northern hemisphere, with a warm peak centered at ~120° E and a cold trough at ~300° E (Fig. 11j). At 60° N, the wave exhibited deep vertically coherent structure, with 215° K maxima at 0.3 and 0.18 hPa, decreasing to 205 K at 0.11 and 0.5 hPa. Figure 14 shows wave amplification at 60° S. The atmosphere at this time was roughly isothermal at 205 K in two regions: above Hellas (3.7–0.18 hPa) in a broad column centered at ~110° E, 60° S (Figs. 9b and 14), and over Claritas in a narrow column (2.24–0.11 hPa) at 215–240°E, 15–30° S (not shown).

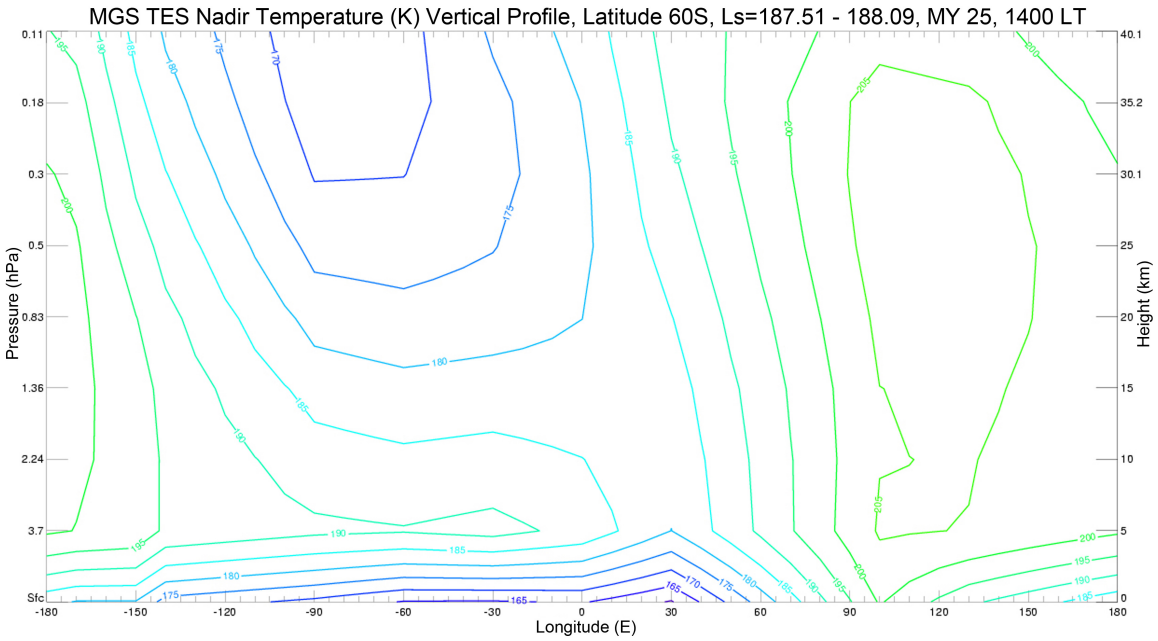

Figure 14. Longitude-height cross-section of TES temperature, 60°S, L_s=187.5°, 2pm.

The equatorial branch on L_s=187.5° had widened to ~10° N–15° S, and τ_d = 0.6 levels extended to ~265° E. Active dust lifting in the extratropical branch extended to 184° E, while haze stretched to ~207° E (Cantor 2007) (Fig. 11i). The dipole-like structure near Arsia Mons narrowed, with a 235 K maximum at 5° S, 235° E, and a minimum at 240° E, 16° S (Fig. 15a). Plots of TES-measured nadir lapse rate (*dT/dz*) between 0.83 and 2.24 hPa southwest of Arsia Mons indicate a transition at ~12° S between positive values (more stable) to the south, and negative values (unstable) to the north. Figure 15b shows lapse rate in the 1.36–2.24 hPa layer with an arrow indicating the transition.

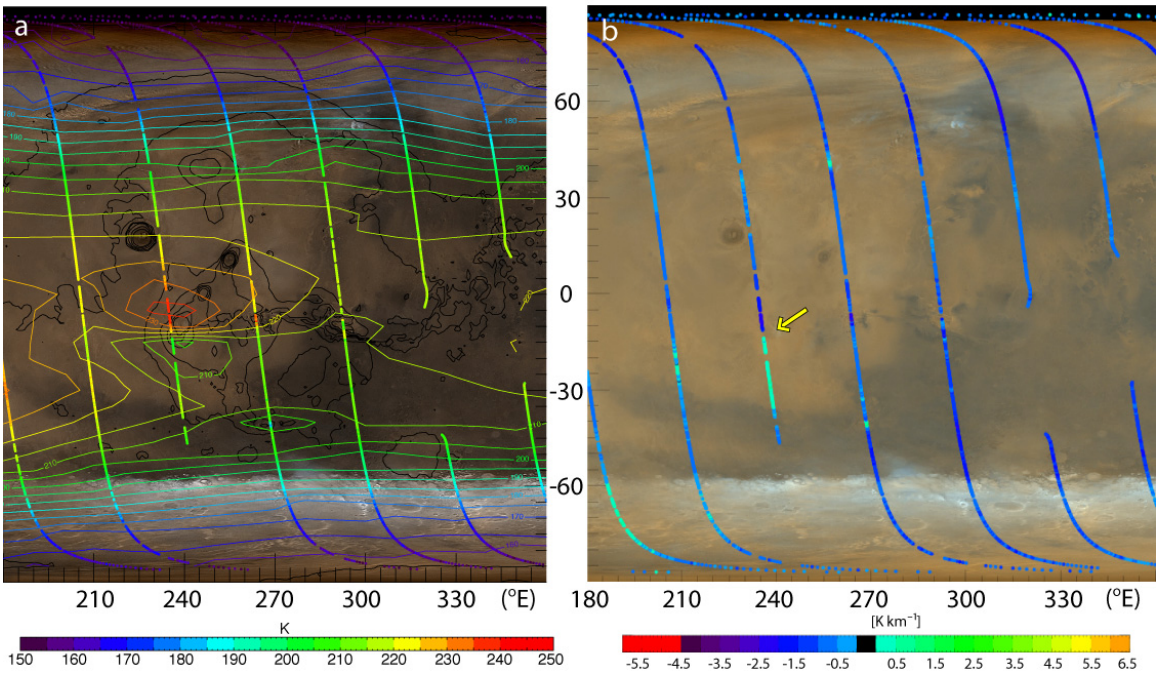

Figure 15. (a) TES 2.24 hPa temperature, L_s=187.5°, 2 pm. (b) TES lapse rate, dT/dz, [K km^{-1}] between 1.36 and 2.24 hPa. Arrow points to region of interest near Claritas.

Figure 16 is a longitude-height plot of static stability on L_s=181.8 (Fig. 16a) and 187.5° (Fig. 16b), the sol before lifting was initiated in Claritas.

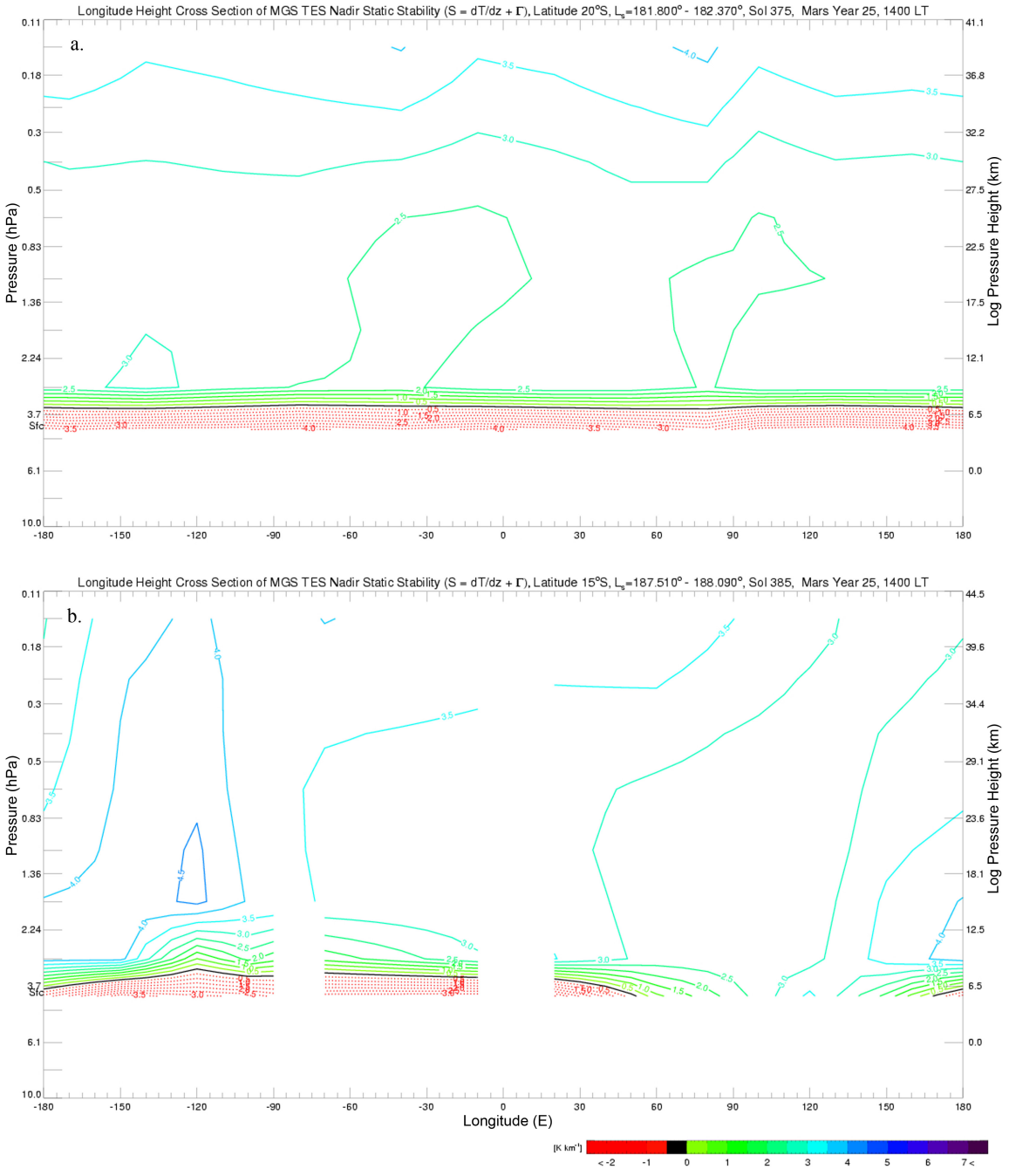

Figure 16. Longitude height sections of static stability ($S = dT/dz + \Gamma$), (a) L_s=181.8° (20°S); (b) L_s=187.5° (15°S). *N.B.* The 20° S plot (a) was chosen due to missing data at 15° S.

On L_s=181.8, conditions are generally unstable from the surface to 3.7 hPa, and increasingly stable with height above 3.7 hPa. Although the unstable lowest layer of the atmosphere has deepened slightly at 240° E (shown as –120° E in Fig. 16), it is unclear if this is a significant signal or an artifact of topography (due to Arsia Mons), binning, and/or TES resolution limitations. Even if it is real, there is no compelling evidence from this figure or from the following sol (not shown) that instability is a critical trigger in the initiation of dust lifting. Stability in the column above 240° E increased after L_s=181.8°, probably due to mid-level equatorial dust haze, although clearly not sufficiently to suppress dust lifting and expansion over the following sols.

On L_s=188.2°, dust loading over the cap had increased to the point where features were completely obscured as far east as ~165° E, while thinner haze was observed over the cap as far east as 250° E (Fig. 17a).

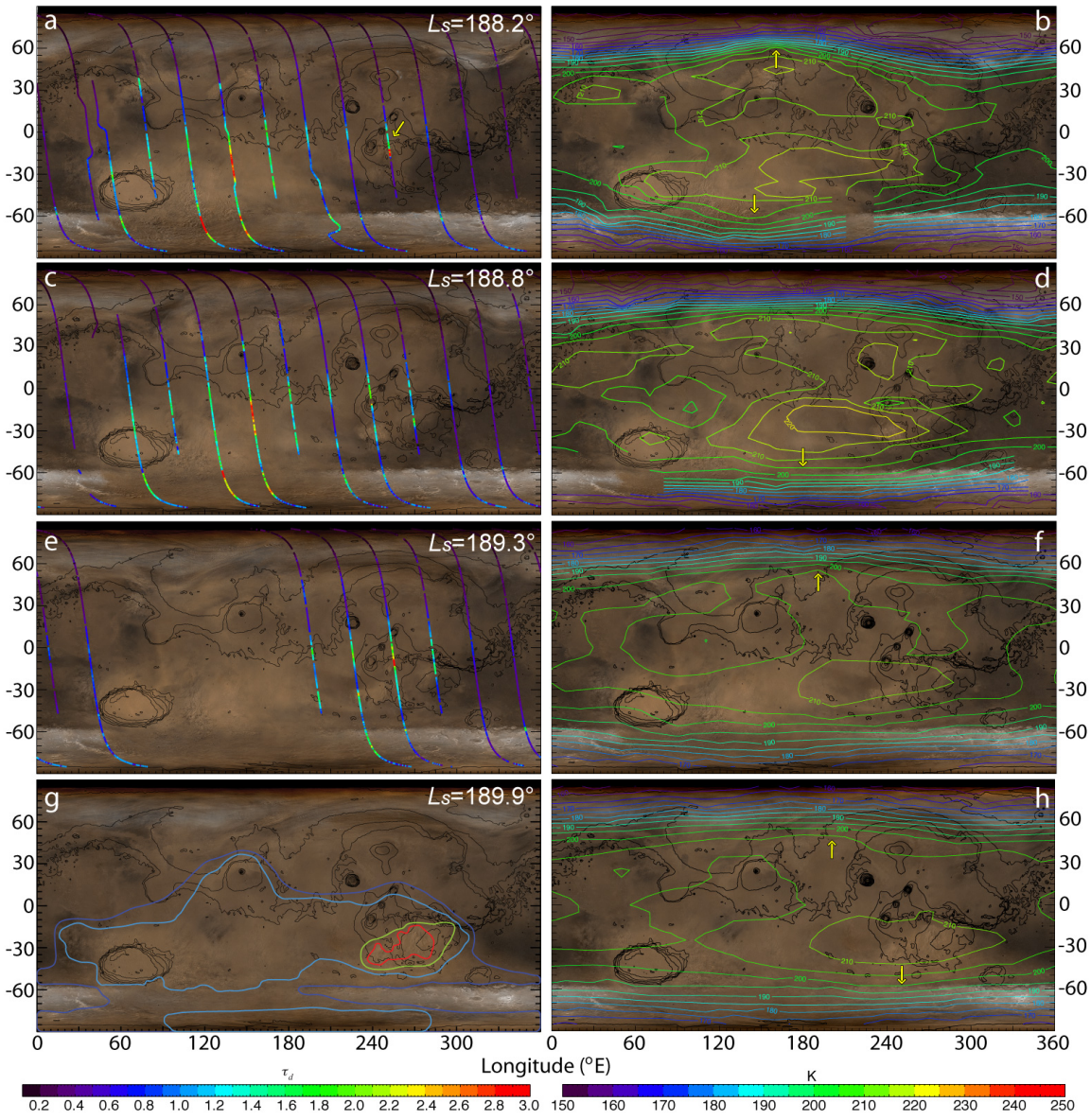

Figure 17. Dust optical depth and mid-level 2 pm temperature, L_s=188.2–189.9° MGCM-derived opacity (a, c, e), TES 0.5 hPa *T* (b, d), MHSA Q2 *T* (f, h), SDM (g)

The eastern extent of the wave one's warm peaks relocated, with the SH warm peak located at ~140° E, while the NH warm peak was located at ~160° E (Fig. 17b). Dust

lifting was initiated in Claritas Fossae at 12.5° S, 249° E (Cantor 2007). MOC imagery shows highly structured dust clouds extending from Arsia Mons to Claritas Fossae. TES observations show a detached dust opacity region (Smith *et al.* 2001; Strausberg *et al.* 2005) with τ_d>3.15 maxima in the Claritas highlands (13° S, 252° E) (Fig. 17a), along with a 255 K surface temperature minimum, and a temperature maximum of 250 K at 2.24 hPa.

By the following sol, L_s=188.8°, local storm activity in Tharsis had spread eastward and southward. Although dust still obscured the cap from 50–190° E, it appeared more homogenous and less textured than on the previous sol (Fig. 17c). The wave one's amplitude decreased and the SH warm peak progressed to ~180° E. (Fig. 17d).

4.3.1 WAVE ONE MAXIMUM AMPLITUDE TEMPERATURE PEAKS

Atmospheric temperatures rose steadily throughout much of the Hellas and Utopia quadrants from L_s=180.7–187.5° (Cantor 2007; Smith *et al.* 2002; Strausberg *et al.* 2005), and dropped sharply the following sol at L_s=188.2°. A SH temperature peak was observed in a wide area from 90–160° E at 85 S, and from 40–95° E at 50° S. Figure 18c shows temperature and opacity evolution over central Hellas, while Fig. 18d shows the most pronounced peak at 80° S, 90º–115° E, where ~29 K upper level (0.3 to 0.11 hPa) warming was measured from L_s=186.9–187.5°, followed by ~28 K cooling the following sol from L_s=187.5–188.7°.

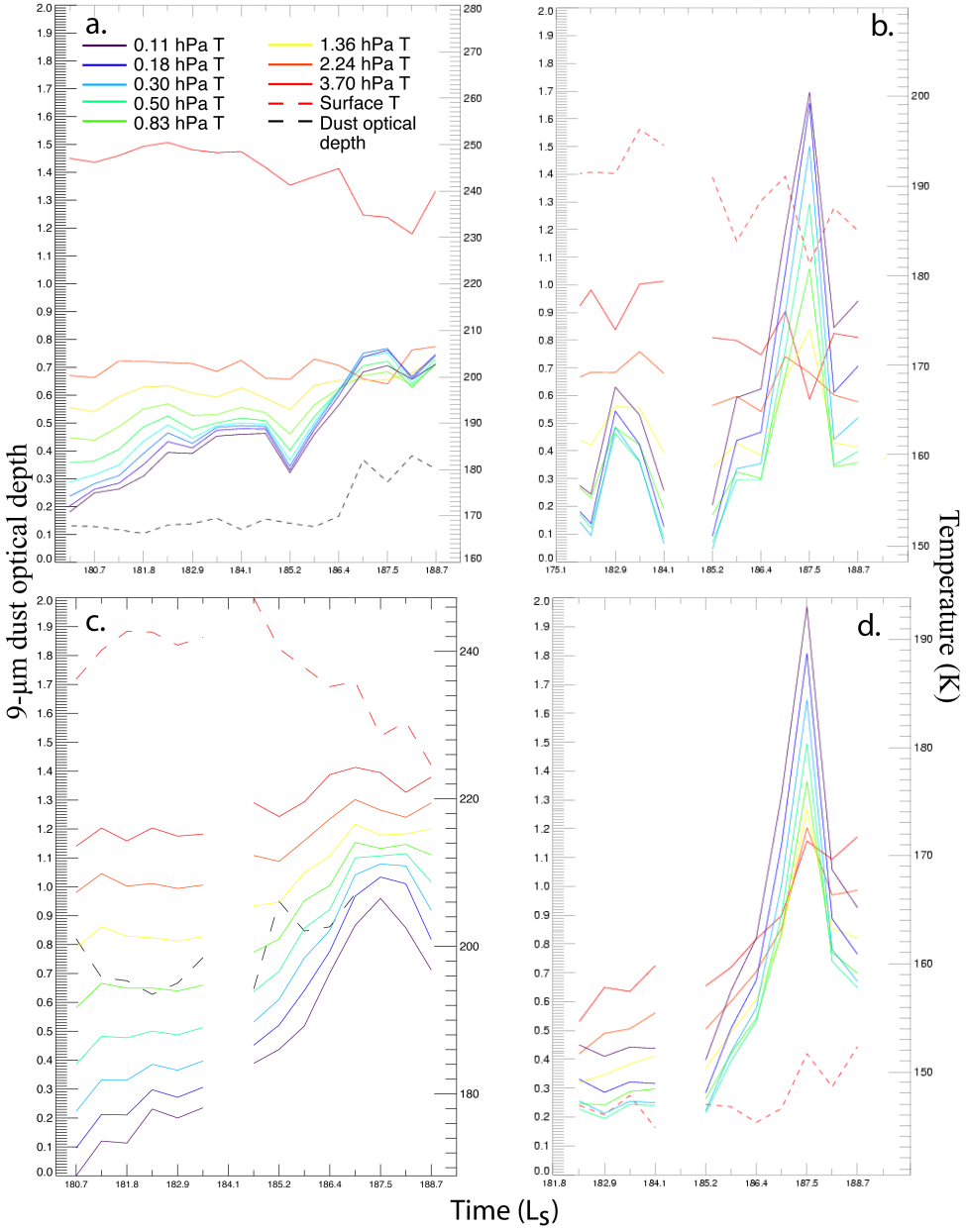

Figure 18. Time histories of TES opacity and temperature L_s=180–188.7°, (a) 60–90° E, 60–30° N, (b) 85–110° E, 70–65° N, (c) 60–85° E, 40–45° S, (d) 90–115° E, 80–85° S.

NH warming occurred almost simultaneously with that in the south, and occurred well before opacity notably increased in the north on L_s=187.0° (Fig. 18a). A similar peak

was seen in northern hemisphere 0.5–0.11 hPa temperatures, with a maximum 32/26 K rise/fall occurring between 85–110° E, 70–65° N L_s=186.4–187.5° (Fig. 18b). Upper level warming in the 30–120° E longitude sector is shown in Fig. 9b (*cf.* Fig. 9a). An isothermal column of ~205 K is visible from 60–65° S, (south of Hellas).

Although dust still obscured the cap from 50–190° E on L_s=188.2°, craters southwest and southeast of Hellas became visible, along with patches of the cap at ~70° S. At L_s=188.7°, dust appeared more homogenous and less textured than the previous sol, with further clearing on the cap edge south of Hellas at 60° E. On L_s=189.7° craters south of the cap edge were visible from 40–120° E. By L_s=189.3°, patches of the cap south of Hellas were visible through the dust cloud, while the region from 110–180° E was still obscured (Fig. 17e). Figure 17f shows the wave one structure in the MHSA quadrant 2 temperature field with a NH warm peak at ~ 190° E. We show MHSA temperature data since TES data is missing on this sol.

4.3.2 DAEDALIA-SOLIS REGIONAL STORMS

By L_s=189.9° the Claritas storm expanded to regional scale with apparent convective activity spreading from Valles Marineris in the north to Aonia in the south. Figure 17g shows a preliminary SDM for L_s=189.9°. No TES temperature or opacity data are available for this or the following sol. Figure 17h shows that the eastern extent of the wave one's warm peaks in the MHSA field had relocated, with the SH warm peak located at 250° E, and the NH warm peak located at 200° E. Continued dissipation of the dust cloud over the southern cap was associated with the wave one progressing further

eastward and weakening from L_s=189.9–190.5°. The entire southern cap was visible, although a thin veil remained from 30–330° E, and new storm development in Aonia expanded just over the cap edge from 260–280° E. By L_s=190°, dust had nearly encircled the planet, while active lifting in Hellas appeared to abate (Cantor 2007; Strausberg *et al.* 2005).

Daedalia and Solis Plana regional storms expanded and intensified on L_s=191.7°, while dust haze encircled the SH (Figs. 19a and 19b).

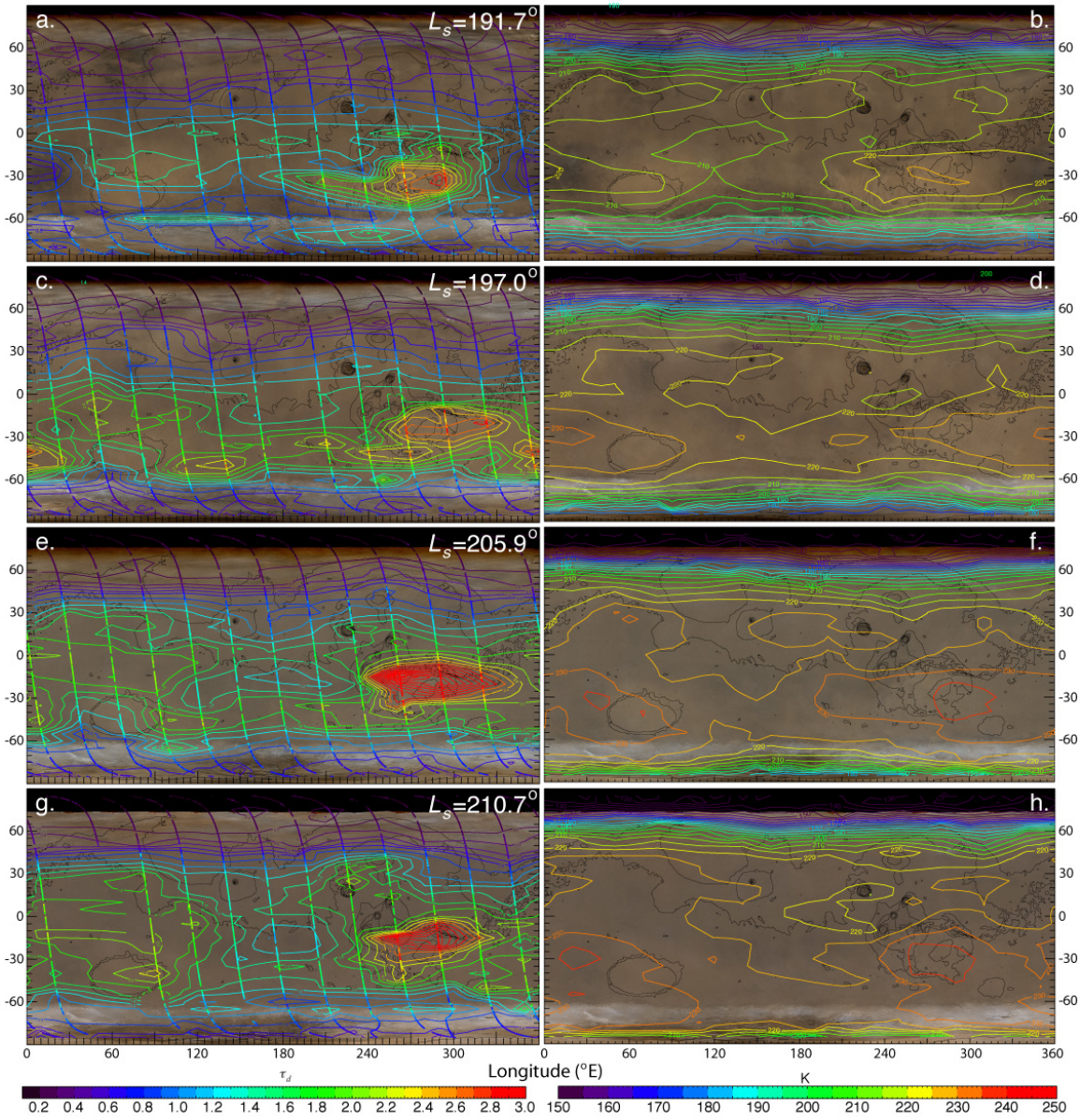

Figure 19. MGCM-derived dust optical depth (a, c, e, g) and TES 0.5 hPa 2 pm temperature (b, d, f, h), L_s=191.7–210.7°

Storm activity grew to planet-encircling scale on the following sol, L_s=192.3°, with Solis Planum storms expanding into Noachis (Cantor 2007). MOC measured SH haze to heights of 60 km (Cantor 2007), while TES observed $\tau_d > 2.0$ levels throughout Solis Planum, and a $\tau_d = 1.2$ opacity belt that encompassed most of the SH.

4.4 Mature Phase L_s=193–210°

Opacity continued to steeply increase across the planet (excluding high latitudes) during the first half of the mature phase, L_s=193–201° (Fig. 5). The SH (> 60° S) was almost completely obscured by L_s=197° (Cantor 2007). TES observed $\tau_d = 2.0$ levels from Cimmeria in the west to Noachis in the east, and a $\tau_d = 1.4$ opacity belt that encompassed most of the SH (Fig. 19c). While temperatures at 0.5 hPa became more zonally uniform, a weak-amplitude wave-one feature with warm peaks in the Hellas hemisphere was still apparent (Fig. 19d).

MOC imagery shows structured dust clouds stretching from Sirenum and Daedalia in the west to Argyre in the east from L_s=193–196°, and in Solis Planum for the remainder of the mature phase. On L_s=205.9°, high opacity levels ($\tau_d = 2.2–4.0$) were observed from Claritas to the prime meridian, while $\tau_d = 1.4$ levels persisted throughout the SH (Fig. 19e). Temperatures at 0.5 hPa were nearly zonally uniform, and the large north-south temperature gradient in the SH became confined to latitudes polewards of 75° S (Fig. 19f). Partial clearing along the cap edge in Promethei, western Sirenum, and eastern Argyre occurred periodically from L_s=196–210.7°. Although storm activity continued in Solis Planum on L_s=210.7°, it showed signs of decline from the previous

sols (Fig. 19g). Dust lifting in Daedalia and Solis Plana appears to have terminated between L_s=210–214°, and PDS decay set in.

We have described the first three phases of the MY 25 PDS: initiation of local dust storms in Hellas, expansion of dust storm activity and dust transport to the northeast, east, and south of Hellas, and initiation of a second dust lifting center in Claritas. By L_s=190°, atmospheric dust fully encircled the planet. Dust storm activity in the Claritas region became the major source of atmospheric dust for the remainder of the storm. Between L_s=210–212°, global opacity reached its maximum level of τ_d = 1.46 (Fig. 5). Discussion of the relationship between global opacity and temperature is located in Ch. 7.3

5 Interannual Comparison of FFSM Eddies

5.1 Interannual Eddy Similarities

In this section we compare and contrast eddies observed in FFSM-filtered TES temperature data during MY 24–26. SH eddy temperature amplitudes are greatest at ~60° S, and diminish significantly south of 65° S and north of 40° S. The maximum at 60° S is expected due to the steep meridional temperature gradient near the receding polar cap (Hinson and Wilson 2002). Eddy structure at 60° S changes with height. For example, strong cold anomalies are predominant in the 3.7–1.36 hPa layer above Hellas (at 60° S) from L_s =174–184°. At 0.5 hPa, warm anomalies are found, and at 0.1 hPa, strong warm anomalies dominate the field (Fig. 20). This change in eddy structure with height indicates that these are not barotropic eddies, and suggests that they are eastward propagating baroclinic eddies.

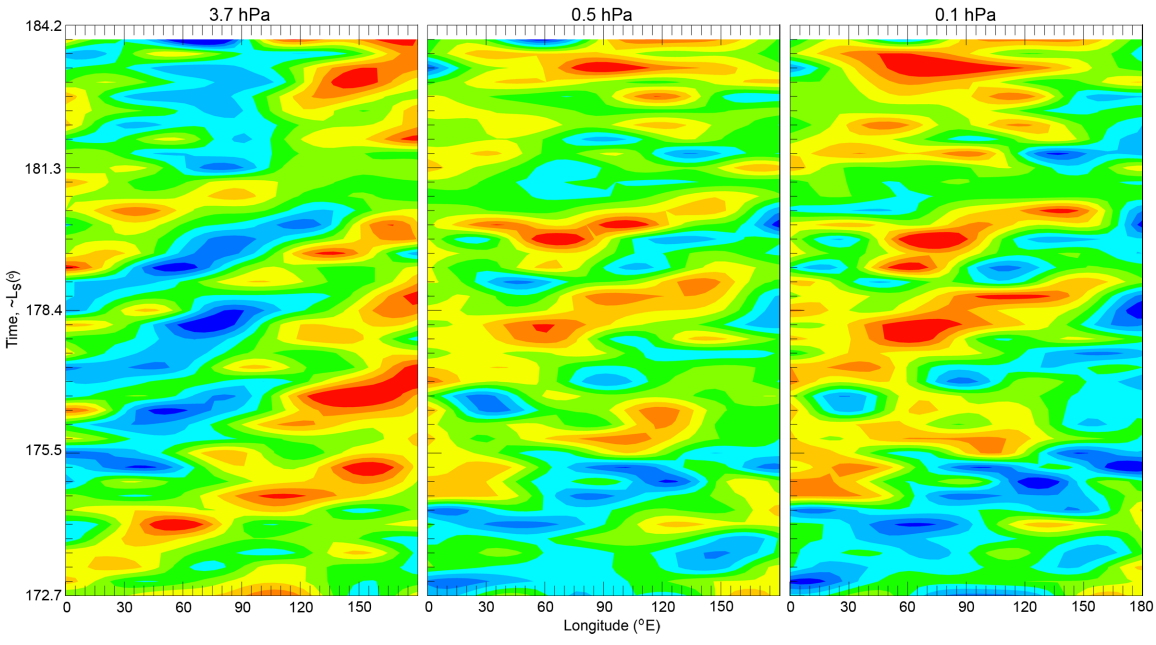

Figure 20. Longitude-time plots of TES FFSM eddies, 60° S, 0-180° E, MY 25 at: (a) 3.7 hPa, (b) 0.5 hPa, and (c) 0.1 hPa

Globally coherent eddies maintain amplitude throughout all or most longitudes. While coherency in the full eddy field (all wavenumbers) appears to be disrupted by SH orography, particularly Argyre and Hellas, wavenumber 3 eddies do not show such disruption (Wilson 2012).

5.2 MY 24 Eddies

Figure 21 shows predominantly wavenumber 2 modes until L_s=175°, followed by a blend of wavenumbers 2 and 3.

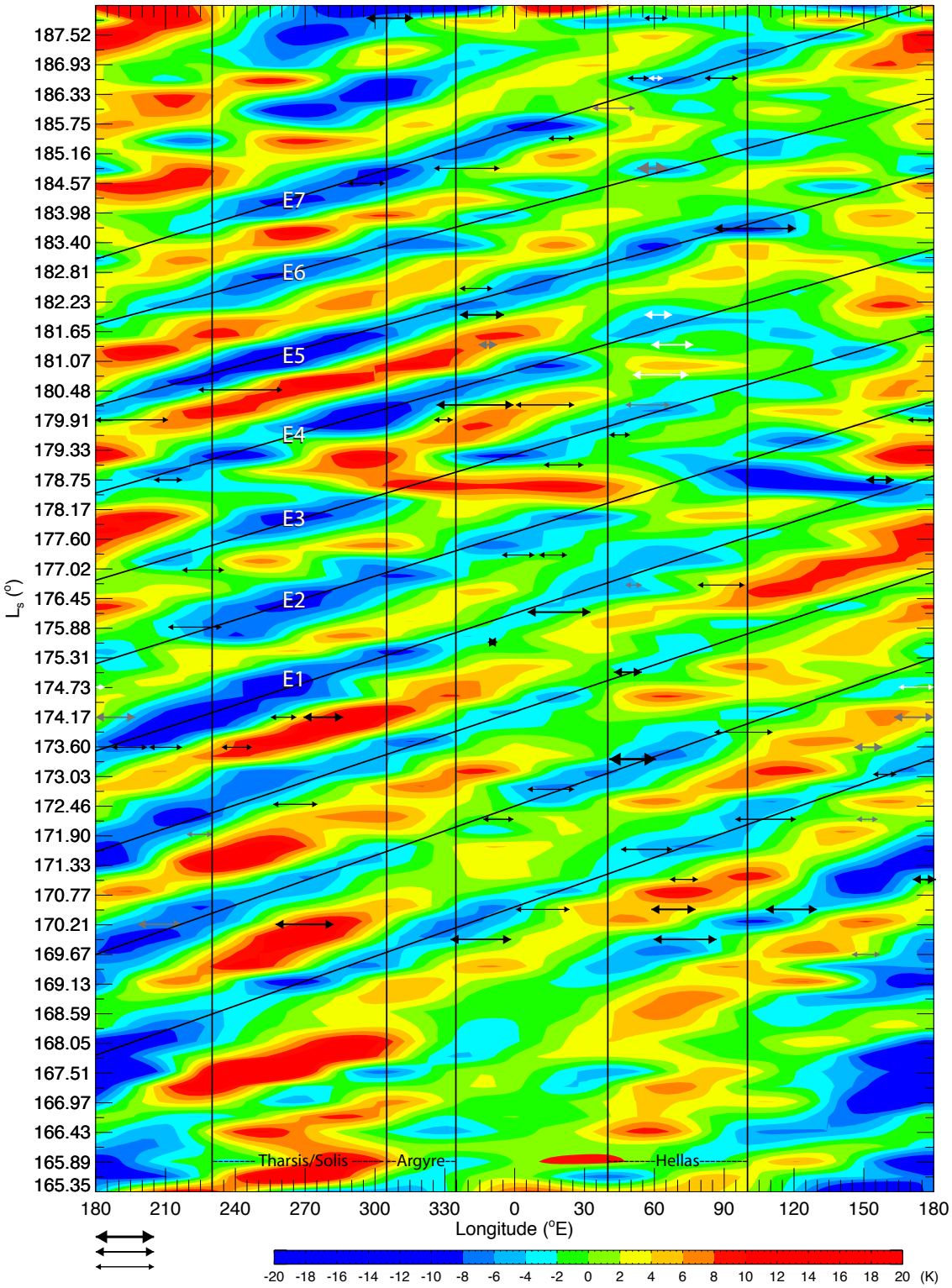
187.52
186.93
186.33
185.75
185.16
184.57
183.98
183.40
182.81
182.23
181.65
181.07
180.48
179.91
179.33
178.75
178.17
177.60
177.02
176.45
175.88
175.31
174.73
174.17
173.60
173.03
172.46
171.90
171.33
170.77
170.21
169.67
169.13
168.59
168.05
167.51
166.97
166.43
165.89
165.35
L_s (°)
E7
E6
E5
E4
E3
E2
E1
Tharsis/Solis
Argyre
Hellas
180
210
240
270
300
330
0
30
60
90
120
150
180
Longitude (°E)
-20 -18 -16 -14 -12 -10 -8 -6 -4 -2 0 2 4 6 8 10 12 14 16 18 20 (K)

Figure 21. TES FFSM eddies and MOC storms, 3.7 hPa, 60° S, as in Fig. 7, except MY24, L_s=165.35-187.83°.

Coherent, strong-amplitude cold anomalies are present in the 150–330° E storm zone for the entire time domain of L_s=165.35–187.83°. Eddy activity within the storm zone appears to shift eastward in time, with strongest eddies appearing in the ~130–240° E sector from L_s=165–173°, and in the ~230–330° E sector from L_s=175–187°. Their apparent weakening from 330–120° E suggests orographic disruption from Argyre and Hellas, as simulated by Hollingsworth (2005). Few strong-amplitude eddies (cold anomalies) maintain amplitude and coherency east of 30° E. The most notable persists until 120° E at L_s=183.7°.

Major cap-edge storms south of Hellas occur less frequently in MY 24 compared to MY 25 when MOC imagery is examined. The most prominent are described below and shown in Fig. 21. At L_s=169.9° large cap-edge storms occurred east of Argyre at 345° E and within Hellas at 80° E. Six sols later at L_s=173.3° a large storm emerged west of Hellas, followed by a smaller one in SW Hellas three sols later at L_s=175.1°. At L_s=180.2° a large cap-edge storm developed between Argyre and Hellas (~330–25° E), along with a storm in NW Hellas. The latter storm appeared to stay confined to northern Hellas and grew for the next three to four sols, visibly diminishing by L_s=182°. Three sols later at L_s=183.5°, dust clouds with a rippled appearance were visible along the cap

edge SE of Hellas. Figure 22 shows that eddies weaken and diminish after L_s=200°. A quasi-stationary mode persists from ~ L_s=200-220°.

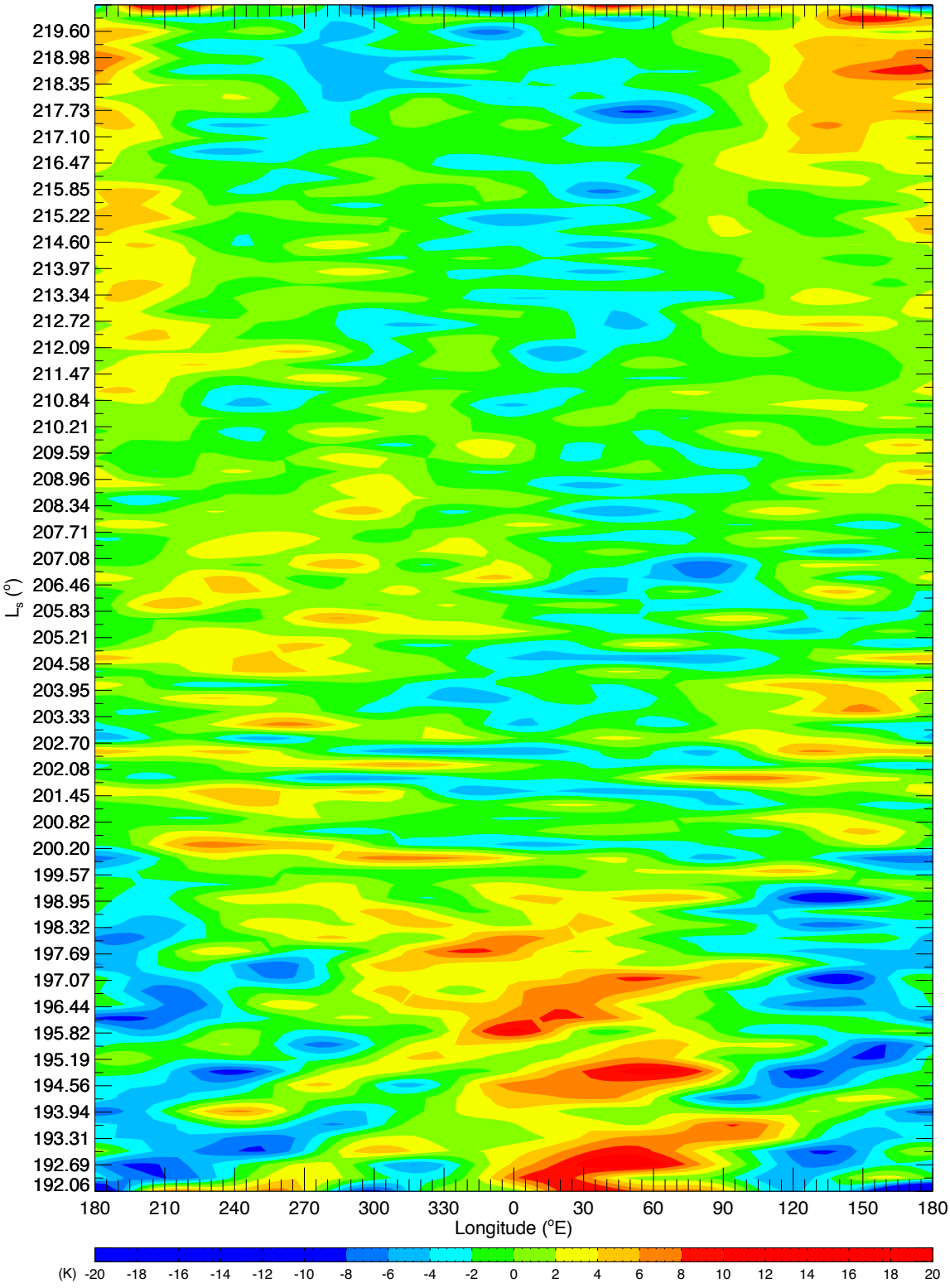

Figure 22. TES FFSM eddies, 3.7 hPa, 60° S, MY24, L_s=192.06–219.83°

5.3 MY 25 Eddies

Coherent, strong-amplitude cold anomalies are present in the 150–330° E storm zone for most of the time domain, and their centers appear to shift slightly eastward over time (Fig. 7). Eddies 1–6 have a period of ~3 sols at 240° E. This general pattern is similar to MY 24. An outstanding difference between the two years is the degree to which strong-amplitude eddies persist through Noachis and extend (undiminished) into Hellas in MY 25. This occurs throughout the precursor phase from L_s=174–180°. The cold anomaly passing through Hellas between L_s=176–179° appears to be the largest amplitude and most coherent eddy during the precursor phase. The corresponding cap-edge storm at L_s=177.5° appears to have the most intense convective activity of this phase (Fig. 8b).

Figure 23 shows MY25 FFSM eddies at 60° S from L_s=191–224°.

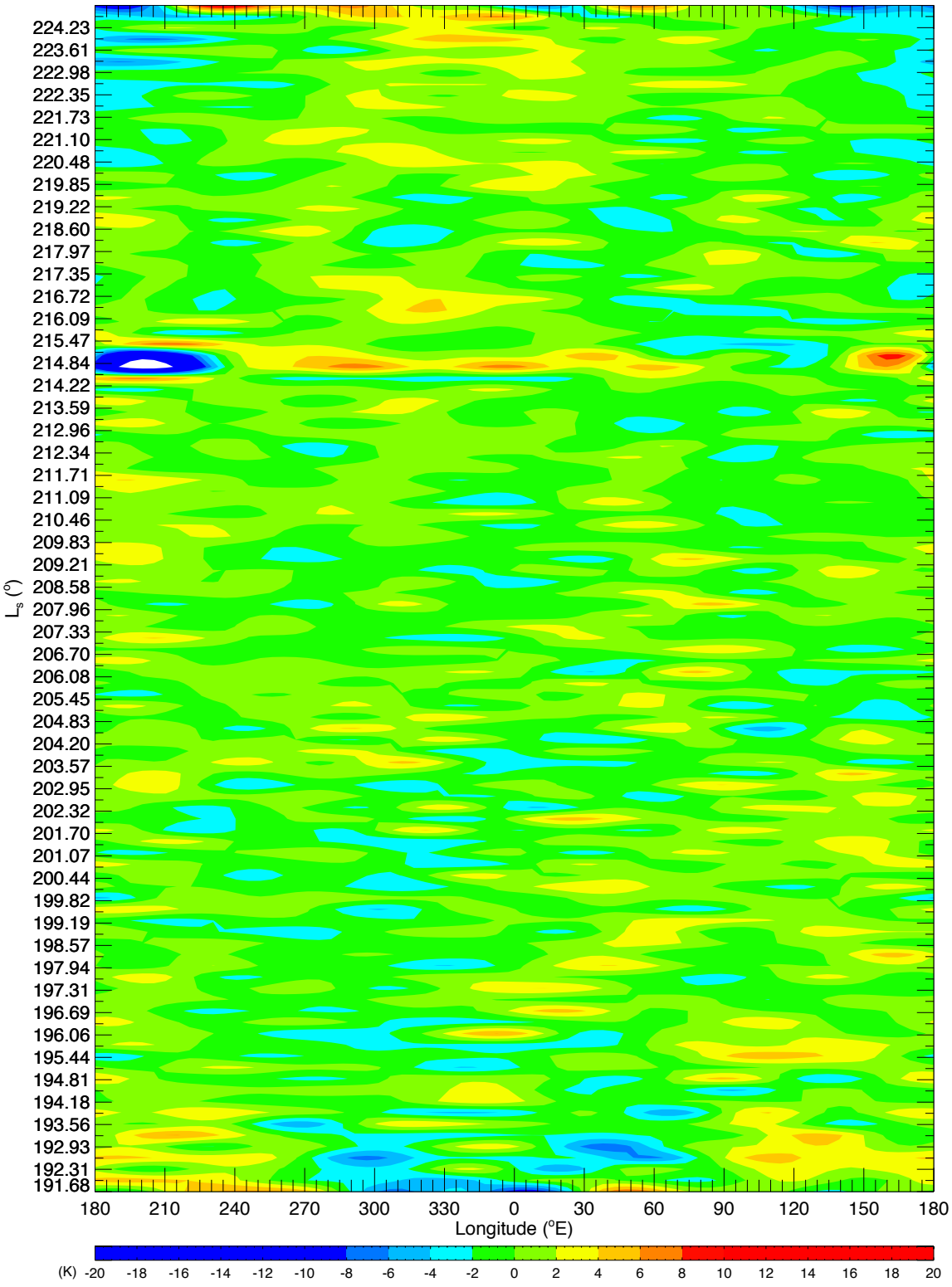

Figure 23. TES FFSM eddies, 3.7 hPa, 60° S, MY25, L_s =191.68–224.58°

The global expansion of the PDS during this time causes transient eddies to diminish more rapidly and disappear after L_s=191° (compared to MY 24). The MY 25 regime from L_s=200–224° is characterized by weaker amplitude anomalies compared to those in MY 24 (Fig. 22) and 26 (not shown).

5.4 MY 26 Eddies

Figure 24 shows MY 26 eddies for L_s=175.39–192.78°. This time range was chosen due to missing data from L_s=165–175°. There is also missing data from L_s=180–181°.

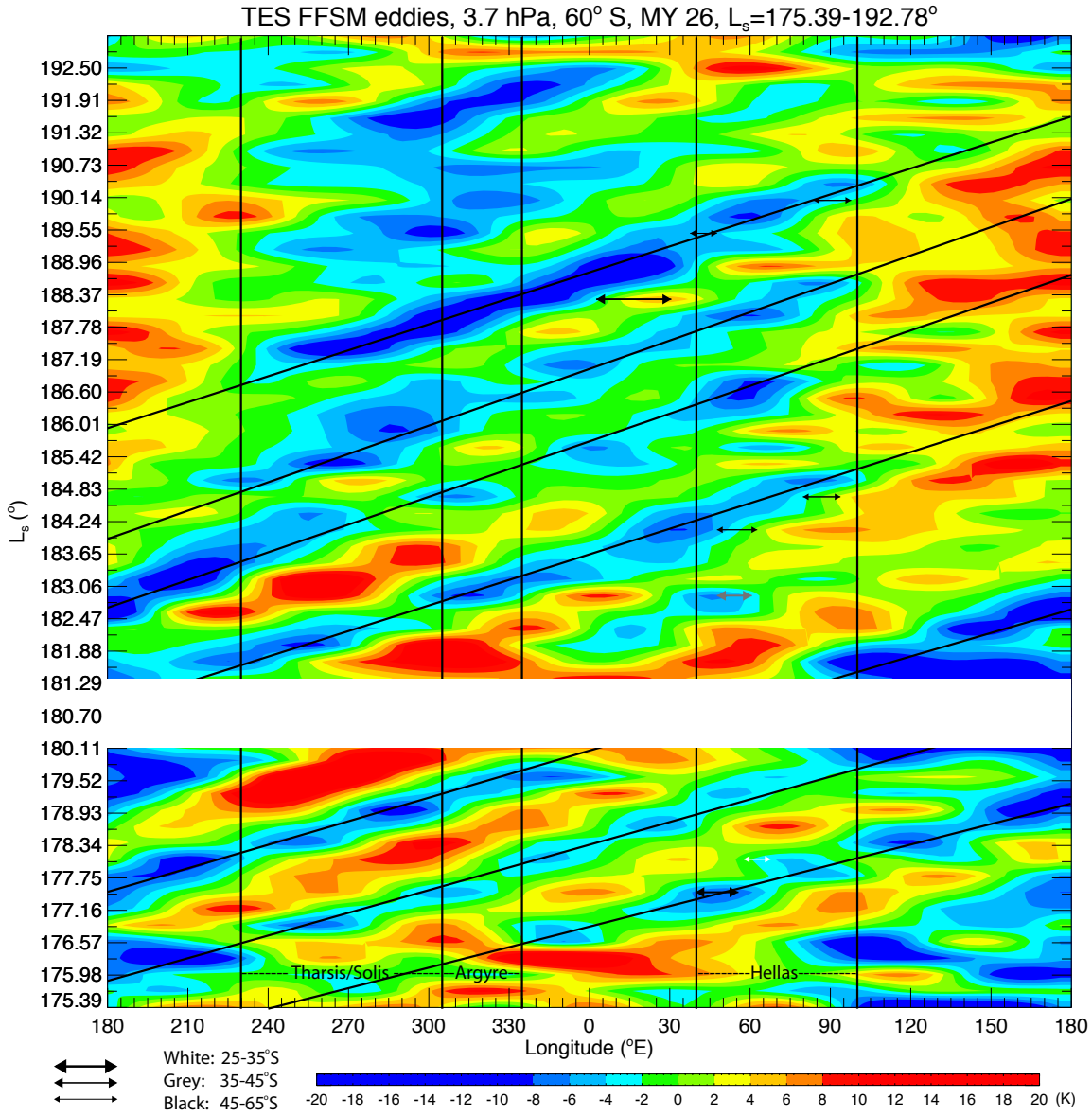

Figure 24. TES FFSM eddies, 3.7 hPa, 60° S, MY26, L_s=175.39–192.78°

MY 26 data show a different seasonal regime compared with MY 24 and 25. Cold centers appear to dominate the 90–220° E longitude corridor from L_s=175–183°, followed by a polarity switch to warm centers from L_s=183–192°. Several strong-

amplitude eddies propagate into Hellas during L_s =183–190°, although their coherency diminishes as they travel further eastward, possibly due to topographic disruption from the Hellas basin.

5.5 Phase and Periodicity

We computed the mean global phase speeds for MY 24–26 as 14.3, 13.8, 13.7 m s^{-1} respectively (Table 3). These show that MY 25 eddies were ~0.5 m s^{-1} slower than those in MY 24. These speeds are generally consistent with previous observations (Barnes 1981). We estimated the mean eddy periodicity in Hellas (60° E) to be P = 2.7, 2.9, and 3.1 sols for MY 24–26 respectively (Table 3). Power spectra for MY 24–25 Hellas (40–100° E, 60° S) eddies from L_s=165–188° show a dominant periodicity of ~3.5 sols for both years and values, along with moderately high adjacent amplitudes from 2.5–3.0 sols (Fig. 25).

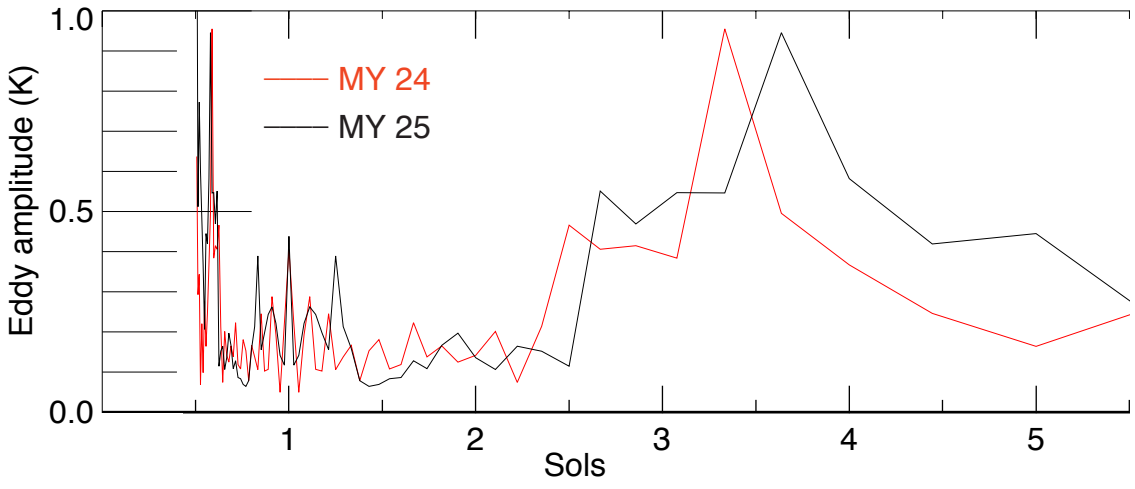

Figure 25. TES FFSM 3.7 hPa eddy power spectra, Hellas Sector (40–100° E, 60° S), L_s=165–188° MY 24 and 25.

Since there are 80 time steps (40 sols), wave 13 is 6.2 sols, and wave 14 is 5.7. The wide, moderate-amplitude (± 0.5 K) spread from 2.5–4 sols is due to wavenumber resolution and heterogeneous data.

Table 3. TES FFSM eddy phase speeds, *c*, and period, *P*, at 60° E, MY 24–26

~ L_s (°): eddy at 60° E	Eddy #	*c* (m/s) global MY 24	*c* (m/s) global MY 25	*c* (m/s) global MY 26	*P* (sols) Hellas MY 24	*P* (sols) Hellas MY 25	*P* (sols) Hellas MY 26
176.5	**E1**	12.8	13.8				
178.0	**E2**	13.4	14.5	15.6	2.7	2.8	
179.3	**E3**	14.1	14.8	14.3	2.6	2.5	2.8
181.0	**E4**	14.5	13.1	13.8	2.8	3.0	2.9
182.7	**E5**	15.2	13.5		2.7	2.9	
184.6	**E6**	16.0	13.8	12.9	2.5	2.8	
186.3	**E7**	13.8	13.2	11.8	2.9	3.3	3.7
	Mean:	14.3	13.8	13.7	2.7	2.9	3.1

5.6 Interannual Eddy Variability, MY 24–26

The data show moderate interannual variability of eddy activity in MY 24 and 25, and significant variability when comparing MY 26 with MY 24 and 25. In MY 24 and 25, maximum amplitude cold centers appear predominantly in the storm zone from 120–330° E. MY 25 eddies 1–3, however, are relatively high-amplitude in Hellas and low-amplitude in Tharsis. Figure 26 shows the evolution of MY 24–26 FFSM cold anomaly amplitudes in Hellas (45–90° E, 50–60° S). MY 25 eddies during the precursor phase are

moderately stronger amplitude than corresponding MY 24 eddies, and significantly stronger than those in MY 26 (Noble *et al.* 2011).

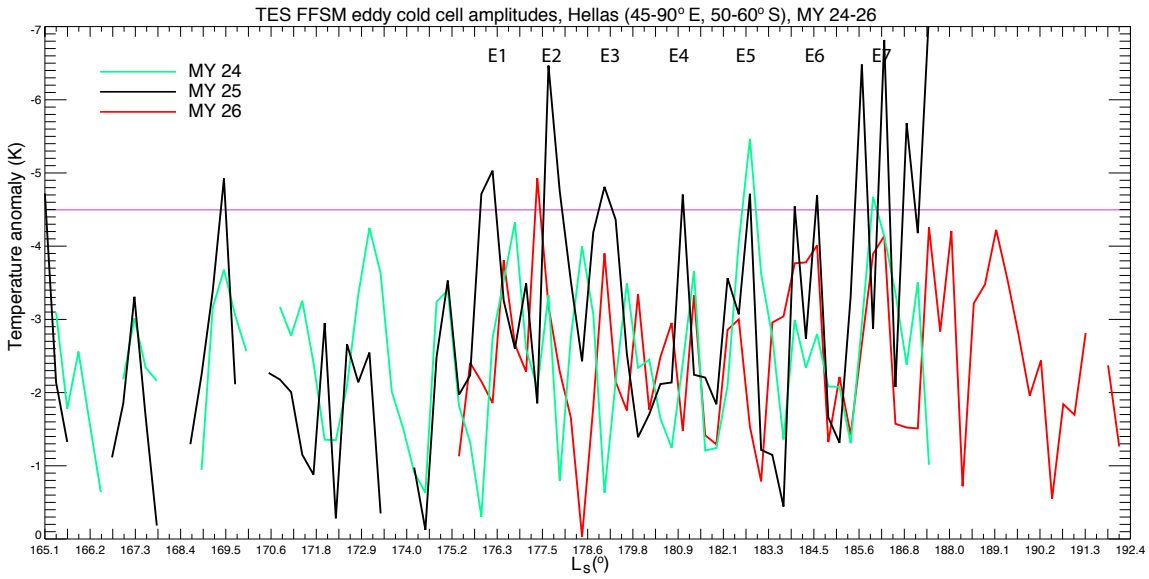

Figure 26. TES FFSM 3.7 hPa cold anomaly amplitudes vs. time, Hellas (45–90° E, 50–60° S), MY 24–26

In summary, we saw eastward propagating eddies every year during this season (L_s=165–192°). As we will discuss in Ch. 7.1, MY 25 was characterized by very coherent high-amplitude waves that appeared to be associated with the lifting events in Hellas. We hypothesized that these may have played a role in preconditioning the atmosphere.

6 Synthesized Dust Maps and Estimates of Dust Cloud Heights

6.1 Synthesized Dust Map Development

As discussed in Ch. 3.6, significant gaps exist in the TES dust opacity dataset. For example, TES opacity retrievals for L_s=187.5° are shown in Fig. 13. Significant data loss is evident in the SH from 60–150° E. In order to address this issue, we developed a novel method to integrate all relevant MGS data and produce synthesized dust maps that represent our best estimate of actual opacity values.

We supplemented TES opacity retrievals with the following data:

- binned and contoured TES opacity
- MGCM-derived opacity estimates (Wilson *et al.* 2011)
- MOC DGMs
- TES temperature contrasts: surface temperature (T_{sfc}) minus CO_2 frost point (T_{CO2}), 148 K; calculated for SH latitudes higher than 60° S
- spatial constraints of dust described by Cantor (2007)
    - haze ($\tau_d \leq 0.35$)
    - visually diffuse ($0.5 \leq \tau_d < 1.0$), surface features are visible but muted
    - visually opaque ($\tau_d \geq 1.0$), surface features are completely obscured
- MOC opacity measurements (Cantor 2010)

MGCM-derived opacity estimates are interpolated from several MGCM simulations with fixed opacities that yield brightness temperatures that bracket TES T_{sfc}

observations (Wilson *et al.* 2011). Derived values were carefully compared with TES (where available) and found to agree remarkably well, except in south polar regions with significant dust loading where derived values overestimate opacity (Fig. 11g, i).

We extended previous Fortran and IDL codes to: bin TES temperature and opacity data ($10° \times 5°$), perform quality control, generate contours, and superimpose data and contours on MOC DGMs. We created a map development environment (MDE) in Adobe Illustrator to synthesize available data, hand draw improved opacity contours, and generate composite opacity maps. IDL codes were then developed to combine opacity maps and write gridded NetCDF SDMs for MGCM input ($1° \times 1°$).

A daily MDE template was created with a 3600×1800 grid, major and minor longitude-latitude lines, and several clear-sky DGMs. All available datasets were imported into separate MDE layers. TES and MGCM-derived opacity ground tracks and contours were compared. Clearly erroneous opacity contours in areas of missing data were deleted, while reliable contours were kept and used as a base for synthesized opacity versions. An interpretive analysis was performed to extend, by hand, opacity contours at the haze and optically-thick levels (τ_d = 0.35 and 0.5) described by Cantor (2007). A qualitative visual characterization of haze and optically-thick dust boundaries was arrived at and used to interpolate τ_d = 0.35 and 0.5 contours between initial locations. Intermediary gradients and adjacent values were carefully filled in using available data for guidance.

Over the seasonal CO_2 icecap, we use TES $T_{sfc} - T_{CO2}$ (148 K) contours in conjunction with MOC imagery as first order guidelines for estimating opacity

distribution and magnitude where TES data are missing, and MGCM-derived opacity values are believed to be erroneous (overestimates described above) (Fig. 27).

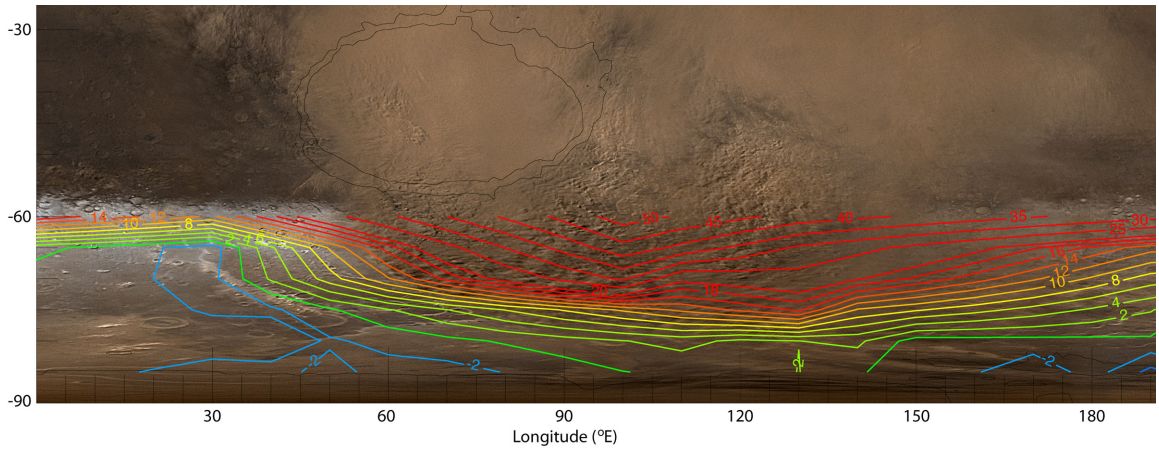

Figure 27. Contours of surface temperature minus CO_2 frost point (148 K), 60–90° S, L_s=187.5° Hellas quadrant, on MOC DGM.

This method assumes that the south polar cap (without dust on the cap or in the atmosphere) has a temperature of 148 K, and that any surface warming measured by TES (when dust is visible by MOC) is primarily due to atmospheric dust.

Two reference contours (τ_d = 0.2, 1.0) were initially drawn on the L_s=187.5° map (Fig. 11i). The τ_d=1.0 contour was drawn along the western edge of the visually opaque dust cloud (60° E, 62° S). The $T_{sfc} - T_{CO_2}$ = 14 K contour roughly follows this edge (Fig. 27). The dust cloud edge is relatively well defined, especially compared to the southern edge, which is distorted due to high-latitude stretching of the MOC DGM. The 14 K contour was then used as a guideline for the southern edge of the τ_d=1.0 contour (Fig. 27). The eastern edge of the cloud in MOC imagery was used as a guideline for the τ_d

=1.0 contour due to missing T_{sfc} data over the cap (near 140° E, 70° S, not shown) that possibly produced overestimates in $T_{sfc} - T_{CO2}$ contours.

The τ_d=0.2 contour was drawn over the $T_{sfc} - T_{CO2}$ = 2 K contour, assuming mild warming from dust haze. Intermediary values were then interpolated (Table 4) and contoured. All contours were then joined to corresponding ones north of 60° S. Finally, IDL codes were developed to combine map layers and produce gridded NetCDF files for MGCM input.

Table 4**.** Dust-induced temperature change estimates (south polar cap). TES dust optical depth and temperature estimates. Opacity descriptions: *diffuse*: $\tau_d \leq 0.35$, dust haze; *visually diffuse*: $0.5 \leq \tau_d < 1.0$ surface features are visible but muted; *visually opaque*: $\tau_d \geq 1.0$, surface features are completely obscured; *optically thick*: $\tau_d \geq 0.5$ (Cantor 2007).

τ_d (9-μm)	$\tau_{d\text{-}vis}$ (visible)	Visual description Cantor (2007)	$T_{sfc} - T_{CO2}$ estimate (K), 60–90° S
0.2	0.4	diffuse	2
0.35	0.7	diffuse	4
0.5	1.0	visually diffuse	5
0.6	1.2	visually diffuse	6
0.8	1.6	visually diffuse	10
1.0	2.0	visually opaque	14
1.2	2.4	visually opaque	18

6.2 SDM Results

The SDM for L_s=187.5° is shown in Fig. 11i, where IDL-generated contours of TES opacity have been supplemented with hand-drawn contours. The SDM for

L_s=189.9° is shown in Fig. 17g, where contours have been hand drawn using MOC-imagery as guidelines, along with data interpolation from previous and later sols. Figure 28 shows a comparison of before and after maps, where Fig. 28a shows TES gridded opacity, and Fig. 28b shows SDMs.

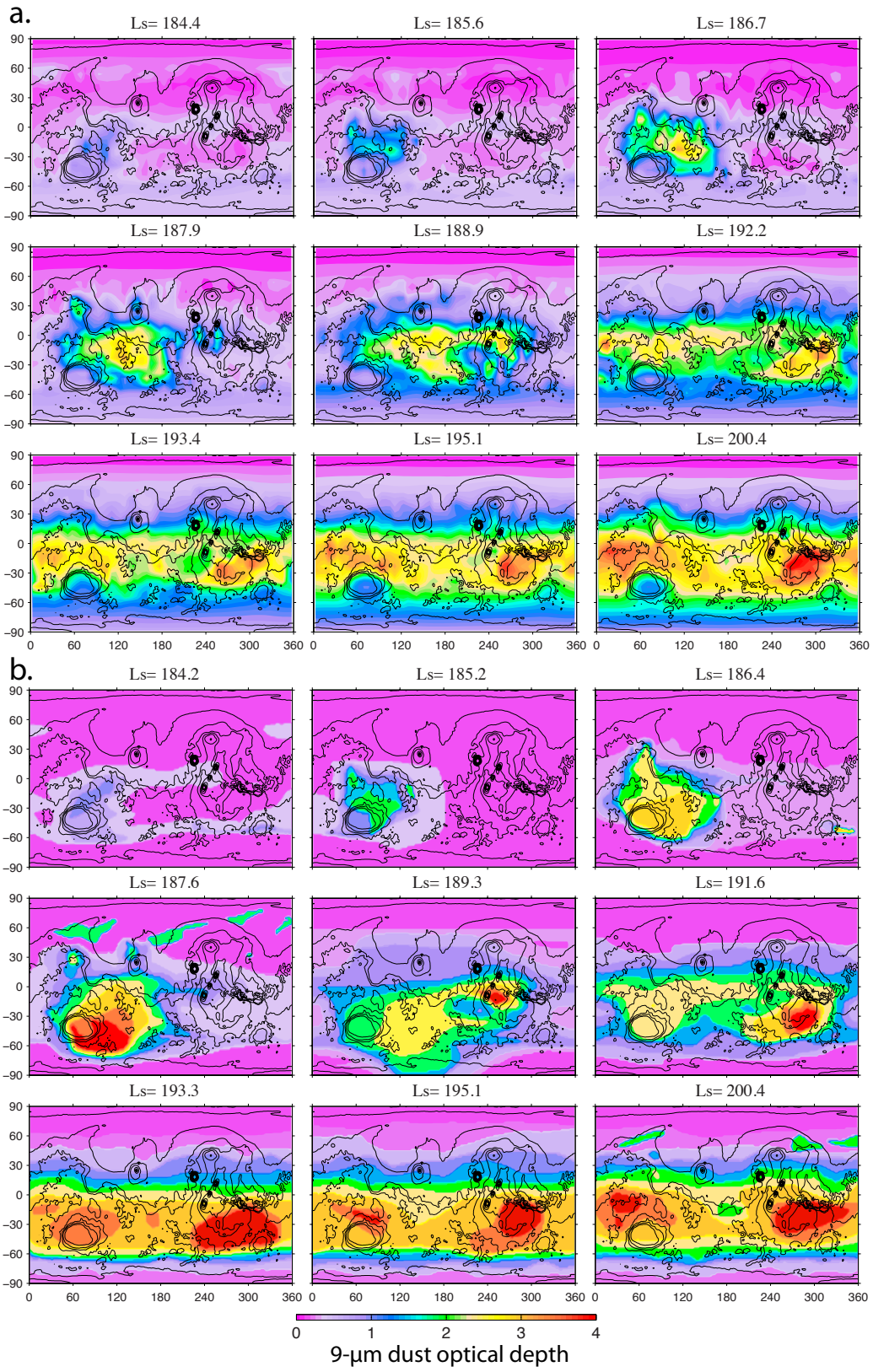
a.
Ls= 184.4
Ls= 185.6
Ls= 186.7
Ls= 187.9
Ls= 188.9
Ls= 192.2
Ls= 193.4
Ls= 195.1
Ls= 200.4
b.
Ls= 184.2
Ls= 185.2
Ls= 186.4
Ls= 187.6
Ls= 189.3
Ls= 191.6
Ls= 193.3
Ls= 195.1
Ls= 200.4
90
60
30
0
−30
−60
−90
0
60
120
180
240
300
360
0
1
2
3
4
9-μm dust optical depth

Figure 28. (a) Gridded TES dust opacity; (b) synthesized dust maps

Preliminary simulations with the improved opacity distribution have been conducted and presented by Wilson *et al.* (2008) (This author was a co-author on that work). Simulations using SDMs as input better predict the evolving temperature field that those using gridded TES opacity (Wilson 2012). SDMs are available in NetCDF format for the modeling community.

6.3 Estimates of Dust Cloud Height

Assuming that dust-induced radiative forcing is a significant component of the temperature tendency field, especially at mid-latitudes and in locations with large day-to-day opacity increases, then TES temperature differences from the previous sol (denoted hereafter as ΔT) can be used as a proxy for first-order estimates of and constraints on dust cloud heights. Cooling below a certain level suggests that dust extended vertically to at least that level, and steep warming above that level may indicate higher altitudes reached. Alternatively, maximum heights where ΔT is greater than a certain threshold (*e.g.* 6 or 8 K) may be used to constrain dust cloud heights. We used the following categories to describe positive and negative temperature changes: 0–2 K is termed noise; 2–4 K mild; 4–6 K moderate; > 6 K strong. We estimated dust cloud heights for the extratropical (western Cimmeria) and equatorial (west of Claritas) dust branches from L_s=184.7–186.4° and L_s=186.9–188.1°. This is a novel method for estimating dust cloud height.

The validity of our assumptions is complex and uncertain, since the total daily temperature change field is the sum of radiative (thermodynamic) and dynamical components. Radiative components include localized dust-induced forcing. Radiative sensitivity decreases towards the surface, where low-level temperatures are strongly influenced by surface heating. Heating efficiency increases with height, so that the high-altitude temperature response is greater than that at low-altitudes for a given amount of dust.

The dynamical components of the temperature tendency field which may influence temperature changes on diurnal time scales and longer include zonal and meridional circulations, along with thermal tides. Meridional circulations include the Hadley circulation. The rising branch of the Hadley circulation at the equator tends to transport dust and heat directly upward, while the high-latitude sinking branches produces dynamical (compressional) adiabatic heating. At L_s=170–180°, the rising branch of the Hadley circulation is confined to the tropics.

Thermal tides distort the dust-induced temperature response and make the temperature tendency field complex with significant uncertainty. Thermal tides (especially the diurnal tide) have large amplitudes in the tropics and are more pronounced at higher altitudes. Exciting the tide with large amounts of low-level dust in the tropics intensifies the vertical temperature gradient. The tide also has a vertical structure. Due to the diurnal tide alone, we expect minimum tropical temperatures at 2 pm with maxima at 2 am. Excitation of thermal tides results in upper level cooling and lower level warming in the daytime tropics. The response to upward movement is adiabatic cooling.

Dust heating at 4 hPa for example produces strong updrafts that produce increasing adiabatic cooling aloft (Wilson 2012). Thus, the effects of tides on the temperature tendency field become increasingly important with height, leading to greater uncertainties in our estimates at higher altitudes, especially in the equatorial dust branch.

Given the above caveats, we produced first order estimates of dust height in the extratropical (Fig. 29a) and equatorial (Fig. 29b) dust branches.

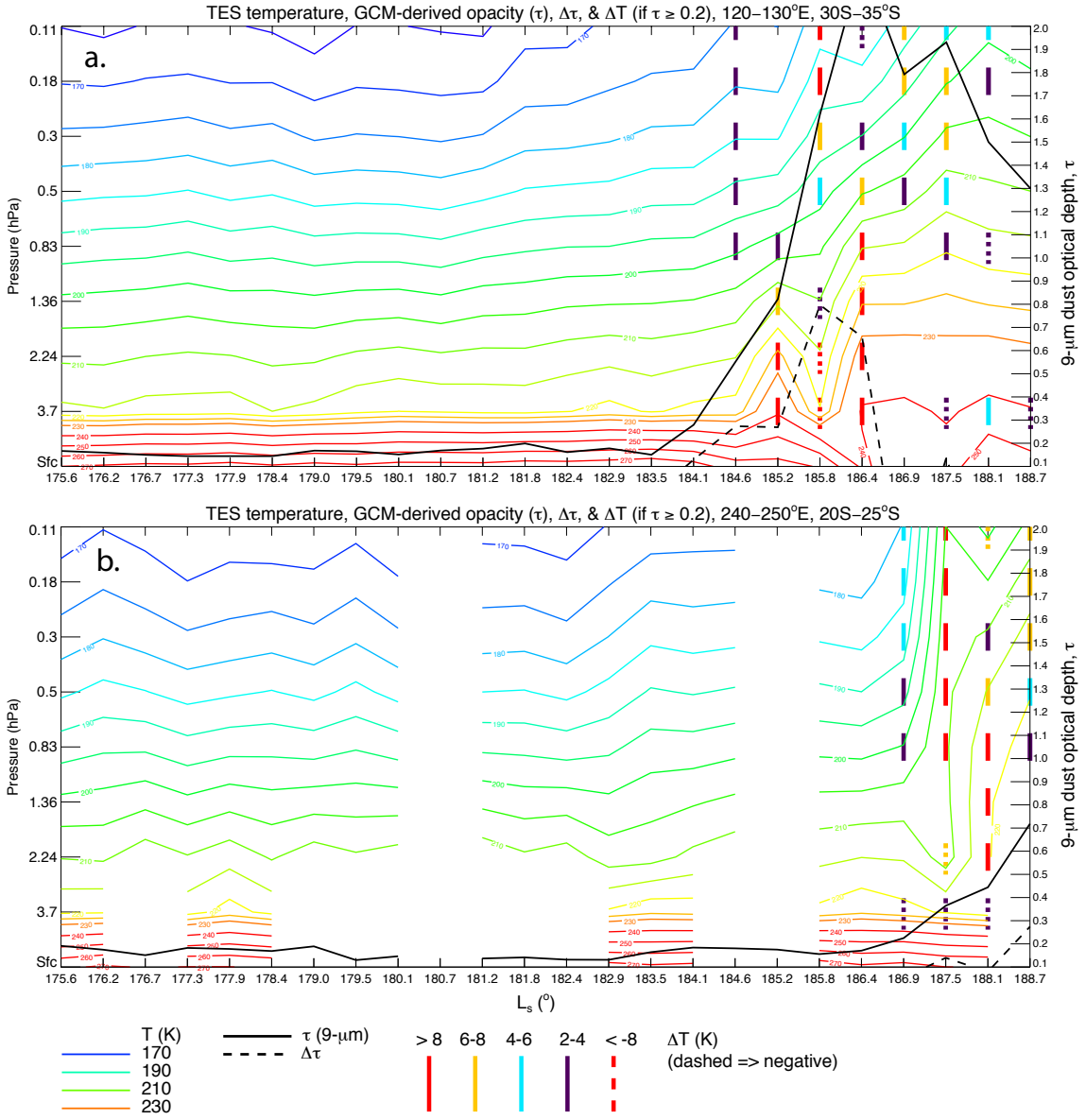

Figure 29. Time-height plots of TES temperature (thin colored lines), MGCM-derived opacity (solid black), $\Delta\tau$ (dashed black), and temperature change from previous sol (thick vertical colored bars), plotted if τ >0.2. (a) Cimmeria, 120–130° E, 30–35° S. (b) west of Claritas, 240–250° E, 20–25° S.

We assumed that all day-to-day temperature changes are dust-induced. Figure 29a shows the evolution of TES-measured thermal structure averaged across a region in western Cimmeria (120–130° E, 30–35° S) as a function of altitude and time from L_s=175.6–188.7°. Active dust lifting spread northeastward out of Hellas into western Promethei (to about 110° E) on L_s=184.7°, while extratropical haze ($\tau_d \approx 0.3$) transport extended to about 140° E. Mild warming was measured from 0.83 hPa and above, suggestive of dust haze transport at mid-levels (0.83 hPa or 21.5 km minimum). The following sol, L_s=185.3°, highly structured clouds extended to ~120° E. Figure 29a shows strong warming below 1.36 hPa, suggestive of significant dust loading below 1.36 hPa (16.2 km). On L_s=185.9° the dust storm spread eastward into Cimmeria (147°E) (Cantor 2007), causing steep column opacity increases above and cooling at and below 1.36 hPa throughout Promethei and Hesperia. These changes were observed from 100–130° E at 20–25° S, and from 120–130° E at 30–40° S. Figure 29a shows a subset of this region. This thermal structure suggests cloud heights of at least 1.36 hPa (~16.2 km), and probably higher due to observations of warming with height (*e.g.* 4–6 K at 0.5 hPa). Storm expansion continued on the following sol, L_s=186.4°, with τ_d = 2.4–2.8 maxima

measured in highly structured clouds in western Promethei. Figure 29a shows strong warming from 3.7 hPa to 0.83 hPa, suggestive of significant dust loading in this layer, and possibly higher. In Table 5 we show estimated dust cloud heights in western Cimmeria (120–130° E, 30–35° S) for 3 sols corresponding to L_s=185.3, 185.9, and 186.4°.

Table 5. Dust cloud height estimates from TES temperature changes, West Cimmeria (120–130° E, 30–35° S)

Time (°L_s)	Height (km)	Height (hPa)
185.3	16.2 – 21.5	1.36 – 0.83
185.9	27 – 38	0.5 – 0.18
186.4	21.5 - 27	0.83 – 0.5

The equatorial dust branch on L_s=187.5° widened to 10° N–20° S and extended eastward to Valles Marineris (Fig. 11i). Throughout a wide region west of Claritas (205–230° E, 5N–20° S), opacity increased to ~ 0.5, and upper level (0.3–0.1 hPa) temperatures increased by ~13 K, while cooling occurred at 2.2 hPa and below. Figure 29b shows the evolution of TES-measured thermal structure averaged across the region 240–250° E, 20–25° S as a function of altitude and time from L_s=175.6–188.7°. The spatial pattern of evolving opacity from L_s=187.5° and the previous sol suggests dust transport from tropical westerlies. Figure 13 shows maximum heights (diamonds) on L_s=187.5° where $\Delta T \geq 8$ K from the previous sol. Upper level warming was observed in a large area from 195–290° E, 0–40° S. The vertical structure of the dust cloud is

difficult to infer. Craters are clearly visible in MOC imagery of the region 210° E, 10° S at L_s=187.5°, and active lifting in the tropics appears to extend as far as 180° E (Fig. 13). These observations suggest that opacity increases west of Claritas are due to dust haze transport aloft, possibly from an anvil-shaped elevated dust cloud propagating eastward along the equator.

The above estimates of dust heights may provide useful observational constraints for model simulations. One of the most important questions to address is: which aspects of the observed temperature response are radiatively- *vs.* dynamically-forced? The radiative component is directly forced, while the dynamic can be more remotely forced. Model simulations are necessary to separate these components.

7 Discussion

7.1 Transient Eddies and Storm Genesis

FFSM analysis of TES temperatures (Barnes 2006) has shown that seven cold waves (E1–E7) propagated through Hellas during L_s=174–187°. We hypothesized that they were eastward-travelling baroclinic eddies due to the change in eddy structure with height, discussed in Ch. 5.1 (Fig. 20). As shown in Fig. 7, the eddies were very coherent at 3.7 hPa in the longitude range 200–90° E. The first eddy (E1) propagated through Hellas from L_s=175–177°. This corresponded to the first pulse of dust storm activity in Hellas described by Cantor (2007). Analysis of MOC-observed storms and FFSM eddies shows that the seven pulses of storm activity identified by Cantor (2007) (L_s=176.2–184.7°) occurred in the same time span as these six eddies (Fig. 7).

Integration and analysis of FFSM and MOC data during both MY 24 and 25 show that there were interesting temporal and spatial associations between the evolution of the eddies and the dust storms. In both years, storms appeared to move eastward concurrently with eddy propagation and with roughly comparable periodicities. This association was visible in MY 24 (Fig. 21) at L_s=169.9° (330 and 60° E), L_s=172.7° (0° E), and L_s=184.57° (290° E). During MY 25, this association was visible as eddies 1, 2, 3, 5, and 6 propagated through Hellas (Fig. 7). In addition, high-latitude storms (black arrows) tended to occur on the eastern side of an eddy, while lower (and some middle) latitude storms (white and grey arrows) occurred on the western side (Fig. 7). This can

be seen in Fig. 7 as eddies 2 and 5 passed through Hellas at ~ L_s=178 and 182° during MY 25.

The three panels in Fig. 8 also show interesting temporal and spatial associations between the evolution of the eddies and the dust storms in MY 25 Hellas. Figure 8a shows eddy 1 propagating through Hellas with two dust storms near the leading edges of large-amplitude cold centers (central and southeast Hellas). Figure 8b shows eddy 2 propagating through Hellas with a large dust storm near the leading edge of a large-amplitude cold center in southwest Hellas. Figure 8c shows mid- and low-latitude storms in northern Hellas two sols after eddy 6 propagated though central Hellas at 60° S. In all three cases, mid- and high-latitude dust storms occurred to the west of cold fronts. This observed spatial relationship is consistent with theory that predicts that southwesterly winds west of cold fronts cause dust lifting.

The following general pattern of eddy and dust storm evolution can be seen in MY 25 data (Figs. 7 and 8). Eddies propagated through Hellas in approximately three sols. On the first sol, cap-edge dust storms appeared in southwestern Hellas (40–60° E, 50–55° S) on the eastern edge of cold anomalies propagating into Hellas. On the next sol, the cold anomaly propagated into south-central Hellas (60–80° E, 50–55° S) triggering additional cap-edge storms. In addition, dust storm activity may have appeared in central Hellas (~40° S). On the last sol, the eddy propagated out of eastern Hellas. Dust storm activity was visible in southeastern Hellas (80–100° E, 50–55° S) and in northern and northeastern Hellas (~30° S). Eddies 2 and 5 typified this pattern. These results suggested a causal relationship between baroclinic eddies and local dust storm initiation.

It is unclear from the MOC imagery, however, if dust storms were propagating north- and northeastward over these three sols, or if they died down at night and new storms were triggered the following day.

Assuming that FFSM cold centers are baroclinic eddies, we hypothesized that northward storm evolution is due in part to northward winds associated with cold fronts. Cold fronts are a characteristic of baroclinic eddies, and in the SH, baroclinic eddies cause northward winds. These northward winds then cause northward movement of dust and or dust storms.

Although to first order we would locate cold fronts between cold (negative) and warm (positive) FFSM anomalies, their exact location cannot be determined from FFSM eddies alone – pressure and wind data are also required. The limited longitudinal resolution of TES data, and subsequent binning of FFSM data into 5° longitudinal bins, preclude precise determination of the location of cold fronts. Fronts are most intense close to the surface, but TES data averaging over the lowest scale height reduces their signal. Furthermore, we would expect a phase shift between eddy temperature and pressure fields, since isobaric and isosteric surfaces intersect under baroclinic conditions. The nature of Martian baroclinic waves and frontogenesis is understudied and consequently fronts have not been sufficiently investigated. There is a need to better characterize the relationship between cold fronts and surface stress, since the latter lifts dust. There is also a need to better characterize the role orography plays in disrupting SH transient eddies (Hollingsworth 2010).

It is important to note that the stronger cold eddies observed in the Hellas sector during the MY 25 precursor phase could be associated with regional cap edge circulations that are not propagating eastward. If these are present and their amplitude varies in time, they may be interpreted by the FFSM analysis procedure as transient eddies. Stronger cap edge circulations during this season in MY 25 could have been associated with a strengthening of the Hellas vortex at low levels (Barnes 2010). Numerical simulations predict the Hellas vortex to be a large-scale vortex with lower level convergence and upper level divergence that forms an anticyclonic circulation (CCW) aloft (Hollingsworth 2001).

We proposed that baroclinic eddies played a significant role in triggering the MY 25 precursor phase regional dust storms in Hellas. Surface stresses associated with eddy cold fronts were sufficient to lift dust, as seen in MY 24 and 25 MOC imagery. Determining the factors responsible for PDS genesis in MY 25 but neither 24 nor 26 is difficult. MY 24–26 eddy periodicities in Hellas of 2.7, 2.9, and 3.1 sols respectively show minor interannual variability, as well as global phase speeds of 14.3, 13.8, and 13.7 m s^{-1} (Table 3). It is unknown if these differences have any significance. The most notable difference seen in MY 25 eddies is the amplitude of E1–E7 eddies in Hellas (Fig. 26), with all seven MY 25 eddies having cold amplitudes less than –4.5 K. During this time period (L_s=176–186°), two eddies in MY 24 were colder than –4.5 K, and one in MY 26.

We hypothesized that the sustained series of high-amplitude eddies in MY 25 was a factor in generating the PDS seen in that year. The higher amplitudes seen in the FFSM

temperature field is suggestive of higher-amplitude eddies in general. These would have had higher-amplitude low-level wind and stress fields associated with them, and could have led to more dust lifting (assuming the same amount of dust available to lift). It is possible that other interannual differences in transient eddy activity were involved in MY 25 PDS genesis (such as very shallow disturbances (Barnes 2010), but these could not have been detected by TES. An important non-dynamical factor which can influence interannual variability of PDS occurrence includes surface dust inventory (Kahre *et al.* 2006).

We further hypothesized that constructive interference of transient eddies with other circulation components in MY 25, including sublimation flow, anabatic winds (daytime upslope), atmospheric tides (diurnal), and dust-induced thermal tides, may have contributed to the initiation, amplification, and sustained expansion of the precursory storms observed. Such a superposition of circulation components may increase surface stresses beyond the level needed to lift dust. Thereafter, dust lifted and suspended during the precursor phase greatly amplified thermal tides that in turn produce amplified wind fields that may have contributed to greater storm growth within, and expansion out of Hellas, compared to other years (Wilson 2012).

Both the lack and resolution of meteorological data limits the depth of analysis and precludes drawing firm conclusions about storm initiation, expansion, and interannual differences. It is not possible to assess the influence of various circulation components on MY 25 PDS genesis with the available MGS data. We are continuing to

conduct MGCM simulations to decompose such components and assess their contributions to storm initiation and expansion.

7.2 Quasi-stationary Wave One Evolution

The quasi-stationary wave one feature (especially pronounced at 2 pm – see Fig. 11j) exhibited a high degree of north-south symmetry in structure and amplitude. The eastward movement of the wave's peak (from about 50° E at L_s=181.8° to 150° E at L_s=188.1°) seen from TES 2 pm data at both 0.5 and 0.1 hPa, as well as MHSA temperature data, was roughly in phase with the eastward evolution of dust storms during this time. Figure 30 shows that the central longitude of dust storm activity moved eastward during this period (black line).

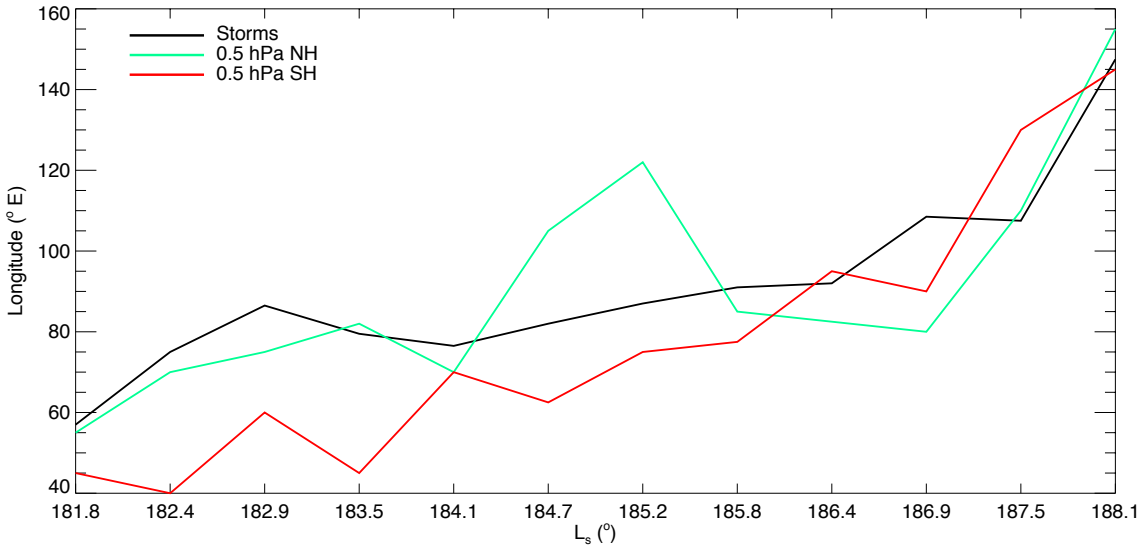

Figure 30. Zonal evolution of MOC-observed dust storms (central longitude) and TES 0.5 hPa 2 pm NH and SH wave one warm peaks

During the same period, the wave one peak in both northern and southern hemispheres also moved eastward (red and teal lines), covering about 90° in longitude over the 11 sol span. The corresponding wave at 2 am and 0.5 hPa exhibited similar north-south symmetry and also showed a NH warm peak moving from 55° E to 155° E, while the SH peak moved from 40° E to 190° E over the same time span (not shown).

The dynamical processes (and possible feedbacks) responsible for amplification, eastward movement, and relaxation of wave one are not fully understood. We hypothesized that wave amplification during the precursor phase was primarily due to a longitudinally-varying response to SH dust heating, and subsequent longitudinally-varying enhancement of the Hadley circulation. A topographically-forced component (from the Hellas basin) may have also contributed. Amplification in the Hellas quadrant was due to both dust-induced and dynamically-induced heating, while that in Utopia was predominantly dynamically-induced. Dust-induced heating in the southern hemisphere strengthened the equatorial rising branch of the Hadley circulation, leading to intensification of the descending branches, and subsequent increased dynamically-induced adiabatic (compressional) heating at high latitudes in both hemispheres (Haberle *et al.* 1982; Read and Lewis 2004; Smith *et al.* 2001). Adiabatic heating in the NH is evident in Fig. 18a between L_s=185.2–186.4°, where opacity has not increased significantly, yet warming at upper levels is greater than that at lower levels. The depth of the amplified wave in the SH mid- and high latitudes is consistent with deep dust heating.

The fact that warm peaks persisted in the Hellas hemisphere while cold troughs persisted in the Tharsis hemisphere at both 2 am and 2 pm from L_s=181.8–188.8° suggests a strong stationary component. North-south hemispheric symmetry may indicate excitation of a global mode. Additional factors may have contributed to wave amplification, including excitation of a semi-diurnal non-migrating tide and/or a diurnal tide. The former is prevalent at higher latitudes, while the latter is generally confined to the tropics. If wave amplification were purely due to the action of the diurnal tide, then a 180° shift of both peak and trough would be expected from 2 pm to 2 am. Such a shift, however, is not evident in the observations from L_s=184–187°.

From L_s=181.8–184.1°, the wave's northern and southern hemisphere warm peaks moved eastward to ~70° E (Figs. 11a–b, 29). As storm activity expanded eastward out of Hellas from L_s=184.2–187.5°, the wave's northern and southern hemisphere warm peaks moved from roughly 70° E to 110° E (NH) and 130° E (SH) (Figs. 11a–j, 29) and reached maximum amplitude. MOC imagery indicates that dust loading over the south polar cap peaked at the end of this period. Localized dust loading in the SH 40–150° E longitude sector contributed to temperatures increases, while sedimentation, eastward storm expansion, and dust transport during the following sols contributed directly to the SH temperature decrease, and also indirectly in both the SH and NH by weakening the Hadley circulation in the 40–150° longitude sector.

Wave one amplification enhanced a poleward component of the meridional circulation east of the SH warm peak due to geostrophy (Gawrych *et al.* 2004; Haberle *et*

al. 2005; Wilson 2012). In addition, wave one amplification displaced the westerly extratropical jet poleward (Hollingsworth 2010). The jet at this season is typified by weak surface winds that increase in speed with height. We suggested that both of these components contributed to southward dust advection, causing greater warming and wave one amplification.

The SH and NH wave one warm peaks moved to 140 and 160° E respectively as dust lifting was initiated in Claritas on L_s=188.2° and the equatorial and extratropical dust branches also moved further eastward (Figs. 17a–b, 29). As storm activity spread throughout Daedalia, Solis, and Aonia on L_s=189.9°, the SH warm peak migrated to ~250° E (Figs. 17g–h). As dust clouds over the south polar cap dissipated and SH temperatures became more zonally uniform after L_s=190°, wave one amplitude decayed, and the atmosphere relaxed back to a more zonally uniform state. This happened at approximately the same time in both hemispheres.

The relationship and dynamical linkages between the wave one structure reaching maximum amplitude on L_s=187.5° and dust lifting initiation in Claritas the following sol is not well understood. We hypothesized that the perturbation caused by regional atmospheric heating in the Hellas sector excited a global teleconnection, possibly a Rossby wave train, that propagated from Hellas to Claritas and initiated dust lifting on L_s=188.2° (Bridger 2010; Noble *et al.* 2006). Winds associated with tidal amplification, augmented by upslope/downslope flows near Arsia Mons, may have also contributed to the onset of lifting. Preliminary NASA-MGCM simulations predict a significant global correlation of meridional winds between Hellas and Claritas in MY 25. MGCM output

shows significant structures in this correlation that seem to be emanating from the region east of Hellas. Structures with the highest correlation are located near Claritas. MY 24 simulations show that global correlations such as these are absent.

7.3 Globally-averaged Opacity and Temperatures

Steep opacity and temperature changes are apparent in the first half of the expansion phase (Fig. 5), where rising opacity levels cause 0.5 hPa 2 pm temperatures to increase due to IR emission from dust at that height. A secular downward trend in surface temperature was observed during the expansion and mature phases due to absorption of solar radiation aloft and subsequent blocking at the surface. Diurnally-averaged surface and 0.5 hPa temperatures are nearly isothermal (~213 K, circled) at L_s=213° (Fig. 5). Increased static stability associated with an isothermal atmosphere is thought to be a mechanism that suppresses dust lifting (Briggs *et al.* 1979), although models do not predict this (Murphy *et al.* 1995; Wilson 2012).

Globally-averaged daytime surface temperatures decreased by 23 K at the height of the PDS, compared to the previous Martian year, while nighttime surface temperature increased by ~20 K due to increased IR emittance from suspended aerosols. These observations are consistent with theories, models, and previous observations indicating that reflection of shortwave radiation by aerosols aloft will cause daytime surface cooling, while nighttime IR radiation emitted from the atmosphere will increase surface temperatures (Haberle *et al.* 1982).

8 Conclusions

We have integrated and examined all available MGS observations of the MY 25 PDS in order to determine which circulation components were involved in storm onset and evolution (Haberle *et al.* 2005; Noble *et al.* 2006). Integration of MGS data has enabled analysis of storm development in conjunction with the evolving temperature and opacity fields. Specifically, we have looked at these co-existing phenomena: i) FFSM eddies in the temperature field and storms observed at the same time via MOC imagery; ii) a quasi-stationary wave one structure in temperature field, which evolved in concert with TES-measured opacity, and MOC-observed storms; and iii) the evolving vertical thermal structure of the atmosphere, the TES opacity field, and MOC-observed storms. We have also produced two types of synthesized dust maps (column and structured) in order to supplement missing TES dust opacity data at important sols during the precursor and expansion phases of the MY 25 PDS. These maps are being used as MGCM input for storm simulations (Wilson *et al.* 2008).

Based on our analysis of these MGS data, we propose the following working hypothesis to explain the dynamical processes responsible for PDS initiation and expansion. Six eastward-traveling transient baroclinic eddies triggered the MY 25 precursor storms in Hellas during L_s=176.2–184.6° due to the enhanced dust lifting associated with their low-level wind and stress fields. This was followed by a seventh eddy that contributed to expansion on L_s=186.3°. Increased opacity and temperatures from dust lifting associated with the first three eddies enhanced thermal tides which supported further storm initiation and expansion out of Hellas. Constructive interference

of eddies and other circulation components including sublimation flow, anabatic winds (daytime upslope), and diurnal tides may have contributed to storm onset in and expansion out of Hellas.

Opacity distributions obtained by TES during the precursor phase show that suspended dust was then transported north- and northeastward where it was both lifted by the rising branch of the Hadley circulation and transported eastward by tropical westerlies. A large-amplitude quasi-stationary wave-one temperature structure developed and amplified due to a longitudinally asymmetric Hadley circulation, which itself developed in response to the concentrated dust-induced heating in Hellas. Both dust-induced and dynamically-induced heating contributed to the amplification of this wave one structure in the SH temperature field, while NH amplification was dynamically-induced.

The amplification of the stationary wave caused an enhancement of the meridional circulation that in turn advected dust over the south polar cap. As dust reached higher altitudes in the 50–180° E longitude sector, the subsequent heating over a deep layer of the atmosphere caused continued amplification of wave one, exciting a Rossby wave train that propagated into the opposite hemisphere. The stress field associated with this wave train is hypothesized to have led to new dust lifting events downstream. One sol after wave one reached its maximum amplitude (L_s=187.5°), dust lifting began in the Syria-Claritas region, a development possibly related to the propagating Rossby wave train. Lifting in this region, which became the major source of atmospheric dust in the PDS, may have been sustained by enhanced thermal tides augmented by

upslope/downslope flows. Zonal mean westerlies and the mean meridional circulation affected the largely eastward movement of dust during storm onset, and its eventual northward and global dispersion.

Our analysis has yielded important results regarding the dynamical response of the atmosphere to dust loading and the evolution of the dust storm. Results from this investigation have been used to validate the NASA-Ames MGCM. Integration of MGS data has increased our understanding of PDS dynamical processes and allowed us to develop an improved quantitative description of storm evolution that may be used to constrain both estimates of horizontal dust distribution and modeling of storm initiation and expansion. We are continuing to refine our dust opacity maps and use them as input into both the NASA and GFDL MGCMs. In future work we will present model results that relate the simulated circulation and atmospheric temperature and aerosol distributions to the available observations in an effort to better understand the underlying dynamics of the initiation and growth of the MY 25 PDS.

9 Appendix - Acronyms

DGM	Daily global map
FFSM	Fast Fourier Synoptic Mapping
GFDL	Geophysical Fluid Dynamics Laboratory
IDL	Interactive Data Language
MDE	Map development environment
MGCM	Mars general circulation model
MGS	Mars Global Surveyor
MHSA	Mars Horizon Sensor Assembly
MOC	Mars Orbiter Camera
MRO	Mars Reconnaissance Orbiter
MY	Mars Year
NH	Northern hemisphere
PDS	Planet-encircling dust storm
SDM	Synthesized dust opacity map
SH	Southern hemisphere
TES	Thermal Emission Spectrometer

10 References

Albee, A., 2001: Introduction to the special section: The Mars Global Surveyor mission. *Journal of Geophysical Research*.

Albee, A., F. Palluconi, and R. E. Arvidson, 1998: Mars global surveyor mission: overview and status. *Science*, **279,** 1671-1672.

Anderson, E., and C. B. Leovy, 1978: Mariner 9 television limb observations of dust and ice hazes on Mars. *Journal of the Atmospheric Sciences*, **35,** 723-734.

Anonymous, 1666: Observations Made in Italy, Confirming the Former, and Withall Fixing the Period of the Revolution of Mars. *Philosophical Transactions of the Royal Society*, **1,** 242-245.

Antoniadi, E. M., 1916: Mars, On a probable relation between the changes in solar radiation and the melting of the Polar Snow Caps of Mars. *Monthly Notices of the Royal Astronomical Society*, **76,** 643-645.

Antoniadi, E. M., 1930: *La planète Mars*. Hermann & Co.

Arvidson, R. E., E. Guiness, H. J. Moore, and J. Tillman, 1983: Three Mars years: Viking Lander 1 imaging observations. *Science*, **222,** 463-468.

Bandfield, J. L., and M. Smith, 2003: Multiple emission angle surface-atmosphere separations of thermal emission spectrometer data. *Icarus*, **161,** 47-65.

Banfield, D., B. J. Conrath, P. J. Gierasch, and R. J. Wilson, 2004: Traveling waves in the martian atmosphere from MGS TES Nadir data. *Icarus***,** 365-403.

Banin, A., 1993: The mineralogy and formation processes of Mars soil. *MSATT Workshop on Chemical Weathering on Mars (Technical Report 93-01, 1-2)*, LPI.

Barnes, J., 1981: Midlatitude Disturbances in the Martian Atmosphere: A Second Mars Year. *Journal of the Atmospheric Sciences*, **38,** 225-234.

Barnes, J., J. B. Pollack, R. Haberle, and C. B. Leovy, 1993: Mars Atmospheric Dynamics as Simulated by the NASA Ames General Circulation Model 2. Transient Baroclinic Eddies. *Journal of Geophysical Research. E. Planets*, **98**.

Barnes, J. R., 1980: Time spectral analysis of midlatitude disturbances in the Martian atmosphere. *Journal of the Atmospheric Sciences*, **37,** 2002-2015.

Barnes, J. R., 2001: Asynoptic fourier transform analyses of MGS TES data: Transient baroclinic eddies. *Bulletin of the American Astronomical Society*, **33,** 1088.

Barnes, J. R., 2003: Mars Weather Systems and Maps: FFSM Analyses of MGS TES Temperature Data. *Sixth International Conference on Mars*, Pasadena, California, USA.

Barnes, J. R., 2006: FFSM Studies of Transient Eddies in the MGS TES Temperature Data. *Mars Atmosphere Modelling and Observations*, Granada, Spain.

Barnes, J. R., 2010: Personal Communication.

Bridger, A. F. C., 2010: Personal Communication.

Briggs, G. A., and C. B. Leovy, 1974: Mariner 9 observations of the Mars north polar hood. *Bull. Am. Meteorol. Soc.*

Briggs, G. A., W. Baum, and J. R. Barnes, 1979: Viking Orbiter imaging observations of dust in the Martian atmosphere. *Journal of Geophysical Research*, **84,** 2795-2820.

Burk, S. D., 1976: Diurnal winds near the Martian polar caps. *Journal of Atmospheric Sciences*, **33,** 923-939.

Campbell, W. W., 1894: Concerning an Atmosphere on Mars. *Publications of the Astronomical Society of the Pacific*, **6,** 273-283.

Cantor, B., 2007: MOC observations of the 2001 Mars planet-encircling dust storm. *Icarus*, **186,** 60-96.

Cantor, B., 2010: Personal Communication.

Cantor, B., M. Caplinger, P. James, and M. J. Wolff, 2001: Martian dust storms: 1999 Mars Orbiter Camera observations. *Journal of Geophysical Research*, **106,** 23653-23687.

Cassini, J., 1707: Observation de l'éclipse de Mars par la Lune faite à Montpellier et à Marseille. *Mémoires de mathématique et de physique de l'Académie royale des sciences*, L'Académie royale des sciences, 193-195.

Christensen, P. R., J. L. Bandfield, V. E. Hamilton, and S. W. Ruff, 2001: Mars Global Surveyor Thermal Emission Spectrometer experiment- Investigation description and surface science results. *Journal of Geophysical Research*, **106,** 23823-23871.

Christensen, P. R., D. L. Anderson, S. C. Chase, R. N. Clark, H. H. Kieffer, M. C. Malin, J. C. Pearl, J. Carpenter, N. Bandiera, F. G. Brown, and S. Silverman, 1992: Thermal Emission Spectrometer Experiment: Mars Observer Mission. *Journal of Geophysical Research*, **97,** 7719-7734.

Clancy, R., B. Sandor, M. Wolff, P. Christensen, M. Smith, J. Pearl, B. Conrath, and R. Wilson, 2000: An intercomparison of ground-based millimeter, MGS TES, and Viking atmospheric temperature measurements- Seasonal and interannual variability of temperatures and dust loading in the global Mars atmosphere. *Journal of Geophysical Research*, **105,** 9553-9571.

Clancy, R. T., E. Lellouch, Y. N. Billawala, B. Sandor, and D. Rudy, 1994: Microwave observations of a 1994 Mars global dust storm. *Bull. Am. Astron. Soc.*, **26,** 1130.

Clancy, R. T., S. W. Lee, G. R. Gladstone, W. W. McMillan, and T. Rousch, 1995: A new model for Mars atmospheric dust based upon analysis of ultraviolet through infrared observations from Mariner 9, Viking, and Phobos. *Journal of Geophysical Research*, **100,** 5251-5263.

Clancy, R. T., A. W. Grossman, M. J. Wolff, P. B. James, D. Rudy, Y. Billawala, B. Sandor, S. Lee, and D. Muhleman, 1996: Water Vapor Saturation at Low Altitudes around Mars Aphelion: A Key to Mars Climate? *Icarus*, **122,** 33-62.

Clancy, T., M. J. Wolff, P. James, R. Haberle, and B. Cantor, 2006: Mars Weather and Ozone Column Mapping with MRO/MARCI. *Mars Atmosphere modeling conference*.

Conrath, B. J., 1981: Planetary-scale wave structure in the Martian atmosphere. *Icarus*, **48,** 246-255.

Conrath, B. J., J. C. Pearl, M. Smith, W. Maguire, P. R. Christensen, S. Dason, and M. Kaelberer, 2000: Mars Global Surveyor Thermal Emission Spectrometer(TES) observations: Atmospheric temperatures during aerobraking and science phasing. *Journal of Geophysical Research*, **105**.

Dollfus, M., 1948: Étude polarimétrique de la lumière réfléchie par les nuages et l'atmosphère de la planète *Compt. Rend. Acad. Sci. (Paris)*, **227,** 383.

Ebisawa, S., and A. Dollfus, 1986: Martian Dust Storms at the Early Stage of their Evolution. *Icarus*, **66,** 75-82.

Elteto, A., 2009: Martian Global Dust Storm 2001A as observed by the Mars Global Surveyor Thermal Emission Spectrometer, Department of Astrophysical and Planetary Sciences, University of Colorado.

Fernandez, W., 1999: Martian Dust Storms: A Review. *Earth, Moon and Planets*, **77,** 19-46.

Flammarion, C., 1892: *La planéte Mars et ses conditions d'habitabilité: Synthèse générale de toutes les observations*. Vol. I, Gauthier-Villars et Fils, Imprimeurs-Libraires de l'observatoire de Paris.

Gawrych, J., R. M. Haberle, M. Malin, B. A. Cantor, and M. D. Smith, 2004: Analysis of the 2001 global dust storm with a Mars general circulation model. *Bulletin of the American Astronomical Society*, 1171.

Gierasch, P., 1974: Martian dust storms. *Reviews of Geophysics and Space Physics*, **12,** 730-734.

Gierasch, P. J., and R. M. Goody, 1973: A Model of a Martian Great Dust Storm. *Journal of the Atmospheric Sciences*, **30,** 169-179.

Glasstone, S., 1968: *The book of Mars*. NASA, 315 pp.

Haberle, R., 1986: Interannual Variability of Global Dust Storms on Mars. *Science*, **234,** 459-461.

Haberle, R., C. Leovy, and J. B. Pollack, 1982: Some effects of global dust storms on the atmospheric circulation of Mars. *Icarus*, **50,** 322-367.

Haberle, R., J. Noble, J. Murphy, A. F. C. Bridger, J. Hollingsworth, J. R. Barnes, B. Cantor, M. C. Malin, and M. Smith, 2005: Synthesis of MGS Observations of the 2001 Global Dust Storm on Mars: Implications for Atmospheric Dynamics. *American Geophysical Union*, San Francisco, CA, USA.

Haberle, R. M., 1997: Mars: Atmosphere. *Encyclopedia of Planetary Sciences*, J. H. Shirley, and R. W. Fairbridge, Eds., Springer, 432-440.

Haberle, R. M., 2003: Planetary Atmospheres: Mars. *Encyclopedia of Atmospheric Sciences*, J. R. Holton, J. A. Curry, and J. A. Pyle, Eds., Academic Press, 1745-1755.

Haberle, R. M., C. B. Leovy, and J. B. Pollack, 1979: A numerical model of the Martian polar cap winds. *Icarus*, **39,** 151-183.

Haberle, R. M., J. B. Pollack, J. R. Barnes, R. W. Zurek, C. B. Leovy, J. Murphy, H. Lee, and J. Schaeffer, 1993: Mars Atmospheric Dynamics as Simulated by the NASA Ames General Circulation Model 1. The Zonal-Mean Circulation. *Journal of Geophysical Research*, **98,** 3903-3123.

Herschel, W., 1784: On the Remarkable Appearances at the Polar Regions of the Planet Mars, the Inclination of Its Axis, the Position of Its Poles, and Its Spheroidical Figure; With a Few Hints Relating to Its Real Diameter and Atmosphere. *Philosophical Transactions of the Royal Society*, **74,** 233-273.

Hess, S., 1948: A meteorological approach to the question of water vapor on Mars and the mass of the Martian atmosphere. *Publications of the Astronomical Society of the Pacific*, **60,** 289-302.

Hess, S., 1950: Some aspects of the Meteorology of Mars. *Journal of Meteorology*, **7,** 1-13.

Hinson, D., and R. Wilson, 2002: Transient eddies in the southern hemisphere of Mars. *Geophysical Research Letters*, **29**.

Hinson, D. P., and H. Wang, 2009: Further observations of regional dust storms and baroclinic eddies in the northern hemisphere of Mars. *Icarus*, **206,** 290-305.

Hollingsworth, J. L., 2001: Stationary Vortices in Southern Midlatitudes on Mars. *American Geophysical Union, Fall Meeting*, San Francisco, CA, USA.

Hollingsworth, J. L., 2005: Large-Scale Weather Systems in Mars' Southern Hemisphere: Effects of the Great Impact Basins. *American Geophysical Union, Fall Meeting*, San Francisco, CA, USA.

Hollingsworth, J. L., 2010: Personal Communication.

Hollingsworth, J. L., R. M. Haberle, and A. F. C. Bridger, 1996: Orographic control of storm zones on Mars. *Nature*, **380**.

Hollingsworth, J. L., M. A. Kahre, and R. Haberle, 2008: Mars' Southern Hemisphere: Influences of the Great Impact Basins on Extratropical waether and the water cycle. *LPI Contributions*.

Hunt, G., E. Mitchell, and A. Peterfreund, 1980: The opacity of some local Martian dust storms observed by the Viking IRTM. *Icarus*, **41,** 389-399.

Ingersoll, A. P., and J. R. Lyons, 1993: Mars dust storms: Interannual variability and chaos. *Journal of Geophysical Research*, **98,** 10951-10961.

James, P. B., 1985: Martian Local Dust Storms. *Recent Advances in Planetary Meteorology*, G. E. Hunt, Ed., Cambridge University Press.

James, P. B., H. H. Kieffer, and D. A. Paige, 1992: The seasonal cycle of carbon dioxide on Mars. *Mars*, H. H. Kieffer, B. M. Jakosky, C. W. Snyder, and M. S. Matthews, Eds., University of Arizona Press, 934-968.

Kahn, R. A., T. Z. Martin, R. W. Zurek, and S. W. Lee, 1992: The Martian dust cycle. *Mars*, H. H. Kieffer, B. M. Jakosky, C. W. Snyder, and M. S. Matthews, Eds., University of Arizona Press, 1017-1053.

Kahre, M. A., J. R. Murphy, and R. M. Haberle, 2006: Modeling the Martian dust cycle and surface dust reservoirs with the NASA Ames general circulation model. *Journal of Geophysical Research*, **111,** E06008.

Leovy, C., 2001: Weather and climate on Mars. *Nature*, **412,** 245-249.

Leovy, C., J. Tillman, W. Guest, and J. Barnes, 1985: Interannual variability of Martian weather. *Recent Advances in Planetary Meteorology*.

Leovy, C. B., R. W. Zurek, and J. B. Pollack, 1973: Mechanisms for Mars dust storms. *Journal of the Atmospheric Sciences*, **30,** 749-762.

Leovy, C. B., G. A. Briggs, A. T. Young, B. A. Smith, and J. B. Pollack, 1972: The Martian Atmosphere: Mariner 9 Television Experiment Progress Report. *Icarus*, **17,** 373-393.

Luhmann, J. G., C. T. Russell, L. H. Brace, and O. L. Vaisberg, 1992: The intrinsic magnetic field and solar-wind interactions of Mars. *Mars*, H. H. Kieffer, B. M. Jakosky, C. W. Snyder, and M. S. Matthews, Eds., University of Arizona Press, 1090-1134.

Malin, M. C., G. E. Danielson, A. P. Ingersoll, H. Masursky, J. Veverka, M. A. Ravine, and T. A. Soulanille, 1992: Mars observer camera. *Journal of Geophysical Research*, **97,** 7699-7718.

Martin, L. J., 1984: Clearing the Martian air: The Troubled History of Dust Storms. *Icarus*, **57,** 317-321.

Martin, L. J., and R. W. Zurek, 1993: An Analysis of the History of Dust Activity on Mars. *Journal of Geophysical Research*, **98,** 3221-3246.

Martin, T. Z., 1986: Thermal infrared opacity of the Mars atmosphere. *Icarus*, **66,** 2-21.

Martin, T. Z., 1997: Horizon Science Experiment for Mars Global Surveyor. *Bulletin of the American Astronomical Society*.

Martin, T. Z., and J. Murphy, 2003: Atmospheric wave structure derived from Mars global surveyor horizon sensor data. *Mars atmosphere modelling observations*, Granada, Spain.

McKim, R., 1996: The dust storms of Mars. *Journal of the British Astronomical Association*, **106,** 185-200.

Menzel, D., 1926: The atmosphere of Mars. *The Astrophysical Journal*, **63,** 48-59.

Montabone, L., S. R. Lewis, and P. L. Read, 2005: Interannual variability of Martian dust storms in assimilation of several years of Mars global surveyor observations. *Advances in Space Research*, **36**.

Murphy, J., 2010: Personal Communication.

Murphy, J., T. Martin, M. Blackmon, and S. Nelli, 2001: Quantification of high frequency thermal waves in the martian atmosphere: Analysis of MGS Horizon Sensor atmospheric temperatures. *Bulletin of the American Astronomical Society*, **33,** 1072.

Murphy, J., J. B. Pollack, J. Schaeffer, R. Haberle, C. B. Leovy, and O. Toon, 1995: Three-dimensional numerical simulation of Martian global dust storms. *Journal of Geophysical Research*, **100,** 26357-26376.

Newman, C. E., S. R. Lewis, and P. L. Read, 2002a: Modeling the Martian dust cycle 2. Multiannual radiatively active dust transport simulations. *Journal of Geophysical Research*, **107,** 15.

Newman, C. E., P. L. Read, and S. R. Lewis, 2002b: Modeling the Martian dust cycle 1. Representations of dust transport processes. *Journal of Geophysical Research*, **107**.

Newman, C. E., P. L. Read, and S. R. Lewis, 2004: Investigating atmospheric predictability on Mars using breeding vectors in a general-circulation model. *Quarterly Journal of the Royal Meteorological Society*, **130,** 2971-2989.

Noble, J., R. J. Wilson, R. M. Haberle, J. L. Hollingsworth, M. A. Kahre, J. R. Barnes, A. F. C. Bridger, and B. A. Cantor, 2011: Comparison of TES FFSM Eddies and MOC Storms, MY24-26. *Fourth International Workshop on the Mars Atmosphere: Modelling and observations*, Paris, France, CNES, ESA, NASA.

Noble, J., R. M. Haberle, A. Bridger, J. Murphy, J. L. Hollingsworth, J. Barnes, B. Cantor, M. Malin, and M. Smith, 2006: Synthesis of MGS observations of the

2001 global dust storm on Mars. *Second International Workshop on the Mars Atmosphere: Modelling and Observations*, Granada, Spain, CNES, ESA, NASA.

Noble, J., R. M. Haberle, A. F. C. Bridger, J. Wilson, J. R. Barnes, J. Murphy, J. Hollingsworth, M. C. Malin, B. Cantor, M. Smith, and T. Martin, 2007: Integration of MGS Observations of the 2001 Global Dust Storm on Mars: Implications for Atmospheric Modeling. *AGU Fall Meeting*, San Francisco, CA, USA, American Geophysical Union.

Owen, T., 1992: The Composition and Early History of the Atmosphere of Mars. *Mars*, H. H. Kieffer, B. M. Jakosky, C. W. Snyder, and M. S. Matthews, Eds., University of Arizona Press, 818-834.

Parsons, J. D., 2000: Are fast-growing Martian dust storms compressible? *Geophysical Research Letters*, **27,** 2345-2348.

Pickering, W. H., 1905: Martian Meteorology. *Annals of Harvard College Observatory*, **53,** 155-171.

Pollack, J. B., D. Colburn, F. Flasar, R. Kahn, C. Carlston, and D. Pidek, 1979: Properties and effects of dust particles suspended in the Martian atmosphere. *Journal of Geophysical Research*, **84,** 2929-2945.

Rafkin, S., 2009: A positive radiative-dynamic feedback mechanism for the maintenance and growth of Martian dust storms. *Journal of Geophysical Research*, **114,** E01009.

Read, P. L., and S. R. Lewis, 2004: *The Martian climate revisited: atmosphere and environment of a desert planet*. Springer-Praxis Books, 326 pp.

Ryan, J., R. Henry, S. Hess, C. B. Leovy, J. E. Tillman, and C. Walcek, 1978: Mars meteorology: Three seasons at the surface. *Geophysical Research Letters*, **5,** 715-718.

Ryan, J. A., and R. M. Henry, 1979: Mars atmospheric phenomena during major dust storms, as measured at surface. *Journal of Geophysical Research*, **84,** 2821-2829.

Schiaparelli, G., 1893a: Il pianeta Marte. *Natura ed Arte*, Casa Editrice Dottor Francesco Vallardi.

Schiaparelli, G., 1893b: The Distribution of Land and Water on Mars. *Publications of the Astronomical Society of the Pacific*, **5,** 169-170.

Schiaparelli, G., 1899: Observations of the Planet Mars. *Science*, **9,** 633-637.

Siili, T., R. Haberle, J. Murphy, and H. Savijarvi, 1999: Modelling of the combined late-winter ice cap edge and slope winds in Mars' Hellas and Argyre regions. *Planetary and space science*, **47,** 951-970.

Simpson, J., 1982: Gravity currents in the laboratory, atmosphere, and ocean. *Annual Review of Fluid Mechanics*, **14,** 213-234.

Smith, M., 2004: Interannual variability in TES atmospheric observations of Mars during 1999-2003. *Icarus*, **167,** 148-165.

Smith, M., J. C. Pearl, B. J. Conrath, and P. R. Christensen, 2000: Mars Global Surveyor Thermal Emission Spectrometer (TES) observations of dust opacity during aerobraking and science phasing. *Journal of Geophysical Research*, **105,** 9539-9552.

Smith, M., J. C. Pearl, B. J. Conrath, and P. R. Christensen, 2001: Thermal Emission Spectrometer results- Mars atmospheric thermal structure and aerosol distribution. *Journal of Geophysical Research*, **106,** 23929-23945.

Smith, M., B. J. Conrath, J. C. Pearl, and P. R. Christensen, 2002: Thermal Emission Spectrometer Observations of Martian Planet-Encircling Dust Storm 2001A. *Icarus*.

Snyder, C. W., and V. I. Moroz, 1992: Spacecraft exploration of Mars. *Mars*, H. H. Kieffer, B. M. Jakosky, C. W. Snyder, and M. S. Matthews, Eds., University of Arizona Press, 71-119.

South, J., 1831: On the Extensive Atmosphere of Mars. *Philosophical Transactions of the Royal Society*, **121,** 417-422.

Strausberg, M. J., H. Wang, M. I. Richardson, S. P. Ewald, and A. D. Toigo, 2005: Observations of the initiation and evolution of the 2001 Mars global dust storm. *Journal of Geophysical Research*, **110**.

Timmermans, M., J. Lister, and H. Huppert, 2001: Compressible particle-driven gravity currents. *Journal of Fluid Mechanics*, **445,** 305-325.

Toigo, A. D., M. I. Richardson, R. Wilson, H. Wang, and A. Ingersoll, 2002: A first look at dust lifting and dust storms near the south pole of Mars with a mesoscale model. *Journal of Geophysical Research*, **107**.

Toon, O., J. Pollack, and C. Sagan, 1977: Physical properties of the particles composing the Martian dust storm of 1971-1972. *Icarus*, **30,** 663-696.

Wang, H., M. I. Richardson, R. J. Wilson, A. P. Ingersoll, A. D. Toigo, and R. W. Zurek, 2003: Cyclones, tides, and the origin of a cross-equatorial dust storm on Mars. *Geophys. Res. Lett*, **30,** 1488.

Wanke, H., J. Bruckner, G. Dreibus, and R. Rieder, 2001: Chemical composition of rocks and soils at the Pathfinder site. *Space Science Reviews*, **96,** 317-330.

Wilson, R. J., 2012: Personal Communication.

Wilson, R. J., J. Noble, and S. J. Greybush, 2011: The derivation of atmospheric opacity from surface temperature observations *Fourth International Workshop on the Mars Atmosphere: Modelling and Observations*, Paris, France.

Wilson, R. J., R. M. Haberle, J. Noble, A. F. C. Bridger, J. Schaeffer, J. Barnes, and B. Cantor, 2008: Simulation of the 2001 planet-encircling dust storm with the NASA/NOAA Mars general circulation model. *Third International Workshop on the Mars Atmosphere: Modeling and Observations*, Williamsburg, VA, USA.

Wolff, M. J., and R. T. Clancy, 2003: Constraints on the size of Martian aerosols from Thermal Emission Spectrometer observations. *Journal of Geophysical Research*, **108,** 5097.

Zurek, R. W., 1982: Martian great dust storms: An update. *Icarus*, **50,** 288-310.

Zurek, R. W., and R. Haberle, 1988: Martian Great Dust Storms: Aperiodic Phenomena? *MECA Workshop on Dust on Mars III*., Lunar and Planetary Institute, 62.

Zurek, R. W., and L. J. Martin, 1993: Interannual variability of planet-encircling dust storms on Mars. *Journal of Geophysical Research*, **98,** 3247-3259.

Zurek, R. W., J. R. Barnes, R. M. Haberle, and J. B. Pollack, 1992: Dynamics of the atmosphere of Mars. *Mars*, H. H. Kieffer, B. M. Jakosky, C. W. Snyder, and M. S. Matthews, Eds., University of Arizona Press, 835-933.